

Investigations of DNA-Mediated Redox Signaling Between E.coli DNA Repair Pathways

Thesis by
Andy Zhou

In Partial Fulfillment of the Requirements for the
Degree of
Biochemistry and Molecular Biophysics

The logo for the California Institute of Technology, featuring the word "Caltech" in a bold, orange, sans-serif font.

CALIFORNIA INSTITUTE OF TECHNOLOGY
Pasadena, California

2019
Defended 7/23/2018

© 2019

Andy Zhou

ORCID: 0000-0003-3383-0855

All rights reserved

ACKNOWLEDGEMENTS

Researching with Jackie Barton as my PhD advisor has been a life-changing experience. She strives for her students to "push back the frontiers", and under her leadership our laboratory achieves this feat. I thank her for all of the advice, critique, discussions, and insight over the years and appreciate the tremendous support she provides as a mentor. I would like to thank my thesis committee: Harry Gray, Doug Rees, Dave Tirrell, and Long Cai. You all have kept your doors open when I needed to discuss academic progression or inquire about research roadblocks and I truly appreciate the scientific and professional support you all have provided. I would like to thank all of my labmates past and present. Specifically, I thank Phil Bartels, Rebekah Silva, Edmund Tse, Levi Ekanger, Lionel Marcelis, Mike Grodick, Helen Segal, and Anna Arnold for discussing research and collaboration. Additionally, I thank Adam Boynton, Stephanie Threatt, Siobhán MacArdle, Elizabeth O'Brien, Natalie Muren, Sandra Koenig, Yingxin Deng, Adela Nano, Ariel Furst, Tim Mui, Alyson Weidmann, Alexis Komor, and Ted Zwang, as we are all one big academic family. I would like to thank Shyam Saladi and Scott Saunders for thoughtful discussion in research and data analysis.

I thank Chris Tang and Kevin Kauntz, my friends from Miami University. No matter how old we get, our conversations never get old. Transitioning into graduate school was not nearly as tough thanks to your friendship. I want to thank Gary Lorigan and David Spencer for their mentorship during my undergrad times and for convincing me to go into academic research. I would like to thank the friends that I have made here at Caltech: Dan Piraner, Kelsey Boyle, Andy Buller, Belinda Wenke, Griffin Chure, Ferdinand Huber, Joe Redford, Bill Ireland, Shyam Saladi, Phil Bartels, Lionel Marcelis, and Levi Ekanger. Fun times.

I would like to thank my Family. Chunlan Liu and Hongcai Zhou are wonderful parents and raised me well. Jennifer is an amazing individual and I am glad to be her sibling. I am forever grateful for love you all show and the opportunities you have given me. I love you all. Finally, I want to thank Emily Blythe for always being by my side. You have changed my life ever since graduate school interviews. I will always appreciate what we have.

ABSTRACT

The 4Fe4S cluster has been identified in various DNA-processing proteins spanning a variety of biological functions and all domains of life. Recently, a novel functional role for the cluster has been identified for proteins in DNA repair and replication as a redox switch for DNA binding. Human DNA primase utilizes this redox switch to coordinate primer handoff in replication. The enzymatic activity of DNA polymerase δ is tuned by the redox-switch, allowing for a fast and reversible regulation of replication in response to oxidative stress. In all cases, the redox of the 4Fe4S cluster is achieved through DNA-mediated charge transport (CT), the ability for DNA to carry charge through its π -stack. Due to the reliance of this phenomena on the π -stacking of the nitrogenous bases, DNA CT is sensitive to DNA lesions and mismatches and can proceed over long molecular distances if the DNA is well-stacked. Given this powerful biological phenomena, new inter-protein signaling interactions have been identified with important downstream consequences for genome fidelity. Here, we investigate the ways DNA-mediated charge transport between DNA processing enzymes results in efficient DNA repair or prevention of DNA-damage.

First, we investigated Dps, a bacterial ferritin that protects DNA from oxidative stress and implicated in bacterial survival and virulence. Dps iron sites can scavenge diffusing oxidants directly but additionally electrons and electron holes can be rapidly transported through the base-pair π -stack through DNA CT, thus providing an additional mechanism of genome protection by Dps. Using X-band EPR, we monitored formation of mononuclear high-spin Fe(III) sites of low symmetry as a gauge of effective Dps protection via oxidation of its iron sites. Using poly(dGdC)₂ or poly(dAdT)₂ DNA, we uncovered the dependence of DNA protection by Dps to the formation of guanine radical intermediates. Oxidation of Dps iron sites depended on the presence of the W52 residue. Point mutations of W52 revealed its involvement in an electron transfer (ET) pathway for the oxidation of the Dps iron sites. Finally, we investigated the *in vivo* consequences of the Dps W52 residue by complementing knockout Dps *E.coli* with plasmids expressing WT, W52A, or W52Y Dps and applying oxidative stress to the cells through hydrogen peroxide treatment. These assays further demonstrated the ability of Dps to protect the *E.coli* genome from harmful oxidants DNA-mediated electron transfer processes.

Second, we assessed the redox properties of EndoIII and MutY, two base

excision repair glycosylases containing 4Fe4S clusters, in the presence and absence of DNA. Previous work has shown these proteins to have a midpoint redox potential around 80mV vs. NHE when bound to DNA with a positive shift in potential in the absence of DNA. However, electrochemical details that define this midpoint potential have not been uncovered. Using a pyrolytic graphite edge electrode, we measured the midpoint potential of point mutations of EndoIII where point charges are flipped near the cluster (K208E, Y205H, and E200K) in the absence of DNA. Our measurements suggest that a change in a single point charge is not enough to shift the 4Fe4S cluster midpoint potential dramatically. Addition of a poly-L-glutamate polyanion introduced a slight negative shift (~20mV), but with the introduction of DNA a large negative shift was observed (70mV). Overall, binding to the DNA polyanion is the dominant effect in tuning the redox potential of the 4Fe4S cluster, helping to explain why all DNA binding proteins with 4Fe4S clusters studied to date have similar DNA-bound potentials.

With these similar DNA-bound potentials, inter-protein redox signaling should occur. Previous works have demonstrated DNA-mediated redox signaling such as EndoIII signaling to DinG helicase, involved in R-loop maturation, increasing cellular survival by resolving deleterious R-loops. Additionally, different cluster-containing repair proteins of different functions and domains of life have been shown using atomic force microscopy (AFM) to localize to DNA mismatches through a redox switch for DNA-binding affinity. Given a DNA-mediated redox signaling system to scan the genome for lesions, the expression levels of these proteins may play a role in defining the scanning efficiency. We identified that the EndoIII *E.coli* knockout strain was sensitive to UV irradiation. This implies that EndoIII assists the nucleotide excision repair (NER) pathway via DNA-mediated redox signaling. However, knockout of MutY, another 4Fe4S glycosylase, does not impart the same UV sensitivity, and thus suggests key differences between MutY and EndoIII that define effective DNA-mediated redox signaling. Thus, the effect of protein expression level on the efficiency of DNA-mediated redox signaling was investigated using inducible protein expression of EndoIII to rescue UV-sensitivity. Using both plasmid-based and genome integrated constructs, we uncovered that low amounts of EndoIII expression were enough to rescue the growth defect, and overexpression of WT EndoIII leads to a greater defect caused by excess non-specific enzyme activity. These findings further informed investigation of this unique protein signaling interaction between EndoIII and NER protein UvrC.

With proper EndoIII rescue plasmids, we further characterized the DNA-mediated redox signaling interaction between EndoIII and UvrC. Using UV-irradiation of genetic knockout strains and growth curve analysis, we demonstrate that EndoIII expression is essential for efficient repair of UV-induced DNA lesions, as measured through quantitative changes in growth lag-time when wild-type or mutant EndoIII is present in the cell. Electrochemical analysis of EndoIII point mutants quantify the DNA-CT inefficiencies that lead to the observed phenotypes. EndoIII, a BER repair protein, assists the NER pathway in the repair of UV-induced DNA lesions via DNA-mediated redox signaling. These results give evidence of a new signaling crosstalk between two distinct DNA repair pathways.

PUBLISHED CONTENT AND CONTRIBUTIONS

- (1) Bartels, P. L.; Zhou, A.; Arnold, A. R.; Nuñez, N. N.; Crespilho, F. N.; David, S. S.; Barton, J. K. *Langmuir* **2017**, *33*, 2523–2530.
 - (2) Ha, Y.; Arnold, A. R.; Nuñez, N. N.; Bartels, P. L.; Zhou, A.; David, S. S.; Barton, J. K.; Hedman, B.; Hodgson, K. O.; Solomon, E. I. *J. Am. Chem. Soc.* **2017**, *139*, 11434–11442.
 - (3) Arnold, A. R.; Zhou, A.; Barton, J. K. *J. Am. Chem. Soc.* **2016**, *138*, 11290–11298.
-
1. A. Z. purified Endonuclease III mutants and helped perform PGE electrochemistry for the manuscript.
 2. A. Z. purified Endonuclease III mutants for XAS.
 3. A. Z. performed hydrogen peroxide survival assays, data analysis for those assays, and helped write the manuscript.

TABLE OF CONTENTS

Acknowledgements	iii
Abstract	iv
Published Content and Contributions	vii
Table of Contents	viii
List of Figures	x
List of Tables	xix
Nomenclature	xx
Chapter I: DNA-mediated redox signaling in biology	1
1.1 DNA charge transport	2
1.2 Fe ₄ S ₄ Clusters in DNA-processing enzymes	3
1.3 DNA-mediated redox signaling	4
1.4 <i>In vitro</i> experiments demonstrating DNA-mediated redox signaling	4
1.5 <i>In vivo</i> experiments demonstrating DNA-mediated redox signaling	5
1.6 Conclusion	6
Chapter II: Protection of DNA by Dps bacterial ferritin using Protein-DNA electron transfer	9
2.1 Introduction	10
2.2 Materials and Methods	13
2.3 Results	16
2.4 Discussion	26
2.5 Conclusions	28
Chapter III: Direct electrochemical investigations of charged point mutations on the redox potential of Endonuclease III	33
3.1 Introduction	34
3.2 Materials and Methods	37
3.3 Results	40
3.4 Discussion	50
Chapter IV: Investigation of repair protein expression levels and DNA-mediated signaling in genome-wide lesion detection	55
4.1 Introduction	56
4.2 Materials and Methods	57
4.3 Results	61
4.4 Discussion	71
Chapter V: Repair pathway crosstalk between base excision repair and nu- cleotide excision repair in <i>E. coli</i>	76
5.1 Introduction	77
5.2 Materials and Methods	78
5.3 Results	83
5.4 Discussion	88

Appendix A: Additional Figures and Tables	92
A.1 Supplemental figures for Chapter 2	92
A.2 Supplemental figures for Chapter 3	96
A.3 Supplemental figures for Chapter 4	98
A.4 Supplemental figures for Chapter 5	99
Appendix B: Primers	104

LIST OF FIGURES

<i>Number</i>	<i>Page</i>
1.1 Illustration of experiment demonstrating photo-induced electron transfer through DNA adapted from Grodick et al. The Ru donor and Rh acceptor are shown in yellow and red respectively.	2
2.1 Schematic depicting DNA-mediated oxidation of ferrous iron-loaded Dps to fill the guanine radical hole generated by flash-quench chemistry.	12
2.2 Chemical oxidation of WT E. coli Dps containing 12 Fe(II)/Dps with stoichiometric ferricyanide. Conditions: Dps concentration: 20 μ M; Fe/Dps: 11.9 ± 0.2 ; Buffer: 50 mM Tris, pH 7, 150 mM NaCl, 5% glycerol. Instrument settings: modulation amplitude = 10 G at 100 kHz; frequency = 9.373 GHz; microwave power = 6.4 mW; and temperature = 10 K.	18
2.3 DNA-bound WT E. coli Dps oxidation via the flash-quench technique. All spectra have had an individual unirradiated spectrum subtracted; thus all features are a function of irradiation. Concentrations: 20 μ M Dps (Fe(II)/Dps: 11.9 ± 0.2), 1 mM base-pairs poly(dGdC) ₂ or poly(dAdT) ₂ DNA, 20 μ M [Ru(phen)(dppz)(bpy')] ²⁺ , 120 μ M [Co(NH ₃) ₅ Cl] ²⁺ . Buffer: 50 mM Tris, pH 7.0, 150 mM NaCl, 5% glycerol. Minus DNA sample contains ferrous iron-loaded Dps, Ru, and Co, but lacks DNA; Light control contains ferrous iron-loaded Dps, poly(dGdC) ₂ DNA, and Ru, but lacks Co quencher. Instrument settings: modulation amplitude = 10 G at 100 kHz; frequency = 9.37 GHz; microwave power = 6.4 mW; and temperature = 10 K.	19

- 2.4 Folding and iron loading of W52 Dps mutants. (Upper) Circular dichroism spectra of wild-type (WT) (black), W52A (red), and W52Y (green) *E. coli* Apo-Dps. Dps monomer depicted in gray, showing α -helical structure (PDB: 1DPS). Protein concentration was 5 μ M in a buffer of 50 mM Tris, pH 7.0, 150 mM NaCl. (Lower) Ferrous iron loading of Dps W52 mutants compared to WT *E. coli* protein. Normalized UV-vis spectra of $[\text{Fe}(\text{bpy})_3]^{2+}$ produced from either WT Dps (black), W52A Dps (red), or W52Y Dps (green). For normalization, the absorbance values were divided by protein concentration. The calculated number of iron atoms per Dps dodecamer is 14.6 ± 0.5 for WT Dps, 8.6 ± 0.4 for W52A, and 10.6 ± 0.4 for W52Y. Protein concentrations were determined as given in the Materials and Methods Section. 21
- 2.5 Comparison of chemical oxidation of ferrous iron-loaded Dps with ferricyanide, and oxidation following DNA photooxidation. EPR intensity for the Dps mutants was adjusted to that of the WT protein via dividing by the ratio $\text{Fe}_{\text{W52}}/\text{Fe}_{\text{WT}}$. (A) Oxidation by 2-fold excess ferricyanide: 20 μ M Dps ($\text{Fe}^{2+}/\text{Dps}$: WT: 13.6 ± 0.2 , W52A: 8.8 ± 0.2 ; W52Y: 11.3 ± 0.1), 480 μ M ferricyanide. (B) Comparison of ferrous iron-loaded WT Dps and W52A/Y mutant following DNA photooxidation. All spectra have had an individual unirradiated spectrum subtracted. Concentrations: 20 μ M Dps ($\text{Fe}^{2+}/\text{Dps}$: WT: 16.0 ± 0.5 , W52A: 10.1 ± 0.2 ; W52Y: 11.5 ± 0.2), 1 mM base-pairs poly(dGdC)₂ DNA, 20 μ M $[\text{Ru}(\text{phen})(\text{dppz})(\text{bpy}')^{2+}$, 120 μ M $[\text{Co}(\text{NH}_3)_5\text{Cl}]^{2+}$. 50 mM Tris, pH 7.0, 150 mM NaCl, 5% glycerol. Modulation amplitude = 10 G in (A) and 5 G in (B) at 100 kHz; frequency = 9.37 GHz; microwave power = 6.4 mW; and temperature = 10 K. 22
- 2.6 Hydrogen peroxide survival assay comparing *E. coli* with WT, W52Y, or W52A Dps. Dps has been induced with 0.2% w/v L-arabinose and cells treated with either 3 (solid gray bars) or 5 (dashed bars) mM hydrogen peroxide. Percent survival was calculated as the fraction of surviving colonies over the number of CFUs seeded (seeded CFUs calculated by dilution-adjusted OD600 readings). Each mutant data set was normalized to the WT survival percentage. The standard error of the mean was calculated by treating each droplet as a data point. 24

- 3.1 Representative CVs from EndoIII and MutY thin films on a PGE electrode. A thin film containing only 75 μM EndoIII capped with Nafion gave a quasi-reversible signal with reductive and oxidative peaks centered, respectively, at 74 ± 11 and 162 ± 20 mV versus NHE (center; red trace). Notably, the addition of CNTs substantially amplified the signal, simplifying quantification (center; blue trace). Similarly, 25 μM MutY in the presence of CNTs yielded a signal with reductive and oxidative peaks at 100 ± 9.0 and 162 ± 3.0 mV versus NHE (bottom). CV scans were taken at a scan rate of 100 mV/s. . . . 41
- 3.2 EndoIII and MutY thin film voltammetry on a PGE electrode in the presence of DNA. By SQWV, the presence of DNA resulted in a -65 mV shift in the potential of 75 μM EndoIII (center), with a similar result for 25 μM MutY (bottom). Signals were very small due to surface passivation, but they were still readily apparent by SQWV. Unfortunately, CNTs led to inconsistent and unstable signals, likely interfering with DNA binding, so they could not be used to enhance the signals. Thin films were formed from several layers of a premixed 1:1 protein/DNA solution, and were capped with Nafion. SQWV scans were taken at a frequency of 15 Hz with 0.025 V amplitude, and scans were from positive to negative potentials (indicated by the arrow). 48
- 3.3 Thin film voltammetry of WT EndoIII with poly-L-glutamate and comparison of WT with the mutants E200K, Y205H, and K208E. Unlike DNA, poly-L-glutamate caused no significant potential shift even at 6 mM glutamate (top). 75 μM WT and mutant EndoIII in protein/CNT/Nafion thin films had nearly identical potentials, with CV peaks centered around 125 mV versus NHE (center); the similarity is even more apparent by DPV (bottom). Small shifts within the measurement error (10–15 mV) are still possible but pale in comparison to the effect of DNA. All CVs shown were taken at 100 mV/s, while DPVs were taken at an amplitude of 0.05 V with a 0.5 s pulse period. Poly-L-glutamate was preincubated with 75 μM EndoIII both with and without CNTs; due to the larger signals, the CVs shown are from films including CNTs. 49

4.1	Illustration of the consequence of protein copy number on the scanning model. Given a lesion highlighted in the red circle that is a substrate for only the teal-colored protein, the efficiency of the teal 4Fe4S repair protein should decrease as the purple-colored 4Fe4S proteins are taken out of the system, as there are now fewer proteins overall participating in redox-signaling and scanning the genome.	57
4.2	OpenCFU interface for drawing regions of interest and counting colonies.	60
4.3	Clonetegration genome integration module developed by Endy et al. Adapted with permission from St-Pierre, F. et al. ACS Synth. Biol. 2013, 2, 537. Copyright 2013 American Chemical Society.	61
4.4	Growth of $\text{InvA}\Delta\text{muty}$ compared with InvA measured through optical density over 7 hours.	62
4.5	UV sensitivity colony count assay of Δnth and Δmuty strains after treatment with $30\text{J}/\text{m}^2$ UV. Pictures of colonies for each knockout strain (left) and a histogram (right).	62
4.6	LB-plates containing droplets of Δnth with pPro30-nth or empty rescue plasmid after treatment with $30\text{J}/\text{m}^2$ UV with varying propionate inducer concentrations.	63
4.7	Normalized survival from UV-sensitivity droplet assay using pLac. Strains of Δnth with various rescue plasmids were treated with $30\text{J}/\text{m}^2$ UV and plated as droplets. Colonies were quantified and the fraction survival was calculated and normalized to best surviving conditions. (I) and (U) stand for induced and uninduced, respectively, with induction meaning a final concentration of $50\ \mu\text{M}$ of IPTG. (NS) means "nonsense" and contains a pLac plasmid expressing a nonsense peptide. Data presented are of three biological replicates.	64
4.8	Normalized survival from UV-sensitivity droplet assay using pBAD. Strains of Δnth with various rescue plasmids were treated with $30\text{J}/\text{m}^2$ UV and plated as droplets. Colonies were quantified and the fraction survival was calculated and normalized to best surviving conditions. Arabinose inducer concentration was $50\ \mu\text{M}$ when added. Data presented are of three biological replicates.	65

4.9	Normalized survival from UV-sensitivity droplet assay using pBAD. Strains of Δ nth with various rescue plasmids were treated with $30J/m^2$ UV and plated as droplets. Colonies were quantified and the fraction survival was calculated and normalized to best surviving conditions. Arabinose inducer concentration was $200 \mu M$ when added. Data presented are of three biological replicates.	66
4.10	Growth curves of Δ nth with genome-integrated WT, D138A, and Y82A EndoIII with varying amounts of arabinose inducer added. 95% confidence intervals are calculated using the bootstrap method for 16 technical replicates.	67
4.11	Growth curves of InvA Δ nth with various EndoIII rescue plasmids replicated using strains from Grodick et al. 95% confidence intervals are calculated using the bootstrap method for 16 technical replicates.	68
4.12	Growth curves of InvA Δ nth with pBAD EndoIII rescue plasmids at various arabinose inducer concentrations. 95% confidence intervals are calculated using the bootstrap method for 16 technical replicates.	68
4.13	Growth curves of InvA Δ nth strains with rescue plasmids from Grodick et al after 2 overnight growth cycles with antibiotic selection. Technical replicates are plotted individually.	69
4.14	Design of rescue plasmids used in previous works. A 5' extension 283 base pairs upstream of EndoIII (<i>rsxE</i>) is added into the plasmid.	69
4.15	Growth of the Δ nth strain with and without the WT EndoIII rescue plasmid.	70
5.1	Schematic of DNA-mediated redox signaling. Two 4Fe4S containing DNA-repair proteins (green and olive) conduct redox between their clusters forcing one to bind with high affinity and the other to unbind with low affinity. This process can occur iteratively through DNA until a lesion is present where localization of bound repair proteins to the DNA-lesion follows.	79
5.2	UV-sensitivity droplet assay. Strains of Δ nth expressing either WT-nth or RFP were treated with $30J/m^2$ UV and plated as droplets. Colonies were quantified and the fraction survival was calculated and normalized to WT conditions. Data presented are of three biological replicates.	83

5.3	Average growth curve of Δ nth and Δ araC over 11 hours measured through OD600 readings. Error bars are the 95% confidence interval calculated using the bootstrap method.	84
5.4	Δ lag-times of Δ araC and Δ nth strains with various rescue plasmids after treatment with $90J/m^2$ UV. Δ lag-times were calculated by subtracting the lag-time of each individual well by the lag-time of the minimum of the individual experimental dataset. Error bars are 95% confidence intervals calculated using the bootstrap methods. Data presented is from three biological replicates.	85
5.5	EMSA of K120 and Y82A for measurement of nonspecific DNA-binding affinity. K_d was calculated through non-linear least squares fitting of free dsDNA band intensities to a Hill equation with a Hill coefficient of 1.	86
5.6	Cyclic voltammetry of WT, K120Q, and Y82A EndoIII. Buffer scan capacitance for each point-mutant indicate similar DNA-modified surfaces before the addition of protein. A reversible redox reaction is observed at 80mv vs. NHE.	86
5.7	Quantification of Cluster degradation using UV-Vis. The absorbance intensity at 410nm was measured as a proxy for the concentration of the 4Fe4S cluster over 28 hours. Linear regression was performed using the least squares method for all data points up to 6 hours to model degradation over the timescale of a typical electrochemical experiment.	87
5.8	Circular Dichroism spectroscopy on WT, K120Q, and Y82A EndoIII. CD signals were normalized to the minimum signal of each dataset by division. A ratio of 222:208nm was calculated for each point mutant to report the presence coiled-coils.	87
A.1	Wide EPR spectra of irradiated sample containing WT ferrous iron-loaded Dps, poly(dGdC) ₂ DNA, Ru(phen)(dppz)(bpy') ²⁺ , and [Co(NH ₃) ₅ Cl] ²⁺ with dark control subtracted. All conditions and instrument settings are identical to Figure 2.3 in Chapter 2.	92
A.2	Ferrous iron only (no protein) mixed with stoichiometric ferricyanide in 50 mM Tris, pH 7.0, 150 mM NaCl, 5% glycerol. Concentration of iron was 240 μ M, equivalent to that in 20 μ M solution of Dps with 12 Fe/Dps. Instrument settings identical are to Figure 2.3 in Chapter 2.	92

- A.3 WT Dps EPR spectra compared to Fe only control in MOPS buffer. Concentrations: Fe only: 240 μM ferrous iron with 240 μM ferricyanide (black trace). Irradiated Dps sample: 20 μM Dps ($\text{Fe}^{2+}/\text{Dps}$: 11.7 ± 0.1), 1 mM base-pairs poly(dGdC)₂ DNA, 20 μM [Ru(phen)(dppz)(bpy')]²⁺, 120 μM [Co(NH₃)₅Cl]²⁺ (red trace). Buffer: 50 mM MOPS, pH 7.0, 150 mM NaCl, 5% glycerol. Dps spectrum has had DC subtracted. Instrument settings: modulation amplitude = 10 G at 100 kHz; frequency = 9.37 GHz; microwave power = 6.4 mW; temperature = 10 K. 93
- A.4 Dark controls (before irradiation) of DNA-bound ferrous iron-loaded WT Dps and W52A/Y mutants. Spectra not adjusted for Fe loading of mutants. Concentrations: 20 μM Dps ($\text{Fe}^{2+}/\text{Dps}$: WT: 16.0 ± 0.5 , W52A: 10.1 ± 0.2 ; W52Y: 11.5 ± 0.2), 1 mM base-pairs poly(dGdC)₂ DNA, 20 μM [Ru(phen)(dppz)(bpy')]²⁺, 120 μM [Co(NH₃)₅Cl]²⁺. Buffer: 50 mM Tris, pH 7.0, 150 mM NaCl, 5% glycerol. Instrument settings: modulation amplitude = 5 G at 100 kHz; frequency = 9.37 GHz; microwave power = 6.4 mW; temperature = 10 K. 94
- A.5 Growth of *E. coli* ZK2471 strain (dps::kan ΔrecA Δara) containing WT, W52A, or W52Y pBAD18-dps plasmids induced with 0.2 w/v L-arabinose. 94
- A.6 Raw images of *E. coli* ZK2471 strain (dps::kan ΔrecA Δara) containing WT, W52A, or W52Y pBAD18-dps plasmids induced with 0.2 w/v L-arabinose, treated with 3mM and 5mM hydrogen peroxide, and diluted 10,000-fold. 95
- A.7 *E. coli* ZK2471 strain (dps::kan ΔrecA Δara) containing WT, W52A, or W52Y pBAD18-dps plasmids induced (+) with 0.2 w/v L-arabinose or uninduced (-). Each 10 μL droplet contains a unique dilution factor and concentration of hydrogen peroxide. This layout was conducted to extract optimal experimental conditions to ensure a quantifiable amount of colonies on plates. At 3.5 mM treatment of peroxide treatment (5th row colonies) there are clear differences in survival between induced and uninduced strains. We extrapolated that 3 mM H₂O₂ treatment of 10,000-fold diluted cells would create countable colonies for the survival assay. 95

- A.8 CV scans of storage buffer, a CNT/Nafion thin film, and a WT EndoIII/CNT/Nafion thin film. CNTs increase the capacitance dramatically relative to buffer alone (20 mM sodium phosphate, pH 7.5, 150 mM NaCl, 0.5 mM EDTA; green plot), although they also enhanced the signal due to charged surface species (around 200 mV vs NHE) in addition to a signal near -80 mV vs NHE attributable to oxides on the CNTs themselves (brown plot). Notably, neither of these peaks exhibited any splitting, indicative of rapid processes taking place at the surface. Incorporation of 75 μ M EndoIII into the thin film suppressed both of these signals, and resulted in the appearance of a reversible signal with noticeable peak splitting near 100 mV vs NHE. The much higher capacitance in these CVs relative to those in Figure 1 is due to the addition of 3-6 more layers of CNT/protein than later CVs, which made the comparison easier but also caused the EndoIII peaks to be less clearly defined. All CVs were taken at a scan rate of 100 mV/s. 96
- A.9 Scan rate dependence of the current for EndoIII and MutY, and peak splitting for WT EndoIII. The linear dependence of current on scan rate confirms that the protein is adsorbed to the electrode surface (EndoIII, top right; MutY, top left). Because the proteins were adsorbed to the surface, Laviron's method for non-diffusive systems was applied to estimate electron transfer rates (k_{ET}) and coefficients (α) for EndoIII (bottom; the small size of the MutY signal precluded Laviron analysis). 97
- A.10 Electrochemistry controls on the PGE electrode. To determine the electro-active area of the PGE electrode and to verify the accuracy of measured potentials, 2 mM $[\text{Ru}(\text{NH}_3)_6]^{3+}$ in EndoIII storage buffer was added in the presence (dark green) and absence of CNTs (light green). Notably, while the peak splitting decreased slightly in the presence of CNTs, the midpoint potential was unaltered. 97
- A.11 Growth curves of E.coli after arabinose induction for expression of the Lux operon adapted from Ceroni et al. 98

- A.12 The starting OD600 of Δ araC and Δ nth strains with various rescue plasmids either treated with $90J/m^2$ UV or left untreated. This initial-OD was extracted from the y-intercept of the curve fits for each well. Error bars are 95% confidence intervals calculated using the bootstrap methods. Data presented is from three biological replicates. 99
- A.13 The Δ lag-times of Δ araC and Δ nth strains with various rescue plasmids either treated with $90J/m^2$ UV or left untreated. Error bars are 95% confidence intervals calculated using the bootstrap methods. Data presented is from three biological replicates. 99
- A.14 The maximum specific growth of Δ araC and Δ nth strains with various rescue plasmids either treated with $90J/m^2$ UV or left untreated. Error bars are 95% confidence intervals calculated using the bootstrap methods. Data presented is from three biological replicates. 100
- A.15 96-well plate OD600 growth curves of each genotype of E.coli after treatment of $90J/m^2$ UV. Curves from the 16 technical replicates of each genotype are represented as an average with a 95% confidence interval acquired through the bootstrap method. 100
- A.16 (A) Δ lag-time data of E.coli treated with $90J/m^2$ UV visualized as a beeswarm plot. Every observation over three biological replicates are plotted. (B) Boxplot of Δ lag-time data showing the minimum and maximum extent of the data, outliers, median, and data quartiles (1st and 3rd). 101
- A.17 Scan-rate dependence of WT, K120Q, and Y82A EndoIII. The relationship of peak current to scan-rate of EndoIII was analyzed using a linear least squares method to produce regression lines for a linear or square-root of scan-rate dependence. The correct dependence is selected as the regression line with the highest coefficient of determination (R^2). 102
- A.18 UV-vis spectra of EndoIII point mutants at $t = 0$ hours. Starting concentrations are calculated by the absorbance of the 4Fe4S cluster at 410nm using an extinction coefficient $\epsilon_{410nm} = 17000M^{-1}cm^{-1}$. Cluster degradation analysis was completed by normalizing to these concentrations. 103

LIST OF TABLES

<i>Number</i>	<i>Page</i>
1.1 Table of Fe ₄ S ₄ DNA processing enzymes.	3
3.1 Potentials (versus NHE) of SQWV Reductive Sweeps for WT and Mutant EndoIII and WT MutY in the Presence and Absence of DNA ^a . (a) When used, CNTs were added from a 0.25 mg/mL stock, and all experiments used protein storage buffer as the supporting electrolyte (20 mM sodium phosphate, 0.5 mM EDTA, 150 mM NaCl, pH 7.5 for EndoIII and 20 mM sodium phosphate, 1 mM EDTA, 150 mM NaCl, pH 7.6 for MutY). Each value is the average of three or more separate experiments, and the error is the standard deviation of the mean. (b) No CNTs present. (c) The MutY SQWV peaks (Figure 3.2) were too small and noisy to measure the potential with confidence. (d) OG:FA MutY substrate trap DNA.	44
A.1 Protein expression levels of EndoIII and MutY measured by ribosome profiling and single molecule counting [1, 2]	98
B.1 Table of primers for Clonetegration [4].	104
B.2 Table of primers for colony PCR of InvA strain.	105
B.3 Table of primers for pPro, pLac, and pBAD tunable EndoIII plasmids.	106
B.4 Table of primers for site directed mutagenesis of EndoIII and RFP control plasmid.	107

NOMENCLATURE

- AFM.** Atomic force microscopy.
- BER.** Base excision repair: a DNA repair pathway specialized in the repair of single damage DNA bases.
- CC104.** Strain of *E.coli* with a deactivated β -galactosidase caused by a A→C substitution.
- CD.** Circular dichroism.
- D138.** Aspartate 138 of EndoIII: Involved in EndoIII glycosylase activity.
- DNA.** Deoxyribonucleic acid.
- DNA CT.** DNA charge transport: the phenomenon in which DNA conducts charge through its stacked nucleobases.
- EMSA.** Electrophoretic mobility shift assay.
- EndoIII.** Endonuclease III: a base excision repair glycosylase.
- EPR.** Electron paramagnetic resonance.
- InvA.** Strain of *E.coli* with an inverted *rrnA* operon.
- K120Q.** Lysine 120 of EndoIII: Involved in EndoIII glycosylase activity.
- NER.** Nucleotide excision repair pathway: a DNA repair pathway specialized in repairing bulky DNA lesions such as those formed by UV irradiation.
- NHE.** Normal hydrogen electrode.
- nth.** Name of gene encoding EndoIII.
- OD₆₀₀.** Optical density at 600nm measured through absorbance at that wavelength.
- PGE.** Pyrolytic graphite edge.
- R-loop.** Three stranded nucleic acid structure; RNA invades the DNA duplex creating a RNA:DNA hybrid along with the excluded DNA strand.
- RBS.** Ribosome binding site.
- rrnA.** An operon in *E.coli* encoding ribosomal and transfer RNAs.
- W52.** Tryptophan 52 of Dps: Involved in Dps electron transfer pathway.
- Y82.** Tyrosine 82 of EndoIII: Involved in EndoIII DNA CT.

*Chapter 1***DNA-MEDIATED REDOX SIGNALING IN BIOLOGY**

1.1 DNA charge transport

The phenomenon of DNA to conduct charge through its stacked nucleobases, or DNA charge transport (DNA-CT), provides biology with the ability to carry out long-range redox chemistry. This phenomena was experimentally demonstrated using metallointercalators containing Ru or Rh in a donor-acceptor pair [1]. DNA CT of an electron from the photo-excited metallointercalator to its distal partner results in luminescence quenching and is illustrated in Figure 1.1. The metallointercalators $\text{Ru}(\text{phen})_2\text{dppz}^{2+}$ and $\text{Rh}(\text{phen})_2\text{phen}^{3+}$ attached covalently to either ends of a 15-mer DNA duplex as donor and acceptor pair. DNA CT was observed through rapid quenching of the donor luminescence by the acceptor after photo-excitation. Multiple in vitro setups have been used to measure DNA CT subsequently resulting in characterization of its picosecond timescales [2] and sensitivity to mismatched and otherwise perturbed base stacking [3, 4]. The sensitivity of DNA CT to perturbations in base stacking resulted in development of diagnostic platforms such as a setup to detect hyperactivity of DNMT1 methyltransferase in colorectal tumors using a DNA-mediated signal from a intercalative methylene blue probe [5]. Naturally, the question arose of whether or not redox active proteins can also utilize the sensitivity of DNA CT to base stacking. Appropriately, multiple DNA-processing enzymes spanning multiple biochemical functions and all domains of life have recently been identified to contain a 4Fe4S cluster. More and more, these proteins have been shown to be redox active on DNA with their oxidation states defining their biochemical activity, affinities, and inter-protein signaling capabilities [6–11].

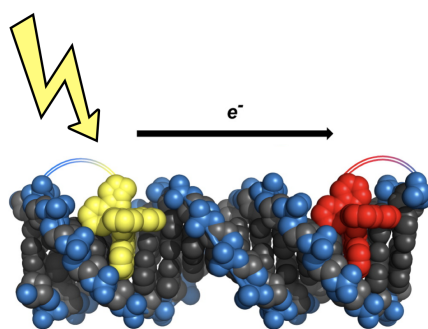


Figure 1.1: Illustration of experiment demonstrating photo-induced electron transfer through DNA adapted from Grodick et al [12]. The Ru donor and Rh acceptor are shown in yellow and red respectively.

Pathway	Bacteria	Archaea	Eukarya
Base excision Repair	EndoIII, MutY	UDG, Mig	NTG2, MUTYH, DME
Nucleotide excision repair	UvrC	XPB	Rad3, XPD
DNA replication	-	-	DNA primase, DNA polymerase (α , δ , ϵ , η)
Replication-coupled repair	AddAB, DinG	-	DNA2, FANCI, ExoV
Telomere maintenance, meiotic crossover	-	-	Rtel1, Chl1
Transcription	-	RNA polymerase	Elp3

Table 1.1: Table of Fe₄S₄ DNA processing enzymes.

1.2 Fe₄S₄ Clusters in DNA-processing enzymes

The Fe₄S₄ cluster is a metal cofactor comprised of four iron and four sulfide ions arranged in a cubane structure. These clusters are used in one electron redox processes and can be very reactive [13]. For example, the Radical S-adenosylmethionine (Radical SAM) enzymes utilize their Fe₄S₄ cluster to generate a 5'-deoxyadenosyl radical intermediate which could then carry out difficult chemical reactions such as C-H bond activation [14]. However, DNA processing enzymes spanning multiple biochemical functions and all domains of life have been shown to contain 4Fe4S clusters (Table 1.1). In the context of DNA CT, the bacterial DNA-repair proteins containing 4Fe4S clusters have been shown to be redox active with a midpoint potential for their [Fe₄S₄]^{2+/3+} couple of around 80mV vs NHE [6, 7, 9]. The sharing of this midpoint potential could be an evolutionary consequence and could allow for redox to occur between proteins through DNA, a phenomena called DNA-mediated redox signaling. From Table 1.1, it is apparent that instead of 4Fe4S clusters being a structural relic from ancestral organisms, more clusters are being identified in higher organisms. Potentially, the redox capabilities of this metal cofactor could impart

biology with diverse biochemical mechanisms for genome maintenance, gene expression, and coordination of large biomolecular machines. Here, DNA-mediated redox signaling, a long-range DNA CT signaling mechanism, as well as key experiments utilizing a diverse set of *in vitro* and *in vivo* techniques that demonstrate this phenomenon.

1.3 DNA-mediated redox signaling

DNA-mediated redox signaling at its core is a redox reaction between two 4Fe4S cluster proteins using DNA CT with the signal being the electron traveling through the well-matched base stack. This signaling allows for switching of oxidation states of the DNA-repair proteins involved in the system. The oxidation state affects the non-specific DNA binding affinity of these proteins, ultimately coordinating "on" and "off" binding events to occur and thus allow for these proteins to scan the DNA for lesions that disrupt the base stack. Thus, DNA-mediated redox signaling between 4Fe4S DNA-repair proteins allows for scanning of the genome for DNA damage and the localization of these proteins to those damaged sites.

1.4 *In vitro* experiments demonstrating DNA-mediated redox signaling

In vitro experiments are essential to the characterization and demonstration of DNA-mediated redox signaling. The Barton laboratory has utilized DNA-modified electrochemistry, pyrolytic graphite-edge electrochemistry and traditional biochemical techniques to characterize proteins that utilize DNA-mediated redox signaling for cellular function and measure their individual redox activity. Atomic force microscopy was used to demonstrate the ability of these proteins to redistribute to DNA strands containing mismatches using this redox signaling mechanism.

In order to perform DNA-mediated redox signaling, DNA repair proteins must be redox active when bound to DNA. Endonuclease III (EndoIII), a base excision repair (BER) glycosylase, displayed reversible redox of its 4Fe4S cluster with a midpoint potential measured at 80mV vs. NHE on DNA-modified electrodes [6, 15]. Subsequently, DinG helicase, XPD helicase and MutY glycosylase also displayed this same redox activity [6, 7, 9]. We now have the components for inter-protein signaling using DNA-mediated redox but biochemical characterization of EndoIII would prove to be a final essential piece to proper demonstration of this DNA-mediated signaling mechanism. Point mutants of EndoIII revealed the key residues involved in its redox and enzymatic activities. EndoIII Y82A was demonstrated to have 90% WT enzyme activity but shown to be less redox active

on DNA-modified electrodes compared to WT [16]. On the other hand, D138A and K120Q have been shown to be catalytically deactivated but still able to conduct DNA-mediated redox signaling [16] (Chapter 5). With these point-mutants, the Barton lab demonstrated inter-protein DNA-mediated redox signaling through AFM. The AFM redistribution assay involves incubation of proteins of interest with either well-matched or mismatched DNA strands. Using AFM, proteins bound to well-matched or mismatched DNA strands can be quantified and thus protein redistribution to mismatched strands is detectable and would suggest DNA-mediated redox signaling. Indeed, EndoIII, XPD, and DinG have all been demonstrated to interchangeably redistribute to mismatched strands of DNA using AFM [8, 9, 16, 17]. More recently, the effect of oxidation state of the 4Fe4S cluster of EndoIII was characterized using microscale thermophoresis (MST) [17]. The 3+ oxidation state of the 4Fe4S cluster of EndoIII was shown to have a 500-fold tighter binding affinity to non-specific DNA compared to the 2+ oxidation state as measured by MST.

1.5 *In vivo* experiments demonstrating DNA-mediated redox signaling

Although the discussed *in vitro* experiments defined the biochemical mechanisms of DNA-mediated redox signaling, *in vivo* experiments are essential for validating the existence of this phenomena in cells. These *in vivo* assays share a common formula: demand a particular DNA-repair pathway to perform its repair function, quantify successful repair events through a measurement of growth or fitness, disrupt the performance of repair by knocking out putative DNA-mediated redox signaling partners, and rescue the performance of repair using point mutants of the signaling partner that modify its DNA CT capabilities.

Lac reversion assay

The first *in vivo* assay used to demonstrate DNA-mediated redox signaling utilized a previously constructed strain, CC104, which reported on MutY activity [18]. In CC104, substitution of an adenine for cytosine inside the lacZ gene creates an inactivation of β -galactosidase activity. Only a GC to TA transversion event at the specific site will restore β -galactosidase activity. However, MutY activity should prevent this transversion from occurring. *E.coli* CC104 growth on minimal lactose medium will only occur with β -galactosidase activity. Therefore, growth of CC104 occurs only with a decreased efficiency of MutY activity. After knocking out EndoIII, CC104 reversion increased two-fold, suggesting that EndoIII contributes to efficient MutY activity [16]. Additionally, this reversion is not decreased with

complementation of DNA CT deficient Y82A EndoIII, demonstrating the DNA CT capabilities of EndoIII leads to more MutY activity [16].

InvA growth assay

Another assay that demonstrated the importance of DNA-mediated redox signaling *in vivo* was the InvA growth assay. This assay measures the growth of a previously constructed strain called InvA [19] which reports on DinG helicase activity. DinG is a 4Fe4S cluster containing helicase involved in R-loop maturation. The InvA strain contains a genetic inversion of the *rrnA* operon, a highly transcribed operon encoding ribosomal RNAs. This inversion forces transcription of the operon to occur in the opposite direction of replication and thus creates a deleterious R-loop which DinG must unwind in order for the strain to survive [19]. Knocking out DinG or proteins which affect the repair efficiency of DinG results in a large growth defect [9, 19]. After knockout of EndoIII in InvA, a growth defect was indeed observed [9]. This growth defect again could not be rescued through plasmid complementation of Y82A EndoIII but could be rescued using D138A EndoIII, a catalytically deactivated point mutant that can still carry out DNA CT. The InvA growth assay established that the repair activity of DinG relied only on EndoIII DNA CT ability but not enzyme activity and was a monumental demonstration of DNA-mediated redox signaling inside cells.

1.6 Conclusion

DNA-mediated redox signaling has been characterized by multiple *in vitro* and *in vivo* experiments. It is a phenomenon that is dictated by non-specific DNA-binding affinity, redox activity, and is interchangeable between redox-active proteins. Additional details about this biological phenomenon were investigated in this thesis. Here, we will establish the biochemical features that define the 80mV midpoint potential of the $[\text{Fe}_4\text{S}_4]^{2+/3+}$ couple using graphite electrochemistry. We will explore the effect of protein expression level on DNA-mediated redox signaling using tunable expression systems. Finally, we will uncover a new DNA-mediated redox signaling interaction between EndoIII and UvrC, a nucleotide excision repair protein using *in vivo* experimental approaches.

References

- (1) Murphy, C. J.; Arkin, M. R.; Jenkins, Y.; Ghatlia, N. D.; Bossmann, S. H.; Turro, N. J.; Barton, J. K. *Science* **1993**, *262*, 1025–1029.
- (2) O'Neill, M. A.; Becker, H.-C.; Wan, C.; Barton, J. K.; Zewail, A. H. *Angew. Chem. Int. Ed. Engl.* **2003**, *42*, 5896–5900.
- (3) Slinker, J. D.; Muren, N. B.; Renfrew, S. E.; Barton, J. K. *Nat Chem* **2011**, *3*, 230–235.
- (4) Boal, A. K.; Barton, J. K. *Bioconjugate Chem.* **2005**, *16*, 312–321.
- (5) Furst, A. L.; Barton, J. K. *Chem Biol* **2015**, *22*, 938–945.
- (6) Boal, A. K.; Yavin, E.; Lukianova, O. A.; O'Shea, V. L.; David, S. S.; Barton, J. K. *Biochemistry* **2005**, *44*, 8397–8407.
- (7) Mui, T. P.; Fuss, J. O.; Ishida, J. P.; Tainer, J. A.; Barton, J. K. *J. Am. Chem. Soc.* **2011**, *133*, 16378–16381.
- (8) Sontz, P. A.; Mui, T. P.; Fuss, J. O.; Tainer, J. A.; Barton, J. K. *Proc. Natl. Acad. Sci. U.S.A.* **2012**, *109*, 1856–1861.
- (9) Grodick, M. A.; Segal, H. M.; Zwang, T. J.; Barton, J. K. *J. Am. Chem. Soc.* **2014**, *136*, 6470–6478.
- (10) Bartels, P. L.; O'Brien, E.; Barton, J. K. In *Iron-Sulfur Clusters in Chemistry and Biology*, 2ed; De Gruyter: 2017; Vol. 2, pp 405–424.
- (11) O'Brien, E.; Holt, M. E.; Thompson, M. K.; Salay, L. E.; Ehlinger, A. C.; Chazin, W. J.; Barton, J. K. *Science* **2017**, *355*, DOI: 10.1126/science.aag1789.
- (12) Grodick, M. A.; Muren, N. B.; Barton, J. K. *Biochemistry* **2015**, *54*, 962–973.
- (13) Rouault, T. A.; Tong, W.-H. *Nature Reviews Molecular Cell Biology* **2005**, *6*, 345–351.
- (14) Broderick, J. B.; Duffus, B. R.; Duschene, K. S.; Shepard, E. M. *Chem. Rev.* **2014**, *114*, 4229–4317.
- (15) Cunningham, R. P.; Asahara, H.; Bank, J. F.; Scholes, C. P.; Salerno, J. C.; Surerus, K.; Munck, E.; McCracken, J.; Peisach, J.; Emptage, M. H. *Biochemistry* **1989**, *28*, 4450–4455.
- (16) Boal, A. K.; Genereux, J. C.; Sontz, P. A.; Gralnick, J. A.; Newman, D. K.; Barton, J. K. *Proc. Natl. Acad. Sci. U.S.A.* **2009**, *106*, 15237–15242.
- (17) Tse, E. C. M.; Zwang, T. J.; Barton, J. K. *J. Am. Chem. Soc.* **2017**, *139*, 12784–12792.
- (18) Cupples, C. G.; Miller, J. H. *PNAS* **1989**, *86*, 5345–5349.

- (19) Boubakri, H.; de Septenville, A. L.; Viguera, E.; Michel, B. *EMBO J* **2010**, *29*, 145–157.

*Chapter 2***PROTECTION OF DNA BY DPS BACTERIAL FERRITIN USING
PROTEIN-DNA ELECTRON TRANSFER**

Adapted with permission from:

- (1) Arnold, A. R.; Zhou, A.; Barton, J. K. *J. Am. Chem. Soc.* **2016**, *138*, 11290–11298.
Copyright 2018 American Chemical Society.

A. Zhou designed and performed the H₂O₂ sensitivity assay. A. Arnold cloned the Dps constructs, purified Dps proteins, and performed EPR and CD spectroscopy on Dps.

2.1 Introduction

Dps proteins are dodecameric (12-mer) bacterial ferritins that protect DNA from oxidative stress, and have been implicated in bacterial survival and virulence [1]. This protection is thought to derive from the ferroxidase activity of Dps, where Dps proteins simultaneously deplete ferrous iron and hydrogen peroxide, reactive species that can otherwise form damaging hydroxyl radicals via Fenton chemistry [2]. Like other ferritins, Dps proteins are spherical, with a hollow core where oxidized iron is reversibly stored. Some Dps proteins nonspecifically bind DNA, such as that from *Escherichia coli* which utilizes N-terminal lysine residues for DNA binding [3]. Within cells, Dps is upregulated by the transcriptional regulator OxyR in response to oxidative stress [4]; Dps is also upregulated in stationary phase, when an additional physical component of Dps protection may be biocrystallization with DNA [5].

DNA charge transport (CT), where electrons and electron holes are efficiently transported through the base-pair π -stack, represents a powerful means to carry out redox chemistry from a distance [6]. Moreover, DNA CT chemistry is remarkably sensitive to the integrity of the intervening DNA. We have explored biological applications of DNA CT, where we have seen this chemistry being utilized as a first step for DNA repair proteins containing 4Fe4S clusters to signal one another and thus localize to the vicinity of a lesion within the vast milieu of the genome [7]. We have also found examples where DNA CT facilitates the selective activation of redox-active transcription factors to respond to oxidative stress from a distance [6]. Given these applications of DNA CT, we considered whether Dps, in addition to interacting directly with diffusing oxidants, might also utilize DNA CT to protect DNA from a distance. Guanine is the most easily oxidized base within DNA, and the presence of adjacent stacked guanines further lowers the 5'-guanine oxidation potential [8]; thus, radicals are characteristically formed at guanine multiplets upon DNA photooxidation [9]. A long distance protection mechanism via DNA CT would involve electron transfer from Dps through the DNA π -stack to fill the hole on guanine radicals, restoring the integrity of the DNA. In this way, Dps could respond to an oxidative affront to the DNA, even if the protein is bound, at the minimum, a hundred base-pairs away [10].

Indeed, we have previously shown biochemically that *E. coli* Dps loaded with ferrous iron at the ferroxidase sites can protect DNA from oxidative damage through DNA CT [11]. $[\text{Ru}(\text{phen})(\text{dppz})(\text{bpy}')]^{2+}$, where phen is 1,10-phenanthroline,

dppz is dipyrido[2,3-a:2',3'-c]phenazine, and bpy' is 4-butyric acid-4'-methyl-2,2'-bipyridine, was covalently tethered to the 5' end of mixed-sequence 70-mer DNA and served as the distally tethered, intercalated photooxidant generated *in situ* by the flash-quench technique. Upon excitation with visible light (“flash”), the ruthenium(II) excited state can be oxidatively quenched (“quench”) by a diffusing quencher, here $[\text{Co}(\text{NH}_3)_5\text{Cl}]^{2+}$, to form a highly oxidizing intercalated Ru(III) complex (1.6 V versus NHE) [12]. In the absence of protein, oxidative damage is observed preferentially at a guanine triplet within the 70-mer DNA duplex. Titrating in ferrous iron-loaded Dps significantly attenuates the level of oxidative damage at the guanine triplet, while Apo-Dps and ferric iron-loaded Dps, which lack available reducing equivalents, do not display this protection [11]. Luminescence experiments rule out direct interaction between the ruthenium photooxidant excited state and Dps, consistent with a long-range DNA-mediated oxidation mechanism. Long-distance, DNA-mediated oxidation of Dps could be an effective mechanism for bacteria to protect their genomes from oxidative insults, contributing to pathogenic survival and virulence.

Here we spectroscopically characterize the DNA-mediated oxidation of ferrous iron-loaded Dps. Electron paramagnetic resonance (EPR) spectroscopy has previously been used to observe oxidation of the 4Fe4S cluster of the base excision repair glycosylase MutY following flash-quench DNA photooxidation [12]. In this work, we use X-band EPR spectroscopy to observe the oxidation of DNA-bound *E. coli* Dps loaded with ferrous iron at the ferroxidase sites and to investigate the DNA-mediated characteristics of this oxidation (Figure 2.1).

We also explore possible protein electron transfer intermediates in the DNA-mediated oxidation of ferrous iron-loaded Dps. There is a highly conserved tryptophan residue in close proximity (approximately 5 Å) to the di-iron ferroxidase site in Dps proteins, W52 in *E. coli* [13]. Aromatic amino acids such as tryptophan and tyrosine can act as electron transfer (ET) hopping intermediates in proteins, allowing for rapid ET across the protein where a single ET process would be kinetically difficult [14]. Because of the location of this aromatic tryptophan residue between the ferroxidase site and the outer protein shell where the DNA must be located, it is an attractive candidate as a hopping intermediate to facilitate ET between the ferroxidase site of Dps and DNA. Previous work has suggested an important role for this conserved tryptophan residue in Dps proteins. Upon oxidation with hydrogen peroxide of Dps loaded with only 6 Fe(II)/Dps, UV–visible stopped flow

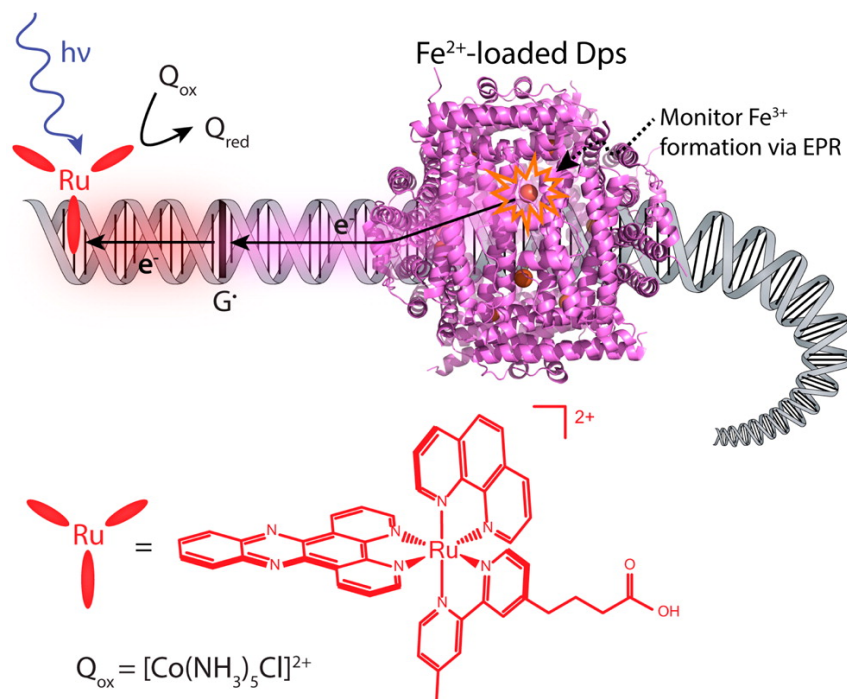


Figure 2.1: Schematic depicting DNA-mediated oxidation of ferrous iron-loaded Dps to fill the guanine radical hole generated by flash-quench chemistry. Visible light first excites an intercalated noncovalently bound ruthenium(II) photooxidant ($[\text{Ru}(\text{phen})(\text{dppz})(\text{bpy}')]^{2+}$), which is then oxidatively quenched by a diffusing quencher (Q, $[\text{Co}(\text{NH}_3)_5\text{Cl}]^{2+}$). This highly oxidizing Ru(III) species abstracts an electron from DNA, preferentially forming guanine radicals. The goal of this study is to observe DNA-mediated electron transfer from the ferrous iron bound at the ferroxidase sites in Dps to the guanine radical by monitoring the appearance of oxidized iron products via EPR. *E. coli* Dps PDB: 1dps.

experiments with *E. coli* Dps were able to observe spectra with maxima at 512 and 536 nm, consistent with a neutral tryptophan radical [15]. By comparison with site-directed mutagenesis studies on *L. innocua* Dps, which also contains a tyrosine residue nearby the ferroxidase site, the tryptophan radical in *E. coli* was ascribed to W52 [15]. A double mutant of *L. innocua* Dps, where both of the aromatic residues in proximity to the ferroxidase site were mutated, was assayed for its ability to protect plasmid DNA from degradation by ferrous iron and hydrogen peroxide. Given that the protective capacity of the *L. innocua* Dps double mutant was significantly attenuated, it was concluded that these conserved aromatic residues act as a trap for electron holes generated by the oxidation of insufficient ferrous iron by hydrogen peroxide [15]. Interestingly, 24-mer ferritins contain a conserved tyrosine residue in close proximity to the ferroxidase site that has also been proposed to act

as a molecular capacitor, although other studies contend with this hypothesis [16]. Overall, the conserved aromatic residue in close proximity to the ferroxidase site may play an important role in ferritins.

Thus, here we investigate two *E. coli* Dps W52 mutants: W52Y, where an aromatic residue is maintained at this position, and W52A, which abolishes the aromatic residue adjacent to the ferroxidase site. We compare these mutants with the wild-type (WT) protein in EPR studies of the oxidation of ferrous iron-loaded Dps following DNA photooxidation. Because the intercalating ruthenium photooxidant is a one-electron oxidant, sending one electron hole at a time into the DNA π -stack, we examine the possible role of *E. coli* Dps W52 as an electron transfer hopping intermediate rather than a molecular capacitor. In addition to EPR, we also probe the role of W52 with respect to cellular survival in studies of *E. coli* under oxidative stress.

2.2 Materials and Methods

Materials

The alternating copolymer DNA duplexes poly(dGdC)₂ and poly(dAdT)₂ were purchased from Sigma. The DNA duplexes were passed through Biorad spin columns (6 K MWCO) before use and quantified based on their molar absorptivity values in base-pairs [17], (poly(dGdC)₂: $\epsilon_{254} = 16800 M^{-1}cm^{-1}$, poly(dAdT)₂: $\epsilon_{262} = 13200 M^{-1}cm^{-1}$). Duplexes were then dried on a speed-vac, brought into an anaerobic chamber, and resuspended in deoxygenated buffer for EPR experiments. Buffers (50 mM Tris or 50 mM MOPS, pH 7.0, 150 mM NaCl, 5% glycerol) were deoxygenated in a Schlenk flask by at least 4 cycles of freeze–pump–thaw.

[Ru(phen)(dppz)(bpy')]²⁺ was synthesized according to published methods [18], purified by reversed-phase chromatography, and characterized by NMR and ESI mass spectrometry (expected for the +2 ion: 409.62 m/z, observed: 410.2 m/z). The ruthenium photooxidant was brought into the anaerobic chamber as a solid powder, resuspended with deoxygenated buffer, and a sample removed for quantification based on UV–vis absorption ($\epsilon_{440} = 21000 M^{-1}cm^{-1}$). [Co(NH₃)₅Cl]Cl₂ was purchased from Sigma (99.995% pure) and used as received. The Co quencher was brought into the anaerobic chamber as a solid powder, resuspended with deoxygenated buffer, and a sample removed for quantification based on UV–vis ($\epsilon_{550} = 47.5 M^{-1}cm^{-1}$).

W52 Mutagenesis

The W52A and W52Y *E. coli* Dps mutants were made with a Quikchange II-E Site-Directed Mutagenesis Kit (Stratagene) using a pBAD18-dps plasmid (containing the WT *E. coli* dps gene and an ampicillin resistance cassette) donated by Dr. Roberto Kolter as a template [19]. Primers were purchased from Integrated DNA Technologies. All mutagenized plasmids were sequenced (Laragen) to confirm the desired sequences. After creating the mutant pBAD18-dps plasmids, the *E. coli* cell line ZK2471 (dps::kan Δ recA Δ ara) donated by Dr. Roberto Kolter was made electrocompetent and the plasmid was transformed via electroporation into these cells.

Dps Overexpression, Purification, and Iron Loading

WT and W52 mutant *E. coli* Dps proteins were overexpressed and purified according to previous procedures [11], with one significant modification: the addition of a HiTrap Heparin HP affinity column to ensure removal of endogenous DNA. Proteins were deoxygenated in Schlenk tubes by rapid cycles of vacuum and argon according to previous procedures [11] and brought into the anaerobic chamber. Proteins were then anaerobically incubated with excess ferrous iron to load the ferroxidase sites, with unbound iron removed by size exclusion chromatography [11]. The number of iron ions bound per Dps dodecamer was then quantified by separately measuring the protein and iron concentration. Protein concentrations were measured using either a Bradford assay (Sigma) or ϵ_{280} values calculated using the ExPASy ProtParam tool (<http://web.expasy.org/-protparam/>) with calculated molar absorptivity values for WT, W52A, and W52Y *E. coli* Dps dodecamers of $1.86 \times 10^5 \text{ M}^{-1} \text{ cm}^{-1}$, $1.20 \times 10^5 \text{ M}^{-1} \text{ cm}^{-1}$, and $1.37 \times 10^5 \text{ M}^{-1} \text{ cm}^{-1}$, respectively. Iron concentration was quantified according to $[\text{Fe}(\text{bpy})_3]^{2+}$ absorbance ($\epsilon_{522} = 8790 \text{ M}^{-1} \text{ cm}^{-1}$) using a denaturing method detailed elsewhere [11]. As-purified, Dps was considered to be Apo-Dps with typically $\leq 1 \text{ Fe/Dps}$.

Circular Dichroism of Dps

Protein concentrations were determined using the calculated ϵ_{280} values described above. Spectra were recorded at 25°C on a Model 430 circular dichroism spectrometer (AVIV) in a buffer consisting of 50 mM Tris, pH 7.0, 150 mM NaCl. The spectra shown are the average of three individual scans, with a spectrum of buffer alone subtracted.

EPR Sample Preparation

EPR samples were prepared in an anaerobic chamber using the anaerobic materials outlined above. Samples were loaded into EPR tubes within the anaerobic chamber, sealed with septa, and parafilmmed around the septa seal. Under the conditions used in these experiments, all samples containing both Dps and DNA precipitated, expected behavior associated with Dps condensing DNA. EPR tubes were then brought out of the anaerobic chamber, frozen in liquid nitrogen, and kept in the dark until measurement. Precipitated samples were thoroughly mixed before freezing in liquid nitrogen. For chemically oxidized samples, ferrous iron-loaded protein (approximately 120 μL) was added to the bottom of an EPR tube. Approximately 20 μL of ferricyanide solution was added to the top of the EPR tube, which was then sealed. Upon removal from the anaerobic chamber, the solutions were mixed together and immediately frozen in liquid nitrogen within approximately 5-10 s of the initiation of mixing.

EPR Experiments

EPR spectra were measured on an X-band Bruker EMX spectrometer equipped with an ER4119HS resonator and an Oxford ES9000 cryostat. Instrumental settings are detailed in figure captions, but were generally as follows: modulation amplitude = 10 G at 100 kHz, frequency = 9.37 GHz, microwave power = 6.4 mW, and temperature = 10 K. Samples in Suprasil quartz EPR tubes were irradiated while freezing in liquid nitrogen in an unsilvered Dewar. The excitation source was a xenon lamp equipped with a lens to focus the beam and a 320 nm long-pass filter to remove UV light. Each sample was irradiated for approximately 10 s. For each sample, a dark control (DC) EPR spectrum was first measured at 10 K. The sample was then thawed, mixed, and irradiated while freezing with liquid nitrogen as described. The EPR spectrum of the irradiated sample was then measured under identical instrumental settings. For data analysis, the DC spectrum was smoothed and subtracted from the irradiated sample.

Hydrogen Peroxide Survival Experiments

This protocol is adapted from that reported by Martinez and Kolter [19]. Hydrogen peroxide was purchased from Macron (30% solution). Lyophilized catalase from bovine liver (≥ 20000 units/mg protein) was purchased from Sigma and resuspended in buffer (50 mM K_3PO_4 , pH 7) to make a stock concentration of 0.4 mg/mL. Overnight cultures of the *E. coli* ZK2471 strain (*dps::kan* ΔrecA Δara) containing

WT, W52A, or W52Y pBAD18-dps plasmids were prepared by inoculating single colonies in 5 mL of LB media containing 100 $\mu\text{g}/\text{mL}$ ampicillin and 50 $\mu\text{g}/\text{mL}$ kanamycin. After overnight shaking at 37°C, the cultures were diluted 1:500 into 10 mL of fresh LB media also containing antibiotics. For each WT, W52A, and W52Y, both induced and uninduced 10 mL cultures were prepared: L-arabinose was added to induce Dps overexpression (0.2% w/v final concentration), and an equivalent volume of sterile water was added to uninduced cells. Cultures were then incubated at 37°C with shaking (200 rpm) for 3 h until $\text{OD}_{600} = 0.3\text{-}0.4$ (exponential phase). Separately, the growth of the induced cultures were monitored over 8 h for growth differences. Once reaching exponential phase, cultures were serially diluted in LB media for a total of 10000-fold dilution with a final 1 mL aliquot volume. Hydrogen peroxide was added to these aliquots to attain a final concentrations of 3 or 5 mM in the cell aliquots and mixed by pipetting. After 15 min at RT, catalase solution was added to each aliquot to stop the reaction (50 μL , working concentration: 50 $\mu\text{g}/\text{mL}$ culture) and mixed by pipetting. Cultures were incubated for 15 min after catalase addition to ensure complete hydrogen peroxide reaction. Finally, cultures were plated in 10 μL droplets onto LB agar plates containing ampicillin and kanamycin and incubated at 37°C overnight. The number of colonies in each droplet was manually counted the subsequent day after plate imaging.

2.3 Results

EPR Spectroscopy of WT *E. coli* Dps

In spectroscopic studies with Dps, we expect to observe the oxidation of mononuclear iron sites under the conditions of this study. At the intersubunit ferroxidase sites of Dps, two irons are bound by two conserved histidine ligands and two conserved carboxylate ligands, glutamate and aspartate [1]. This ligand coordination sphere creates two binding sites with very different iron affinities: while one site has a relatively high affinity, the other site binds iron weakly [20]. After binding, ferrous iron is oxidized and shuttled to the core of the protein for storage. Whereas 24-mer ferritins react rapidly with dioxygen as an oxidant, Dps proteins react slowly with dioxygen and much more quickly with hydrogen peroxide [2]. We have previously found that ferricyanide also functions well as a chemical oxidant of *E. coli* Dps in solution [11]. Whereas full occupation of the 12 di-iron centers of the protein would correspond to 24 Fe(II)/Dps, we have found that under the anaerobic conditions used in our experiments (i.e., in the absence of oxidants), *E. coli* Dps binds only 12 Fe(II)/Dps [11]. This loading agrees with studies on *Bacillus anthracis*

and *Listeria innocua* Dps proteins, where a bridging oxidant seems to be required to tether the lower affinity iron and form the di-iron site [20, 21]. Coupled with the specificity of iron binding evidenced by its abrogation in the *E. coli* Dps ferroxidase site double mutant H51G/H63G, the 12 Fe(II)/Dps corresponds to binding only at the higher affinity iron site of each ferroxidase center in the dodecameric protein.

Mononuclear high-spin Fe(III) sites of low symmetry (i.e., nonheme) typically display an EPR signal with an apparent g -value of 4.3, and this is what we observe (Figure 2.2) [22, 23]. This mononuclear high-spin Fe(III) signal at $g = 4.3$ has been frequently reported in the EPR spectra of 24-mer ferritins [24]. The EPR spectrum of iron-bound Dps proteins is consistent but has been reported only once previously [25], and has not yet been reported for *E. coli* Dps.

We first used chemical oxidation to examine the Dps oxidation products we might expect in DNA flash-quench studies. All EPR samples described in this study were prepared anaerobically in order to prevent dioxygen oxidation of ferrous iron loaded Dps. As expected, Apo-Dps, which has not been loaded with iron, and Dps loaded with ferrous iron are EPR-silent (Figure 2.2). However, when WT *E. coli* Dps loaded with 12 Fe(II)/Dps is mixed anaerobically with stoichiometric ferricyanide and frozen in liquid nitrogen, within 5-10 s, a split signal at $g = 4.3$ is observed at low temperature (10 K). Given that ferricyanide has a different g -value and ferrocyanide is EPR-silent, and that the steady-state UV-visible spectrum of ferrous iron-loaded Dps incubated with ferricyanide indicates the formation of oxidized iron species [11], this signal at $g = 4.3$ can be assigned to oxidized ferric iron at the mononuclear ferroxidase site in Dps. This signal was confirmed to be neither power saturated nor overmodulated under the conditions used in this study. No other EPR-active species are apparent in wide spectra from 500 to 4500 gauss (data not shown). When instead the ferrous iron-loaded Dps was incubated with ferricyanide for much longer times, no EPR-active species were observed (data not shown), likely because the oxidized iron was translocated to the core of the protein, forming EPR-silent polynuclear species.

Next, we investigated the oxidation of DNA-bound WT Dps following DNA photooxidation via the flash-quench technique. We compare the yield of Dps oxidation with the alternating copolymers poly(dGdC)₂ and poly(dAdT)₂ in order to determine if guanine radical is an important intermediate in Dps oxidation. Here, the sample is irradiated in an EPR tube while freezing in liquid nitrogen in a clear dewar in order to trap reactive intermediates. For each sample, an individual dark con-

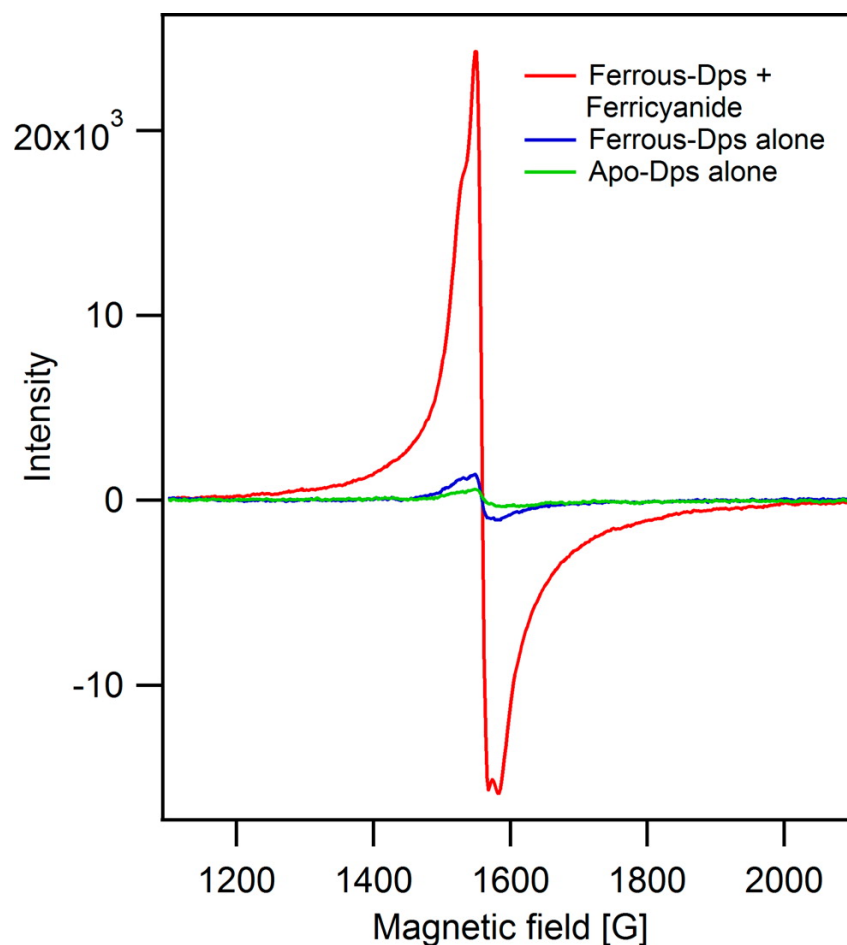


Figure 2.2: Chemical oxidation of WT *E. coli* Dps containing 12 Fe(II)/Dps with stoichiometric ferricyanide. Conditions: Dps concentration: $20 \mu\text{M}$; Fe/Dps: 11.9 ± 0.2 ; Buffer: 50 mM Tris, pH 7, 150 mM NaCl, 5% glycerol. Instrument settings: modulation amplitude = 10 G at 100 kHz; frequency = 9.373 GHz; microwave power = 6.4 mW; and temperature = 10 K.

trol (DC) was measured at low temperature (10 K). The sample was then thawed, mixed, and irradiated while freezing to generate oxidative DNA damage via the flash-quench technique. Efforts were made to irradiate all samples under identical conditions for 10 s. The EPR spectrum of the irradiated sample was then remeasured under identical instrument settings. All spectra shown in Figure 2.3 have had an individual DC subtracted; thus, all features are a function of irradiation.

In a sample containing $20 \mu\text{M}$ Dps loaded with 12 Fe(II)/Dps, poly(dGdC)₂ at a concentration of 1 mM base-pairs, $20 \mu\text{M}$ noncovalent $[\text{Ru}(\text{phen})(\text{dppz})(\text{bpy}')]^{2+}$ and $120 \mu\text{M}$ $[\text{Co}(\text{NH}_3)_5\text{Cl}]^{2+}$ in a buffer of 50 mM Tris, pH 7.0, 150 mM NaCl, 5% glycerol, a split nearly isotropic signal at $g = 4.3$ is observed upon irradiation

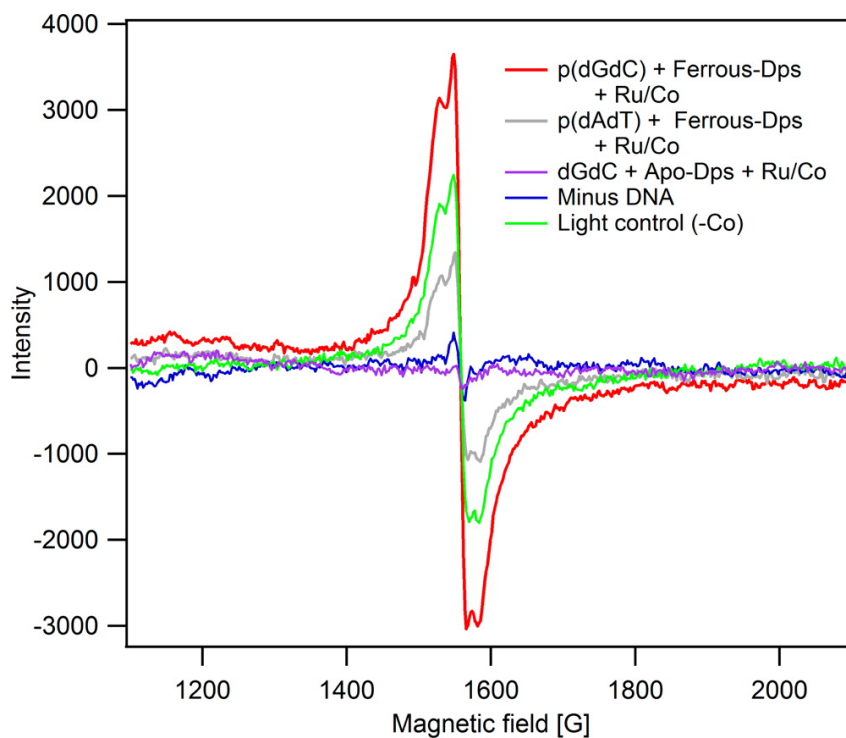


Figure 2.3: DNA-bound WT *E. coli* Dps oxidation via the flash-quench technique. All spectra have had an individual unirradiated spectrum subtracted; thus all features are a function of irradiation. Concentrations: 20 μM Dps (Fe(II)/Dps: 11.9 ± 0.2), 1 mM base-pairs poly(dGdC)₂ or poly(dAdT)₂ DNA, 20 μM [Ru(phen)(dppz)(bpy')]²⁺, 120 μM [Co(NH₃)₅Cl]²⁺. Buffer: 50 mM Tris, pH 7.0, 150 mM NaCl, 5% glycerol. Minus DNA sample contains ferrous iron-loaded Dps, Ru, and Co, but lacks DNA; Light control contains ferrous iron-loaded Dps, poly(dGdC)₂ DNA, and Ru, but lacks Co quencher. Instrument settings: modulation amplitude = 10 G at 100 kHz; frequency = 9.37 GHz; microwave power = 6.4 mW; and temperature = 10 K.

(Figure 2.3). Comparison with the chemically oxidized sample indicates that this species corresponds to oxidized ferric iron at the mononuclear ferroxidase site in Dps that was formed after DNA oxidation with the ruthenium photooxidant. DC subtracted spectra in this trial were quantified by double integration over the range of 1400 to 1700 gauss. Consistent trends were seen in two separate trials. In contrast to the full sample (containing poly(dGdC)₂ DNA, ferrous iron-loaded Dps, Ru photooxidant, and Co quencher), an 8-fold decreased signal was observed in a sample lacking DNA (Minus DNA). An attenuated signal was also observed in an irradiated sample that contained ferrous iron-loaded Dps, poly(dGdC)₂, and [Ru(phen)(dppz)(bpy')]²⁺ but lacked quencher (Light control). Some signal was observed in the light control sample (1.7-fold less than the full sample), even though

steady-state room temperature luminescence experiments with mixed-sequence 70-mer duplex DNA containing covalently tethered $[\text{Ru}(\text{phen})(\text{dppz})(\text{bpy}')]^{2+}$ indicated that Dps does not quench the ruthenium(II) excited state.[11] When Apo-Dps is substituted for Dps loaded with ferrous iron, no signal at $g = 4.3$ is observed, confirming protein-bound iron as the origin of this signal. Importantly, when poly(dAdT)₂ is substituted for poly(dGdC)₂, the observed signal is significantly attenuated (3.0-fold), suggesting that guanine radicals play a role in Dps oxidation.

Structure and Fe Binding of W52 Dps Mutants

The Dps monomer is composed of a four helix bundle with two helix-turn-helix motifs [26]. The far-UV circular dichroism (CD) spectra of WT Apo-Dps is consistent with this α -helical structure [27](Figure 2.4). Comparison of the WT, W52A, and W52Y Dps CD spectra show that overall protein folding is relatively unaffected by these mutations.

Iron binding at the ferroxidase site was also investigated for both mutations. As previously described for WT Dps [11], the proteins were incubated anaerobically with excess ferrous iron and unbound iron was subsequently removed with size exclusion chromatography. The number of irons bound per Dps dodecamer was then quantified by the formation of $[\text{Fe}(\text{bpy})_3]^{2+}$ after protein denaturation and addition of reductant and 2,2'-bipyridine. When Dps concentration is measured via the Bradford reagent or calculated ϵ_{280} values, the Fe(II)/Dps can be quantified. In one trial, the WT protein bound 14.6 ± 0.5 Fe(II)/Dps, whereas the W52A and W52Y mutants bound only 8.6 ± 0.4 and 10.6 ± 0.4 Fe(II)/Dps, respectively. Equivalent results were obtained in other trials. Note that small increases from 12 Fe(II)/Dps in the WT protein are likely due to a minor degree of oxidation due to trace oxygen, allowing for some di-iron site formation. Figure 2.4 shows the $[\text{Fe}(\text{bpy})_3]^{2+}$ spectra normalized to protein concentration for WT, W52A, and W52Y Dps. W52A Dps binds iron on the order of 60% of WT, while W52Y is slightly better, binding 70% of the iron of WT Dps. Thus, iron binding is somewhat attenuated, but not abrogated, for these mutations. Furthermore, these W52 mutations are not expected to affect the DNA binding of Dps; previous work demonstrated that iron-loaded Dps binds DNA similarly to the Apo-protein [11]. Additionally, we observed the same level of precipitation and DNA condensation with the W52 mutants and WT.

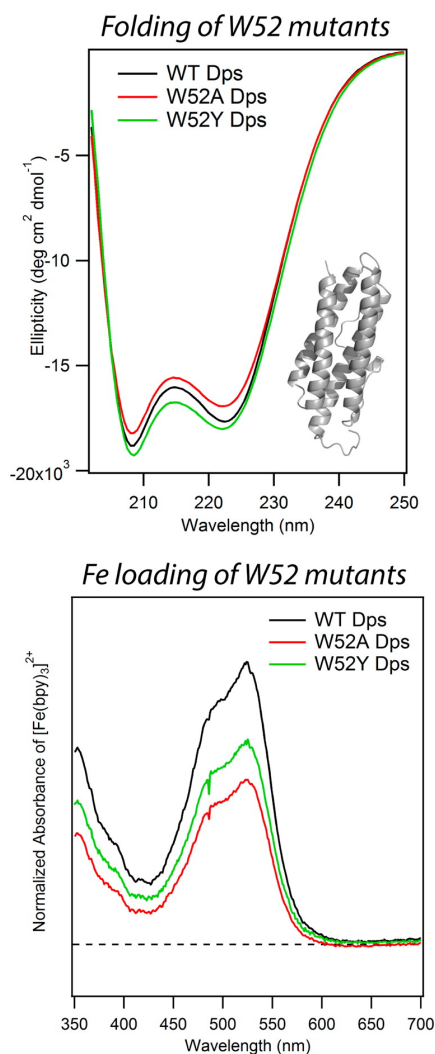


Figure 2.4: Folding and iron loading of W52 Dps mutants. (Upper) Circular dichroism spectra of wild-type (WT) (black), W52A (red), and W52Y (green) *E. coli* Apo-Dps. Dps monomer depicted in gray, showing α -helical structure (PDB: 1DPS). Protein concentration was $5 \mu\text{M}$ in a buffer of 50 mM Tris, pH 7.0, 150 mM NaCl. (Lower) Ferrous iron loading of Dps W52 mutants compared to WT *E. coli* protein. Normalized UV-vis spectra of $[\text{Fe}(\text{bpy})_3]^{2+}$ produced from either WT Dps (black), W52A Dps (red), or W52Y Dps (green). For normalization, the absorbance values were divided by protein concentration. The calculated number of iron atoms per Dps dodecamer is 14.6 ± 0.5 for WT Dps, 8.6 ± 0.4 for W52A, and 10.6 ± 0.4 for W52Y. Protein concentrations were determined as given in the Materials and Methods Section.

EPR Results Comparing WT Dps with W52 Mutants

The ability of ferrous iron-loaded W52A and W52Y Dps to be oxidized by ferricyanide, a diffusing oxidant, was first explored using EPR spectroscopy. Figure

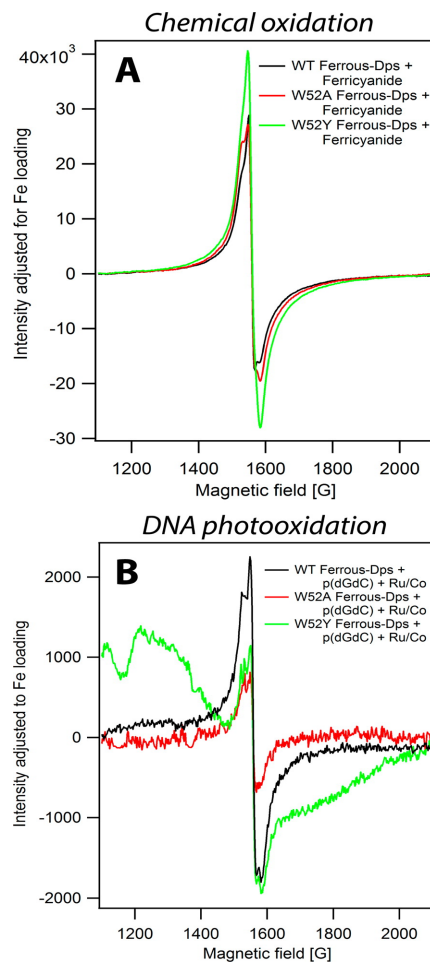


Figure 2.5: Comparison of chemical oxidation of ferrous iron-loaded Dps with ferricyanide, and oxidation following DNA photooxidation. EPR intensity for the Dps mutants was adjusted to that of the WT protein via dividing by the ratio Fe_{W52}/Fe_{WT} . (A) Oxidation by 2-fold excess ferricyanide: 20 μ M Dps (Fe^{2+}/Dps : WT: 13.6 ± 0.2 , W52A: 8.8 ± 0.2 ; W52Y: 11.3 ± 0.1), 480 μ M ferricyanide. (B) Comparison of ferrous iron-loaded WT Dps and W52A/Y mutant following DNA photooxidation. All spectra have had an individual unirradiated spectrum subtracted. Concentrations: 20 μ M Dps (Fe^{2+}/Dps : WT: 16.0 ± 0.5 , W52A: 10.1 ± 0.2 ; W52Y: 11.5 ± 0.2), 1 mM base-pairs poly(dGdC)₂ DNA, 20 μ M [Ru(phen)(dppz)(bpy')]²⁺, 120 μ M [Co(NH₃)₅Cl]²⁺. 50 mM Tris, pH 7.0, 150 mM NaCl, 5% glycerol. Modulation amplitude = 10 G in (A) and 5 G in (B) at 100 kHz; frequency = 9.37 GHz; microwave power = 6.4 mW; and temperature = 10 K.

2.5A shows oxidation of the W52 mutants compared to WT with excess ferricyanide, with the EPR intensity adjusted for iron loading (i.e., $Intensity/(Fe_{W52A}/Fe_{WT})$). When the intensity of the EPR signal resulting from ferricyanide oxidation is adjusted for iron loading in this manner, the W52 mutants show similar yields of iron oxidation

to WT Dps, with W52Y showing a slightly increased signal relative to WT. This result indicates that oxidation of the mononuclear iron site by a diffusing oxidant is not affected in W52A and W52Y Dps compared to WT.

Next, the X-band EPR spectrum of ferrous iron-loaded WT *E. coli* Dps was compared to W52A and W52Y Dps upon DNA photooxidation using the flash-quench technique. Samples containing ferrous iron-loaded Dps, poly(dGdC)₂ DNA, non-covalent [Ru(phen)(dppz)(bpy')]²⁺ and [Co(NH₃)₅Cl]²⁺ were irradiated for identical lengths of time. The yield of iron oxidation at $g = 4.3$ was attenuated in the W52 mutants compared to the WT protein, even when adjusted for iron loading (Figure 2.5B). Overall smaller signals in Figure 2.5B compared to the WT spectra in Figure 2.3 are due to a lower modulation amplitude in the former (5 and 10 G, respectively), while the intensity difference between Figure 2.5, parts A and B, is likely due to a poor kinetic window and inefficiency in irradiation for observing DNA photooxidation. When the DC-subtracted, adjusted spectra are quantified by double integration from 1400 to 1600 gauss, the W52A iron signal is 3.4-fold less than WT, while the W52Y signal is 1.8-fold less than WT. The proficiency in oxidation of the iron sites in these W52 Dps mutants by a chemical oxidant that directly diffuses to the iron site, combined with the deficiency in the yield of iron oxidation upon DNA photooxidation, suggests that W52 could play a role in mediating ET from the iron site to the DNA. As with WT Dps, we do not have the time resolution to observe a tryptophan or tyrosine radical directly using EPR spectroscopy.

It is noteworthy that the EPR spectra of DC samples (i.e., before irradiation) of the W52 mutants show evidence of Co²⁺ formation, whereas the WT protein does not (Figure A.4). The cobalt quencher, [Co(NH₃)₅Cl]²⁺, is a low-spin Co³⁺ d⁶ species with $S = 0$. Upon reduction to Co²⁺, the complex becomes labile, forming [Co(H₂O)₆]²⁺, a high-spin d⁷ species with $S = 3/2$ (EPR-active). Therefore, there may be some direct electron transfer from the ferrous mononuclear iron site to the Co³⁺ quencher to yield EPR-active Co²⁺ in these mutants, perhaps because the ferroxidase site is more solvent-accessible. However, there is very little evidence of ferric iron formation in the DC spectrum of the W52A mutant, and in W52Y, a relatively small percentage of the total amount of iron in the sample is oxidized, allowing ample room for an increase upon irradiation. Thus, the lower yield of iron oxidation that we observe upon DNA photooxidation with the W52 mutants is significant, supporting our EPR results that suggest W52 as an electron transfer intermediate in Dps.

Hydrogen Peroxide Survival Assay

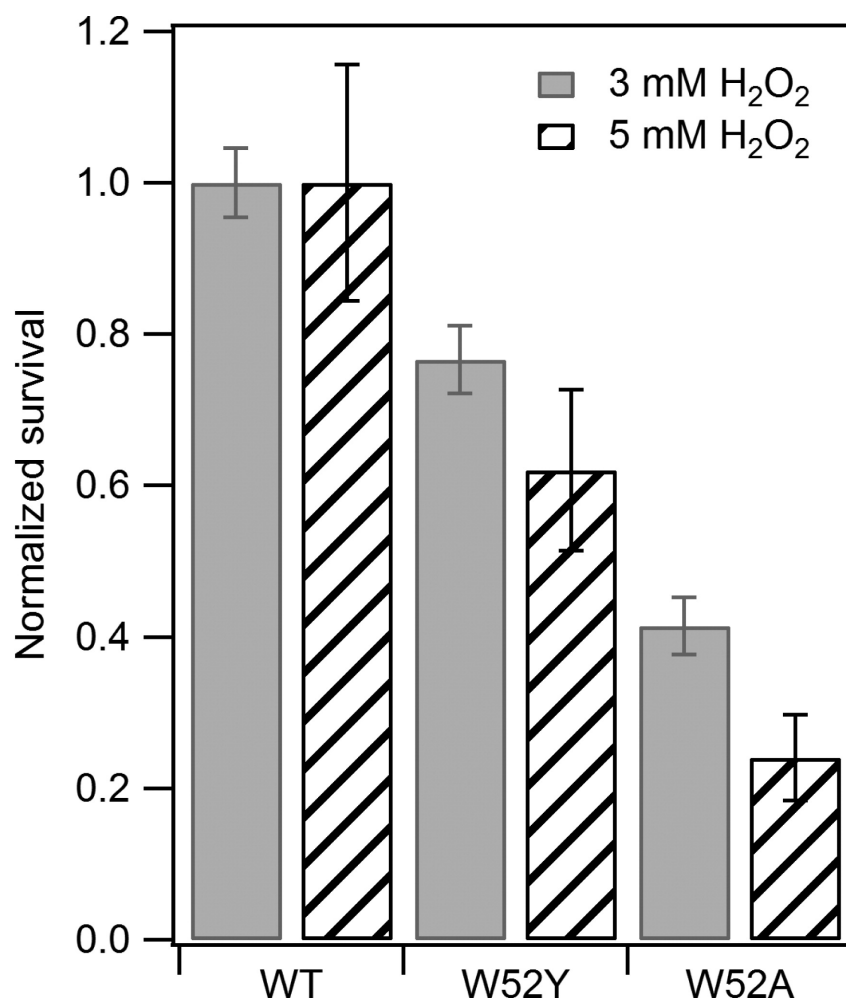


Figure 2.6: Hydrogen peroxide survival assay comparing *E. coli* with WT, W52Y, or W52A Dps. Dps has been induced with 0.2% w/v L-arabinose and cells treated with either 3 (solid gray bars) or 5 (dashed bars) mM hydrogen peroxide. Percent survival was calculated as the fraction of surviving colonies over the number of CFUs seeded (seeded CFUs calculated by dilution-adjusted OD600 readings). Each mutant data set was normalized to the WT survival percentage. The standard error of the mean was calculated by treating each droplet as a data point.

The biological consequence of mutating W52 was also investigated by measuring the survival of *E. coli* upon exposure to hydrogen peroxide for cells containing WT, W52A, or W52Y Dps. The *dps* knockout *E. coli* strain (*dps::kan ΔrecA Δara*) (ZK2471) was transformed with a pBAD18 plasmid containing either the *E. coli* WT, W52A, or W52Y *dps* gene under the control of an inducible promoter. In the absence of hydrogen peroxide at the inducer concentrations used in this study, no growth difference was observed between the strains (Figure A.5).

Adapted from the method of Martinez and Kolter [19], cells were grown overnight and diluted into fresh media with the addition of either the inducer (+), L-arabinose, or sterile water (-). Cells were then grown to exponential phase ($OD_{600} = 0.3-0.4$) and challenged with 3 or 5 mM hydrogen peroxide. After quenching the reaction with catalase, cells were diluted and plated in multiple droplets to quantify colony forming units (CFU). The results from the 0.2% w/v of L-arabinose inducer at 10000-fold dilution are shown in Figure 2.6. Percent survival was calculated as the fraction of surviving colonies over the number of seeded CFUs as calculated by dilution-adjusted OD_{600} readings. Each mutant data set was then normalized to the WT survival percentage. The standard error of the mean was calculated by treating each droplet as a data point ($n = 16$). Raw data are shown in Figure A.6. As was previously observed [19], there is also a clear difference in bacterial survival after treatment with hydrogen peroxide between induced and uninduced cells (Figure A.7), demonstrating that Dps is needed for protection.

As is evident in Figure 2.6, cells containing W52Y Dps survive the hydrogen peroxide challenge more effectively than those with W52A Dps. Additionally, the relative percent survival varies with hydrogen peroxide concentration. Whereas at 3 mM H_2O_2 , cells containing W52Y and W52A Dps survive at levels 77% and 41% of WT, respectively, when cells are further challenged by 5 mM hydrogen peroxide, survival drops to 62% of WT for W52Y and 2% for W52A Dps cells. Thus, W52 is an essential player for cells containing Dps to survive this hydrogen peroxide challenge. There is certainly a component of Dps Fe loading proficiency (W52Y and W52A Dps bind iron at approximately 70% and 60%, respectively, of WT, see above) in this survival. However, the difference between observed survival and Dps Fe loading, combined with the variation of survival with H_2O_2 concentration shows that an additional component also affects survival; we propose that this factor may be the efficiency of DNA CT. Furthermore, this *in vivo* trend (WT > W52Y > W52A) parallels what we observe in EPR experiments, where the largest attenuation in the yield of iron oxidation following DNA photooxidation is seen with W52A Dps. The correlation between our EPR and *in vivo* experiments supports our proposal that survival depends on both Dps Fe loading proficiency and the efficiency of DNA CT.

2.4 Discussion

In earlier studies, we have shown biochemically that ferrous iron-loaded *E. coli* Dps can protect DNA from oxidative damage generated using the flash-quench technique [11]. The absence of this protective ability in Apo-Dps and Dps loaded with ferric iron, which both lack available reducing equivalents, suggested that ferrous-iron loaded Dps protects DNA by becoming oxidized via DNA CT to fill guanine radical holes. Here using EPR, we show directly the oxidation of WT ferrous iron-loaded *E. coli* Dps following DNA photooxidation generated by the flash-quench technique. Because Dps is loaded with one ferrous iron per ferroxidase site, this oxidation is evidenced by the appearance of mononuclear ferric iron species of low symmetry at an apparent g-value of 4.3. This signal is absent in controls without DNA and is attenuated in the irradiated control that lacks the diffusing quencher necessary for oxidation by flash-quench.

The results described here furthermore support the idea that guanine radicals facilitate Dps oxidation. When poly(dGdC)₂ is substituted with poly(dAdT)₂, the yield of Dps oxidation is decreased significantly. A similar dependence on guanine radicals was observed in the oxidation of the 4Fe4S cluster of the base excision repair protein MutY following DNA photooxidation by flash-quench [12]. More efficient protein oxidation by guanine radicals is likely a kinetic effect. Back electron transfer processes generally decrease the observed yield of oxidized protein using the flash-quench technique. Adenine radicals would be expected to have short lifetimes compared to the neutral guanine radical, which persists for milliseconds [28]. Thus, as was described for MutY [12], it appears likely that guanine radical formation allows more time for the oxidation of Dps by better competing with rapid back electron transfer to the intercalated ruthenium photooxidant, resulting in higher yields of Dps oxidation with guanine radical as an intermediate. Additionally, poorly stacked ATAT tracts do not conduct charge efficiently [29]; this poor CT may also be a factor in the lower yield of protein oxidation with poly(dAdT)₂ DNA. Generally, the more favorable oxidation of Dps by guanine radicals also supports a sequential process, using DNA-mediated CT, where, after guanine radicals are produced, Dps is oxidized to fill guanine radical holes.

Can we also obtain information concerning the path for electron transfer? In 12-mer Dps proteins, there is a conserved tryptophan residue in close proximity to the ferroxidase site (W52 in the *E. coli* protein), whereas 24-mer ferritins contain a conserved tyrosine residue. In both cases, this aromatic residue has been proposed

to act as a molecular capacitor, providing an extra electron during iron oxidation in order to prevent formation of oxygen radicals [15]. The location of the conserved tryptophan residue in Dps proteins between the ferroxidase site and protein surface suggests a possible role for the tryptophan as an electron transfer hopping intermediate in the DNA-mediated oxidation of the iron site.

Here we use site-directed mutagenesis, creating W52A and W52Y *E. coli* Dps, to investigate this possibility. While overall protein folding seems unaffected by these mutations, iron binding is somewhat attenuated. When adjusted for iron loading, the yield of Dps oxidation by a diffusing oxidant, ferricyanide, is not attenuated by these W52 mutations. However, even adjusted for iron loading, the level of iron oxidation observed in EPR experiments upon DNA photooxidation for both W52A and W52Y Dps is significantly reduced with respect to the WT protein, with a more significant attenuation for W52A Dps. These observations suggest that W52 may play a role in mediating CT from the iron site to DNA. Because (i) the intercalating ruthenium photooxidant is a one-electron oxidant, and (ii) the mononuclear iron site has a much lower redox potential (as indicated by its oxidation by ferricyanide, 0.43 V versus NHE) [30] than tryptophan or tyrosine, making it the thermodynamic sink, the deficiency in iron oxidation for these mutants suggests a role for W52 as an electron transfer hopping intermediate rather than as a molecular capacitor.

While we may understand how the W52A mutation might inhibit CT by deleting the aromatic residue that mediates electronic coupling, why might substitution of tryptophan with an aromatic tyrosine residue have such an effect? Work by Gray and co-workers has revealed that precise tuning of the reduction potential of hopping intermediates is essential for function [31, 32]. With tyrosine, the reduction potential can be modulated by adjacent basic amino acids such as His, Asp, or Glu that can hydrogen bond with the OH group of tyrosine [31]. In *E. coli* Dps, no basic residues are in the vicinity of Y52 except for the ferroxidase site ligands, which are presumably coordinating iron. Therefore, the Dps protein environment may support a tryptophan radical but not be as amenable to a tyrosine radical at the reduction potentials necessary for a hopping intermediate.

We also probed the role of *E. coli* W52 Dps in cells through tests of cell survival under stress of hydrogen peroxide. Bacteria containing WT Dps are best able to survive this oxidative stress. Whereas there is some attenuation in survival seen for cells containing W52Y Dps, cells containing W52A Dps show significantly

diminished survival. It appears then that the conserved tryptophan residue in close proximity to the ferroxidase site in Dps proteins is important for bacteria containing Dps to survive under conditions of oxidative stress. This survival likely depends on both the Dps iron loading proficiency and an additional factor that we propose to be the ability of the Dps protein to facilitate efficient DNA CT. Moreover, the survival trend that we observe in bacteria under oxidative stress mirrors the Dps photooxidation proficiency observed in EPR experiments. Thus, some of this *in vivo* effect may be due to inhibition of the DNA-mediated oxidation of Dps upon mutation of W52. Perhaps Y52 can still act as a molecular capacitor inside cells, preventing ROS formation in the hydrogen peroxide oxidation of mononuclear iron sites, but it is less able to act as a hopping intermediate because of nonoptimal protein environment. A52 would be unable to fulfill either function in Dps proteins, and it is interesting that this mutant shows the most deficiency in survival. Overall, mutations to W52 in *E. coli* Dps impair the ability of the bacteria to survive oxidative stress, and we hypothesize that a component of this deficiency derives from a decreased ability to mediate ET from the iron site of Dps to the DNA.

2.5 Conclusions

Dps proteins are involved in the survival and virulence of pathogenic bacteria in response to oxidative stress generated by the host immune system and antibiotics [33–40]. Elucidating the mechanism of Dps protection of the genomes of pathogenic bacteria may inform the development of new antibiotic therapies. A long-distance Dps protection mechanism via DNA CT could be an efficient strategy for maintaining the integrity of genomic DNA. In this work, we further explore the DNA-mediated oxidation of the bacterial ferritin Dps. We use EPR to characterize spectroscopically the oxidation of ferrous iron-loaded Dps following DNA photooxidation via the flash-quench technique. We find that guanine sequences facilitate Dps oxidation. Furthermore, we explore possible ET intermediates within the Dps protein fold in the DNA-mediated oxidation, focusing on a conserved tryptophan residue in close proximity to the ferroxidase site of Dps proteins. In EPR experiments, the yield of Dps oxidation upon DNA photooxidation is significantly attenuated for W52A Dps compared to the WT protein. This effect is reflected *in vivo* in *E. coli* survival in response to hydrogen peroxide, suggesting that some of this *in vivo* survival decrease could be due to inhibition of the DNA-mediated oxidation of Dps upon mutation of W52.

Thus, we have moved toward understanding the role that DNA CT may play

with Dps proteins inside cells. Interestingly, Dps seems to act as a checkpoint during oxidative stress to delay the initiation of DNA replication in *E. coli* until oxidative DNA damage has been repaired [41]. This interplay of DNA protection by Dps with repair and replication may be considered in the context of long-range signaling through DNA CT.[6] Certainly the function of Dps proteins in the long-range DNA-mediated protection of the genome from oxidative assault requires further consideration as targets in the treatment of pathogenic bacteria.

References

- (1) Chiancone, E.; Ceci, P. *Biochimica et Biophysica Acta (BBA) - General Subjects* **2010**, *1800*, 798–805.
- (2) Zhao, G.; Ceci, P.; Ilari, A.; Giangiacomo, L.; Laue, T. M.; Chiancone, E.; Chasteen, N. D. *J. Biol. Chem.* **2002**, *277*, 27689–27696.
- (3) Ceci, P.; Cellai, S.; Falvo, E.; Rivetti, C.; Rossi, G. L.; Chiancone, E. *Nucleic Acids Res* **2004**, *32*, 5935–5944.
- (4) Altuvia, S.; Almiron, M.; Huisman, G.; Kolter, R.; Storz, G. *Molecular Microbiology*, *13*, 265–272.
- (5) Wolf, S. G.; Frenkiel, D.; Arad, T.; Finkel, S. E.; Kolter, R.; Minsky, A. *Nature* **1999**, *400*, 83–85.
- (6) Grodick, M. A.; Muren, N. B.; Barton, J. K. *Biochemistry* **2015**, *54*, 962–973.
- (7) Boal, A. K.; Genereux, J. C.; Sontz, P. A.; Gralnick, J. A.; Newman, D. K.; Barton, J. K. *Proc. Natl. Acad. Sci. U.S.A.* **2009**, *106*, 15237–15242.
- (8) Saito, I.; Nakamura, T.; Nakatani, K.; Yoshioka, Y.; Yamaguchi, K.; Sugiyama, H. *J. Am. Chem. Soc.* **1998**, *120*, 12686–12687.
- (9) Arkin, M. R.; Stemp, E. D. A.; Coates Pulver, S.; Barton, J. K. *Chemistry & Biology* **1997**, *4*, 389–400.
- (10) Slinker, J. D.; Muren, N. B.; Renfrew, S. E.; Barton, J. K. *Nat Chem* **2011**, *3*, 230–235.
- (11) Arnold, A. R.; Barton, J. K. *J. Am. Chem. Soc.* **2013**, *135*, 15726–15729.
- (12) Yavin, E.; Boal, A. K.; Stemp, E. D. A.; Boon, E. M.; Livingston, A. L.; O'Shea, V. L.; David, S. S.; Barton, J. K. *Proc Natl Acad Sci U S A* **2005**, *102*, 3546–3551.
- (13) Ren, B.; Tibbelin, G.; Kajino, T.; Asami, O.; Ladenstein, R. *Journal of Molecular Biology* **2003**, *329*, 467–477.
- (14) Winkler, J. R.; Gray, H. B. *Chem. Rev.* **2014**, *114*, 3369–3380.
- (15) Bellapadrona, G.; Ardini, M.; Ceci, P.; Stefanini, S.; Chiancone, E. *Free Radical Biology and Medicine* **2010**, *48*, 292–297.
- (16) Ebrahimi, K. H.; Hagedoorn, P.-L.; Hagen, W. R. *ChemBioChem*, *14*, 1123–1133.
- (17) Sovenyhazy, K. M.; Bordelon, J. A.; Petty, J. T. *Nucleic Acids Res* **2003**, *31*, 2561–2569.
- (18) Anderson, P. A.; Deacon, G. B.; Haarmann, K. H.; Keene, F. R.; Meyer, T. J.; Reitsma, D. A.; Skelton, B. W.; Strouse, G. F.; Thomas, N. C. *Inorg. Chem.* **1995**, *34*, 6145–6157.

- (19) Martinez, A.; Kolter, R. *J. Bacteriol.* **1997**, *179*, 5188–5194.
- (20) Su, M.; Cavallo, S.; Stefanini, S.; Chiancone, E.; Chasteen, N. D. *Biochemistry* **2005**, *44*, 5572–5578.
- (21) Schwartz, J. K.; Liu, X. S.; Tosha, T.; Diebold, A.; Theil, E. C.; Solomon, E. I. *Biochemistry* **2010**, *49*, 10516–10525.
- (22) Bou-Abdallah, F.; Chasteen, N. D. *J Biol Inorg Chem* **2008**, *13*, 15–24.
- (23) Gibson, J. F. In *ESR and NMR of Paramagnetic Species in Biological and Related Systems*; Nato Advanced Study Institutes Series; Springer, Dordrecht: 1980, pp 225–253.
- (24) Sun, S.; Chasteen, N. D. *Biochemistry* **1994**, *33*, 15095–15102.
- (25) Ardini, M.; Fiorillo, A.; Fittipaldi, M.; Stefanini, S.; Gatteschi, D.; Ilari, A.; Chiancone, E. *Biochimica et Biophysica Acta (BBA) - General Subjects* **2013**, *1830*, 3745–3755.
- (26) Grant, R. A.; Filman, D. J.; Finkel, S. E.; Kolter, R.; Hogle, J. M. *Nature Structural & Molecular Biology* **1998**, *5*, 294–303.
- (27) Kelly, S. M.; Jess, T. J.; Price, N. C. *Biochimica et Biophysica Acta (BBA) - Proteins and Proteomics* **2005**, *1751*, 119–139.
- (28) Stemp, E. D. A.; Arkin, M. R.; Barton, J. K. *J. Am. Chem. Soc.* **1997**, *119*, 2921–2925.
- (29) O’Neil, M. A.; Barton, J. K. *J. Am. Chem. Soc.* **2004**, *126*, 11471–11483.
- (30) Dutton, P. L. *Meth. Enzymol.* **1978**, *54*, 411–435.
- (31) Warren, J. J.; Winkler, J. R.; Gray, H. B. *FEBS Letters*, *586*, 596–602.
- (32) Shih, C.; Museth, A. K.; Abrahamsson, M.; Blanco-Rodriguez, A. M.; Bilio, A. J. D.; Sudhamsu, J.; Crane, B. R.; Ronayne, K. L.; Towrie, M.; Vlček, A.; Richards, J. H.; Winkler, J. R.; Gray, H. B. *Science* **2008**, *320*, 1760–1762.
- (33) Sund, C. J.; Rocha, E. R.; Tzianabos, A. O.; Tzinabos, A. O.; Wells, W. G.; Gee, J. M.; Reott, M. A.; O’Rourke, D. P.; Smith, C. J. *Mol. Microbiol.* **2008**, *67*, 129–142.
- (34) Li, X.; Pal, U.; Ramamoorthi, N.; Liu, X.; Desrosiers, D. C.; Eggers, C. H.; Anderson, J. F.; Radolf, J. D.; Fikrig, E. *Molecular Microbiology* **2007**, *63*, 694–710.
- (35) Satin, B.; Del Giudice, G.; Della Bianca, V.; Dusi, S.; Laudanna, C.; Tonello, F.; Kelleher, D.; Rappuoli, R.; Montecucco, C.; Rossi, F. *J. Exp. Med.* **2000**, *191*, 1467–1476.
- (36) Halsey, T. A.; Vazquez-Torres, A.; Gravdahl, D. J.; Fang, F. C.; Libby, S. J. *Infect. Immun.* **2004**, *72*, 1155–1158.

- (37) Pang, B.; Hong, W.; Kock, N. D.; Swords, W. E. *Front Cell Infect Microbiol* **2012**, *2*, 58.
- (38) Theoret, J. R.; Cooper, K. K.; Zekarias, B.; Roland, K. L.; Law, B. F.; Curtiss, R.; Joens, L. A. *Clin. Vaccine Immunol.* **2012**, *19*, 1426–1431.
- (39) Olsen, K. N.; Larsen, M. H.; Gahan, C. G. M.; Kallipolitis, B.; Wolf, X. A.; Rea, R.; Hill, C.; Ingmer, H. *Microbiology (Reading, Engl.)* **2005**, *151*, 925–933.
- (40) Calhoun, L. N.; Kwon, Y. M. *Int. J. Antimicrob. Agents* **2011**, *37*, 261–265.
- (41) Chodavarapu, S.; Gomez, R.; Vicente, M.; Kaguni, J. M. *Mol. Microbiol.* **2008**, *67*, 1331–1346.

Chapter 3

DIRECT ELECTROCHEMICAL INVESTIGATIONS OF
CHARGED POINT MUTATIONS ON THE REDOX POTENTIAL
OF ENDONUCLEASE III

Adapted with permission from:

- (1) Bartels, P. L.; Zhou, A.; Arnold, A. R.; Nuñez, N. N.; Crespilho, F. N.; David, S. S.; Barton, J. K. *Langmuir* **2017**, *33*, 2523–2530.
Copyright 2018 American Chemical Society.

A. Zhou, A. Arnold, and N. Nuñez prepared proteins for experiments. P. Bartels performed all electrochemical experiments with assistance from F. Crespilho and A. Zhou.

3.1 Introduction

E. coli endonuclease III (EndoIII) is a DNA glycosylase that excises oxidized pyrimidines from DNA, functioning as part of the base excision repair (BER) pathway in order to maintain the integrity of the genome [1]. EndoIII contains a $[4\text{Fe}4\text{S}]^{2+}$ cluster that is relatively insensitive to reduction and oxidation in solution [2]; as a result, it was initially proposed that the cluster served only a structural role within the protein. MutY is another *E. coli* BER glycosylase, homologous to EndoIII, that also contains a $[4\text{Fe}4\text{S}]^{2+}$ cluster [3]. MutY, found in organisms from bacteria to man, is involved in the repair of oxoG:A mismatches [4]; in humans, inherited defects in MUTYH are associated with a familial form of colon cancer known as MUTYH-associated polyposis (MAP) and many MAP-associated variants are localized near the $[4\text{Fe}4\text{S}]$ cluster [4]. Furthermore, in the case of MutY, it has been shown that the cluster is not required for folding or stability [3], or direct participation in the intrinsic glycosidic bond hydrolysis catalysis [5], making the widespread presence of conserved, noncatalytic $[4\text{Fe}4\text{S}]$ clusters difficult to explain.

Notably, the earliest studies with EndoIII and MutY looked only at free protein in solution, neglecting the effect of DNA binding on redox potential. Experiments carried out on DNA-modified electrodes have demonstrated that, in both EndoIII and MutY, the cluster undergoes a negative shift in potential associated with binding to the DNA polyanion and is activated toward reversible redox activity [6]. In these experiments, DNA monolayers were formed on gold electrodes, and upon addition of EndoIII or MutY, a reversible signal with a midpoint potential ranging from 60 to 95 mV versus NHE was observed. Importantly, the introduction of just a single mismatch or abasic site into DNA led to signal attenuation, showing that electron transfer between the protein and the electrode was through the π -stacked base pairs in a process known as DNA-mediated charge transport (DNA CT) [7]. In this process, charge is funneled from the electrode surface through the π -stack of the DNA bases to reach the redox probe (a protein in this case); the only requirement is that the probe must be electronically coupled to the DNA π -stack. Remarkably, the sensitivity to base stacking observed with EndoIII and MutY was comparable to that obtained using small molecules such as Nile blue or methylene blue that intercalate directly into the base stack.

The expanded potential window of highly oriented pyrolytic graphite (HOPG) and the ability to form pyrene-modified DNA films on the surface made it possible to directly compare the potential of proteins in the presence and absence of DNA [8].

Experiments with EndoIII revealed that DNA binding shifts the reduction potential of the $[4\text{Fe}_4\text{S}]^{3+/2+}$ couple by -200 mV to favor oxidation. Thermodynamically, this shift corresponded to a large (~3 orders of magnitude) increase in the DNA binding affinity of the oxidized form of the protein. Crystal structures of EndoIII and MutY with and without DNA do not show any significant structural change upon DNA binding [9–12], so this dramatic result was attributed to a combination of electrostatic effects resulting from the negatively charged DNA backbone and decreased solvent accessibility of the cluster in DNA-bound protein, which is in agreement with the known sensitivity of $[4\text{Fe}_4\text{S}]$ clusters to their local environment [13]. By demonstrating that DNA binding brought the redox potential of EndoIII into a biologically relevant window, this result served to explain the previously observed redox insensitivity of free EndoIII and provided evidence in favor of a redox role for the DNA-bound protein cluster.

Since these experiments were carried out, a wide range of DNA processing enzymes have been revealed to contain $[4\text{Fe}_4\text{S}]$ clusters with properties similar to EndoIII and MutY. These include the *Archaeoglobus fulgidus* uracil DNA glycosylase (UDG), archaeal and eukaryotic versions of the nucleotide excision repair helicase XPD, and the *E. coli* R-loop maturation helicase DinG [14], all of which were found to have similar DNA-bound potentials (~80 mV versus NHE) as measured on DNA-modified gold electrodes [6, 7]. The similar DNA-bound midpoint potentials and picosecond kinetics of DNA CT together suggested that DNA CT could provide a means for these enzymes to localize efficiently to the vicinity of their target lesions [15]. Indeed, experiments carried out both *in vitro* and *in vivo* have led to the development of a model for DNA repair in which two $[4\text{Fe}_4\text{S}]$ cluster proteins use DNA CT to communicate with each other over long molecular distances via electron transfer self-exchange reactions [7, 15]. As evidenced through the potential shift, DNA binding activates the proteins toward oxidation to the $[4\text{Fe}_4\text{S}]^{3+}$ state [8]. When the DNA intervening between the two proteins is undamaged, the self-exchange reaction can proceed efficiently, with the result that one of the DNA-bound proteins is reduced and its affinity for DNA lowered. This protein is then free to diffuse to another region of the genome. However, in the case of an intervening mismatch or lesion that impairs CT by disrupting π -stacking, this self-exchange reaction is inhibited. Both proteins then remain bound to the DNA in the vicinity of the lesion, significantly reducing the range over which the slower processes of diffusion must occur and facilitating repair of a relatively large genome on a biologically relevant time scale [15].

While DNA binding is clearly of critical importance to the redox activity of these enzymes, it is not clear that it represents the only way to modulate the potential. It was recently reported that carboxylic acid monolayers had a similar activating effect as DNA, although, in contrast with the above model, they suggested the relevant couple as the $[4\text{Fe}4\text{S}]^{2+/+}$ rather than the $[4\text{Fe}4\text{S}]^{3+/2+}$ couple [16]. With respect to the latter point, the high potential of the reversible DNA-bound signal on both gold and HOPG, EPR spectroscopy of oxidized DNA bound EndoIII and MutY, and the observation of both couples in the expected potential regimes on HOPG support the original $[4\text{Fe}4\text{S}]^{3+/2+}$ assignment [6, 8, 15]. Furthermore, this assignment is in agreement with the known potential ranges accessed by the $[4\text{Fe}4\text{S}]^{3+/2+}$ couple of HiPIPs [17]. Regardless of redox couple assignment, the possibility of activation by other molecules remains an interesting point deserving further investigation.

In addition to other molecules, charged amino acid residues near the cluster might also be expected to affect the potential. This was explored in a recent study in which several EndoIII mutants, E200K, Y205H, and K208E, were prepared and extensively characterized on DNA-modified gold electrodes; although these residues are located within 5 Å of the cluster, all of the mutants had indistinguishable DNA-bound midpoint potentials [18]. Overall, these observations suggested that DNA binding was the dominant environmental effect in modulating potential, but the narrow accessible potential window on gold prevented further investigation.

In this work, we used direct electrochemistry on carbon electrodes to address the capacity of DNA and other polyanions to activate $[4\text{Fe}4\text{S}]$ proteins for redox activity and to assess the ability of local electrostatics to shift the potential of EndoIII in the absence of DNA. Because the hydrophobic surface of HOPG is unsuitable for protein adsorption and difficult to prepare [8, 19, 20], we turned to the rougher, more hydrophilic pyrolytic graphite edge (PGE) electrode for these experiments, using the technique of thin film voltammetry to immobilize proteins in a stable layer on the electrode surface [21–23]. To enhance signal sizes, we also included single-walled carbon nanotubes (CNTs) when possible, taking advantage of their high conductivity and the additional three-dimensional surface area they can provide for protein binding [21]. In summary, this platform provided an ideal and reliable way to improve our understanding of the factors important to tuning the potential of DNA processing enzymes containing $[4\text{Fe}4\text{S}]$ clusters.

3.2 Materials and Methods

EndoIII Overexpression and Purification

WT *E. coli* EndoIII was overexpressed in BL21star-(DE3)pLysS cells containing a pET11-ubiquitin-His6-nth construct and purified as detailed previously [18], with the exception that the final buffer contained 10% rather than 20% glycerol (20 mM sodium phosphate, pH 7.5, 0.5 mM EDTA, 150 mM NaCl, 10% glycerol). For electrochemical experiments, glycerol was removed from the protein solution using a HiPrep 26/10 desalting column (GE Healthcare) equilibrated with a buffer consisting of 20 mM sodium phosphate, pH 7.5, 0.5 mM EDTA, 150 mM NaCl. Following buffer exchange, the protein was concentrated in two steps. First, 10,000 molecular weight cutoff (MWCO) Amicon Ultra 15 mL centrifugation filter units (Millipore) were used to concentrate each protein solution to a total volume of 1 mL or less. Samples were then transferred to 10,000 MWCO Amicon Ultra 0.5 mL centrifugation filter units (Millipore) and concentrated until the initially yellow protein solutions were very dark in color (approximately 300 μ L final volume from 6 L of bacterial culture). Protein purity was confirmed by SDS-PAGE. Immediately following the concentration of the sample, the [4Fe4S] cluster loading ratio was calculated by dividing the total [4Fe4S] cluster concentration as determined from the UV-visible absorbance spectrum using $\epsilon_{410} = 17,000 \text{ M}^{-1} \text{ cm}^{-1}$ by the total protein concentration as measured in a Bradford assay; typical cluster loading ratios for WT EndoIII were 70-75%.

MutY Overexpression and Purification

MBP (Maltose Binding Protein)-MutY fusion protein was expressed and purified using a slightly modified version of a previously reported protocol [24, 25]. Modifications to the protocol included changes in “buffer A” to a resuspension buffer (20 mM sodium phosphate, pH 7.5, 200 mM NaCl, 1 mM EDTA, 1 mM DTT, 1 mM PMSF, and 10% glycerol) and use of an amylose column to eliminate the necessity of a streptomycin sulfate and ammonium sulfate precipitation. During the amylose preparation, the sample was washed with amylose wash buffer (20 mM sodium phosphate, pH 7.5, 200 mM NaCl, 1 mM EDTA pH 8) and eluted in amylose elutant buffer (20 mM sodium phosphate, pH 7.5, 200 mM NaCl, 1 mM EDTA pH 8, 10 mM maltose). The resultant fractions were concentrated using an ultrafiltration cell with a 10,000 MWCO filter with stirring at 4 °C. Protein was then diluted 10-fold in heparin buffer A (20 mM sodium phosphate, pH 7.5, 1 mM EDTA, 5% glycerol in water), applied to a Pharmacia Hi-trap heparin column on an AKTApurifier FPLC

system, and eluted using a 10% linear gradient in heparin buffer A to 100% heparin buffer B (20 mM sodium phosphate, pH 7.5, 1 mM EDTA, 5% glycerol, and 1 M NaCl in water). MBP-MutY eluted at 450 mM NaCl (45% heparin buffer B). Those fractions were combined, concentrated to 50 mM and exchanged into a final buffer composed of 20mM sodium phosphate, pH 7.5, 1mM NaCl to remove glycerol. The purity of protein samples was confirmed via 12% SDS page stained with SYPRO orange. The [4Fe4S] cluster loading was determined using the UV-visible absorbance at 410 nm ($\epsilon_{410} = 17,000 \text{ M}^{-1} \text{ cm}^{-1}$) and at 280 nm ($\epsilon_{280} = 143,240 \text{ M}^{-1} \text{ cm}^{-1}$); samples were typically 65–75% loaded.

DNA Preparation

DNA strands for EndoIII experiments were purchased from Integrated DNA Technologies, with sequences as follows:

- **20-mer:** 5'-GTG AGC TAA CGT GTC AGT AC-3'
- **Complement:** 5'-GTA CTG ACA CGT TAG CTC AC-3'

Single-stranded DNA oligomers (5 μmol) were resuspended in Milli-Q water and purified by ethanol precipitation. Briefly, 1 mL of cold 200 proof ethanol and 50 μL of 3 M NaCl were added to 100 μL single-stranded DNA in water and vortexed; DNA solutions were then frozen in liquid nitrogen for rapid precipitation and spun at 16,000 RCF (25 min) to form a pellet which was then redissolved in EndoIII storage buffer (20 mM sodium phosphate, pH 7.5, 0.5 mM EDTA, 150 mM NaCl). Single-stranded DNA was quantified by UV-vis using ϵ_{260} values calculated using the Integrated DNA Technologies oligo analyzer tool; these were $197,800 \text{ M}^{-1} \text{ cm}^{-1}$ for the 20-mer strand and $190,200 \text{ M}^{-1} \text{ cm}^{-1}$ for its complement. Equimolar amounts of each strand were then annealed by incubation at 90C for 5 min followed by slow cooling to ambient temperature.

For MutY experiments, DNA substrates containing oxoG (8-oxo-guanine) or FA (2'-fluoro-deoxyadenosine) were synthesized at the University of Utah DNA and Peptide Synthesis Core Facility, and unmodified strands were ordered from Integrated DNA Technologies. The following DNA duplexes were used:

- **30-mer:** 5'-CGA TCA TGG AGC CAC XAG CTC CCG TTA CAG-3'
- **Complement:** 5'-GCT AGT ACC TCG GTG YTC GAG GGC AAT GTC-3'

- **X** = G or oxoG and **Y** = C, FA, or A

Oligonucleotides containing the central oxoG or FA were deprotected and cleaved from the column by incubation in NH_4OH ; 2-mercaptoethanol was added into oxoG samples to prevent oxidation. The cleaved DNA substrates were dissolved in H_2O , filtered with a $0.2 \mu\text{m}$ filter, and HPLC purified using a Beckman Gold Nouveau system with a Waters AP1DEAE 8HR column; a 10–100% gradient of 90:10 H_2O /acetonitrile with 2 M NH_4Ac was used in purification. Isolated fractions were dried down and desalted using SEP-PAK cartridges, and DNA integrity was confirmed using MALDI-MS. All DNA substrates were stored dried in the -20C freezer prior to annealing.

Electrochemistry

All electrochemical experiments were performed on an edge-plane pyrolytic graphite electrode (Pine Research Instrumentation) with a geometric surface area of 0.196 cm^2 . To generate a rough surface suitable for protein binding, the electrode was abraded with 400 grit sandpaper and cleaned by sonication for 1 min each in ethanol and water. After sonication, the absence of electroactive impurities was verified by scanning in EndoIII storage buffer (20 mM sodium phosphate, 0.5 mM EDTA, 150 mM NaCl, pH 7.5) or MutY storage buffer (20 mM sodium phosphate, 1 mM EDTA, 150 mM NaCl, pH 7.6) as appropriate. Single-walled carbon nanotubes (CNTs) were found to enhance greatly the signal size of adsorbed protein, so they were included in the formation of all thin films unless otherwise noted. Protein thin films were formed from several (typically 3–6) alternate layers of $10 \mu\text{L}$ single-walled carbon nanotubes (CNT) in water (0.25 mg/mL) and $10 \mu\text{L}$ EndoIII (150 μM in storage buffer) or MutY (50 μM) in a 1:1 mix with aqueous CNTs. Each layer was gently dried under an argon gun, and the process was repeated until the surface was coated by a viscous film, which was then secured with 5% Nafion in water (diluted from 10% in water as purchased) to prevent dispersal [21]. For experiments including DNA, CNTs generally hindered electrochemical signals, so these films were formed in their absence. Poly-L-glutamate (MW 50–100 kDa) was used to assess the effects of a negatively charged nonsubstrate on potential. Although Nafion also carries a negative charge at the pH values used, it was applied only to the top of a multilayer film to form a binding layer, minimizing interactions with the electroactive protein; in contrast, poly-L-glutamate and DNA were incorporated directly into the thin film with protein to maximize any possible interactions.

After thin film formation, 50 μL of EndoIII or MutY storage buffer was pipetted on top of the film and a Ag/AgCl reference in 3 M NaCl and Pt auxiliary electrode were submerged in the resulting droplet. Reduction potential, current, and charge measurements were then taken by cyclic voltammetry (CV), square wave voltammetry (SQWV), and differential pulse voltammetry (DPV); all experiments were conducted at ambient temperature (20C). Electroactive area was determined by plotting the scan rate dependence of the CV current generated by 1 mM $[\text{Ru}(\text{NH}_3)_6]\text{Cl}_3$ in storage buffer and applying the Randles–Sevcik equation [26]:

$$I_p = \left[0.4463(F^3/RT)^{1/2} \right] (n^{3/2})(A)(D^{1/2})(C^\circ)v^{1/2} \quad (3.1)$$

I_p is the peak current in amperes, F is Faraday's constant ($96485 \text{ C} \cdot \text{mol}^{-1}$), R is the universal gas constant ($8.314 \text{ J} \cdot (\text{mol} \cdot \text{K})^{-1}$), T is the temperature in K , n is the number of electrons transferred per CV peak, A is the electrode area in cm^2 , D is the diffusion coefficient in $\text{cm}^2 \cdot \text{s}^{-1}$ (9.0×10^{-6} for $[\text{Ru}(\text{NH}_3)_6]_{3+}$) [27], C° is the bulk protein concentration in $\text{mol} \cdot \text{cm}^{-3}$, and v is the scan rate in $\text{V} \cdot \text{s}^{-1}$. Potentials were converted to NHE by adding 0.212V to the value measured by Ag/AgCl, using the value of 0.209mV at 25°C given by the supplier, BASi, and applying a temperature correction [28]. To prevent leakage of NaCl into the buffer and subsequent wandering of the reference potential, the glass frit of the electrode was immersed in a gel loading pipet tip containing 3 M NaCl with 4% dissolved agarose, and dried in this mix overnight. CNTs, 10% aqueous Nafion, poly-L-glutamate, and $[\text{Ru}(\text{NH}_3)_6]\text{Cl}_3$ were purchased from Sigma-Aldrich, while the Ag/AgCl reference electrode in 3 M NaCl was purchased from BASi.

3.3 Results

Direct Electrochemistry of WT EndoIII and MutY

To examine variations in EndoIII potentials with various substitutions or binding partners, EndoIII thin films anchored to the surface by Nafion were prepared on a PGE electrode. In the absence of DNA, a quasi-reversible signal was observed by CV (Figure 3.1). The signal under these conditions was relatively small ($3 \pm 1 \mu\text{C}$ reductive peak, $-4 \pm 1 \mu\text{C}$ oxidative peak), and the reductive peak partially overlapped the much larger wave of oxygen reduction, making it more challenging to quantify. By adding 0.25 mg/mL CNTs to form a protein/CNT/Nafion thin film, the peak areas increased by an order of magnitude to reach 16 ± 3 and $-18 \pm 5 \mu\text{C}$ reductive and oxidative peaks, respectively, while the peak potentials remained

unaltered from those without the CNTs at 74 ± 20 and 162 ± 18 mV (all potentials vs NHE).

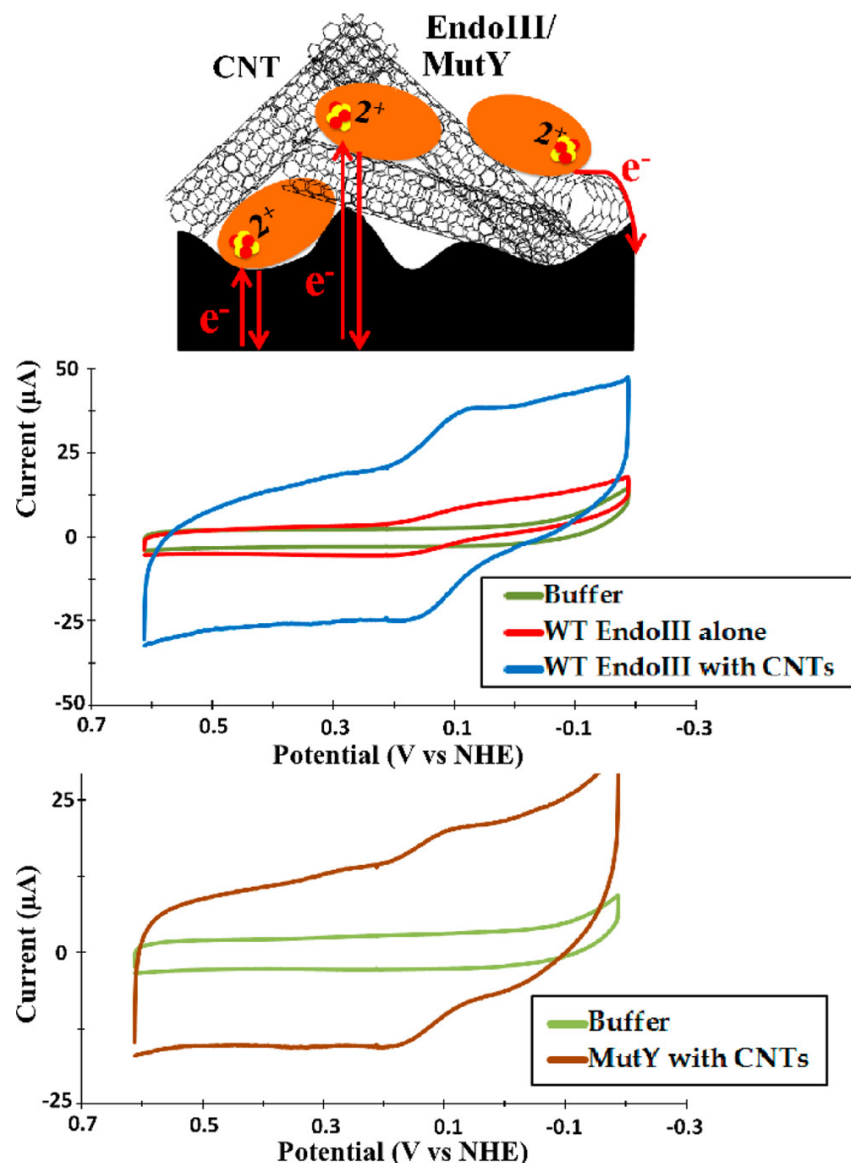


Figure 3.1: Representative CVs from EndoIII and MutY thin films on a PGE electrode. A thin film containing only $75 \mu\text{M}$ EndoIII capped with Nafion gave a quasi-reversible signal with reductive and oxidative peaks centered, respectively, at 74 ± 11 and 162 ± 20 mV versus NHE (center; red trace). Notably, the addition of CNTs substantially amplified the signal, simplifying quantification (center; blue trace). Similarly, $25 \mu\text{M}$ MutY in the presence of CNTs yielded a signal with reductive and oxidative peaks at 100 ± 9.0 and 162 ± 3.0 mV versus NHE (bottom). CV scans were taken at a scan rate of 100 mV/s.

The addition of EndoIII and CNTs was associated with a large increase in the capacitance; much of this increase was due to CNTs, as seen in CNT/Nafion

thin films, but the protein itself certainly contributed (Figure A.8). Notably, the high conductivity of CNTs amplifies redox events at the surface; a CNT/Nafion film shows reversible peaks around 200 mV vs NHE and -80 mV vs NHE, both of which show no splitting and are likely attributable to the reversible reduction of surface oxides on the edge plane and even on the CNTs themselves (Figure A.8) [29–31]. Indeed, the 200 mV peaks were invariably present, although smaller, in buffer alone and the -80 mV peaks varied in size based upon the freshness of the CNT suspension applied, consistent with this assertion. The presence of protein on the surface markedly suppressed both of these peaks, and the EndoIII signal differed from the background both by its potential, which was essentially identical to that measured in the absence of CNTs, and in the occurrence of peak splitting; the latter suggested a slower process, in agreement with reports of other proteins adsorbed on carbon [21].

WT MutY thin films were prepared just as with EndoIII, although the stock concentrations were somewhat lower ($\sim 50 \mu\text{M}$ for MutY compared to $\sim 150 \mu\text{M}$ for EndoIII). MutY displayed a quasi-reversible signal similar to EndoIII on CNT/Nafion thin films, with CV peak potentials centered at $100 \pm 9 \text{ mV}$ for the reductive peak and $162 \pm 3 \text{ mV}$ for the oxidative peak (Figure 3.1). Notably, the potentials were within error of the values obtained for EndoIII. The respective peak areas were 2.3 ± 0.3 and $-3.4 \pm 0.1 \mu\text{C}$, about an order of magnitude smaller than EndoIII and indicative of lower surface coverage.

For both EndoIII and MutY, the current exhibited a linear dependence on the scan rate (Figure A.9), confirming that the protein was adsorbed to the electrode surface rather than diffusing in from solution; this relationship was present whether or not CNTs were included. Surface coverage was initially determined simply by converting the total CV peak charge at a scan rate of 100 mV/s into pmol using Faraday's constant and dividing by the geometric surface area of the electrode. Because the PGE surface is uneven, the geometric surface area can underestimate the electroactive area by a factor as large as 10^4 [32]. Indeed, using the geometric area of the electrode (0.196 cm^2) gave a surface coverage of $550 \pm 300 \text{ pmol/cm}^2$ for $75 \mu\text{M}$ EndoIII stock, over 10 times larger than reported for ferredoxin thin films on PGE (40 pmol/cm^2) [32] and over 100 times larger than CNT/Nafion/protein thin films on glassy carbon ($2\text{--}6 \text{ pmol/cm}^2$) [21].

By taking the scan rate dependence of the current for $[\text{Ru}(\text{NH}_3)_6]^{3+}$ in EndoIII storage buffer and applying the Randles–Sevcik equation (Equation 3.1), the

electroactive surface area was determined to be 1.0 cm^2 , about 5 times larger than the simple geometric area. When this correction was applied to a thin film formed from $75 \text{ }\mu\text{M}$ EndoIII stock, a value of $108 \pm 60 \text{ pmol/cm}^2$ was obtained, which is still high but much closer to previously published results on PGE [32]. Applying the same correction to films formed from $25 \text{ }\mu\text{M}$ MutY stock gave a coverage of $29 \pm 6 \text{ pmol/cm}^2$, around 25% of that measured for $75 \text{ }\mu\text{M}$ EndoIII. To facilitate a more direct comparison, surface coverage on thin films formed with $25 \text{ }\mu\text{M}$ EndoIII was measured to be $51 \pm 8 \text{ pmol/cm}^2$, indicating that MutY adsorption was absolutely less extensive than EndoIII. This result is not surprising, given that unmodified MutY is 39 kDa while EndoIII is only 24 kDa; the 42 kDa N-terminal MBP tag on MutY would only enhance this issue.

Adsorption of proteins to the electrode surface made it possible to estimate electron transfer rate (k_{ET}) and transfer coefficient (α) values using the Laviron method for diffusionless systems (Figure A.9) [33], where α is a measure of transition state symmetry, taking on values between 0 and 1. The MutY signal was too small to measure the currents at high scan rates, but this analysis could be carried out for EndoIII. In the case of EndoIII, we obtained a k_{ET} value of $3 \pm 0.6 \text{ s}^{-1}$ and α values of 0.4 and 0.6 for the reductive and oxidative peaks, respectively. Assuming that electron transfer is the only reaction taking place on the electrode, the values of α imply a quasi-reversible system. Importantly, electron transfer rates are similar to those reported for other redox-active enzymes/proteins adsorbed to carbon electrodes in the presence of CNTs and Nafion [21].

Electrochemistry of WT EndoIII and MutY in the Presence of DNA

Having found thin films on PGE to facilitate the direct electrochemistry of free [4Fe4S] proteins, we proceeded to see if the DNA-directed potential shift observed on HOPG could be replicated. With this aim in mind, a solution containing EndoIII and 20-mer duplex DNA in a 1:1 ratio in storage buffer was prepared, incubated on ice for 30 min, and dried to form a thin film on the electrode surface. Inclusion of CNTs in the film resulted in a noisy, widely split ($>100 \text{ mV}$) signal that had the same potential as DNA-free protein, indicating that the protein was not DNA-bound. Thus, CNTs were excluded from subsequent experiments with DNA present. Under these conditions, EndoIII showed a very small signal by CV that was much more readily visualized and quantified using square wave voltammetry (SQWV; Figure 3.2, Table 3.1). The potential as measured by SQWV was $64 \pm 8 \text{ mV}$, representing a negative shift of $\sim 60 \text{ mV}$ from the DNA-free value of $130 \pm 8 \text{ mV}$. This result is

Enzyme	ESQWV (mV), No DNA	ESQWV (mV), + DNA
WT EndoIII	130 ± 8	64 ± 8 ^b
WT EndoIII poly-L- glutamate	110 ± 8	-
WT EndoIII E200K	130 ± 7	-
WT EndoIII Y205H	125 ± 11	-
WT EndoIII K208E	141 ± 12	-
WT MutY	> 130 ^c	85 ± 3 ^b 80 ± 6 ^{b,d}

Table 3.1: Potentials (versus NHE) of SQWV Reductive Sweeps for WT and Mutant EndoIII and WT MutY in the Presence and Absence of DNA^a. (a) When used, CNTs were added from a 0.25 mg/mL stock, and all experiments used protein storage buffer as the supporting electrolyte (20 mM sodium phosphate, 0.5 mM EDTA, 150 mM NaCl, pH 7.5 for EndoIII and 20 mM sodium phosphate, 1 mM EDTA, 150 mM NaCl, pH 7.6 for MutY). Each value is the average of three or more separate experiments, and the error is the standard deviation of the mean. (b) No CNTs present. (c) The MutY SQWV peaks (Figure 3.2) were too small and noisy to measure the potential with confidence. (d) OG:FA MutY substrate trap DNA.

in overall agreement with earlier results supporting the stabilization of the oxidized [4Fe4S]³⁺ form upon DNA binding, but the shift seen here is markedly smaller [8]. This difference can likely be attributed to less than 100% of the protein being DNA bound; free protein likely contributed to the observed peak, leading to an underestimate of the shift. This heterogeneity could be further complicated by the expected random orientation of DNA and protein at the electrode. Indeed, this is a fundamental difference between the HOPG and PGE setups: the signal on HOPG was DNA-mediated, while that on PGE was not.

Electrochemistry of MutY thin films prepared in the presence and absence of DNA (a 30-mer duplex, in this case) gave similar results to EndoIII. In the absence

of DNA and CNTs, the SQWV peak was too small to measure the potential with confidence, but it was in the same region as EndoIII (~ 130 mV vs NHE; Figure 3.2); when DNA was present, the potential shifted to 85 ± 3 mV vs NHE (Figure 3.2, Table 3.1). In an effort to obtain larger signal sizes by increasing the proportion of DNA-bound protein on the surface, the experiment was repeated with DNA containing an FA:oxoG substrate trap, which mimics the A:oxoG target of MutY but inhibits N-glycosidic bond cleavage due to the electron withdrawing effect of the fluorine at the sugar 2' position [34]. No significant differences were observed, although the potential of 80 ± 6 mV indicated a similar DNA-bound signal, suggesting that any increase in DNA binding affinity afforded by the substrate trap was not sufficient to overcome the combined effects of DNA-free proteins on the surface and surface passivation by the DNA itself. In considering these results, it is important to note that, while a shift could be observed for both proteins, surface passivation by non-tethered DNA blocked a portion of the available electroactive sites and made the signals small and noisy. Taken together, these results demonstrate the limitations of the PGE surface, but importantly, they confirm that large potential shifts can be observed on the PGE electrode even under suboptimal conditions.

Direct Electrochemistry of WT EndoIII in the Presence of Poly-L-Glutamate

We next sought to determine if DNA is unique in its ability to shift the potential of the [4Fe4S] cluster by forming thin films with poly-L-glutamate (MW 50-100 kDa). Due to the small size of MutY signals, EndoIII was used for this purpose. Like DNA, poly-L-glutamate is polyanionic, but it is not a specific target for EndoIII binding. In these experiments, poly-L-glutamate was preincubated with EndoIII in a 1:1 ratio and added to thin films just as with DNA. Unlike with DNA, the measured potentials and peak shapes were indistinguishable whether or not CNTs were included. Interestingly, the presence of poly-L-glutamate did not result in a significant potential shift by CV, with the reductive and oxidative peaks centered at 81 ± 1 and 143 ± 1 mV, respectively (Figure 3.3). At 110 ± 9 mV, the SQWV potential is, accounting for error, about 10 mV lower than that of free EndoIII but is still substantially more positive than the DNA-bound potential (Table 3.1). The CV values are within error of that for free WT EndoIII (Figure 3.3, Table 3.1), and given that EndoIII does not specifically bind to poly-L-glutamate, this result should not be too surprising. It is likely that the [4Fe4S] cluster is not exposed to the negative charges of unbound poly-L-glutamate to the extent that it would be when the protein is tightly bound to DNA, so no significant shift can be observed. This is also in line

with the insusceptibility of free EndoIII to oxidation or reduction originally noted by Cunningham [2]. Overall, these results indicate that the potential of the EndoIII [4Fe4S] cluster can be appreciably altered only when the protein binds directly to a polyanion, such that the cluster experiences the full effect of the negative charges. Thus, DNA appears uniquely able to affect the potential of the cluster both by its charges and by its function as a binding substrate for these types of [4Fe4S] proteins.

Direct Electrochemistry of EndoIII Mutants

Since EndoIII was observed to undergo a significant potential shift upon DNA binding but not in the presence of the nonsubstrate poly-L-glutamate, we reasonably assumed that only charges in the immediate vicinity of the cluster could shift the potential. Following this line of reasoning, we sought to determine if altering the charge on amino acid residues near the cluster might have a similarly large effect on the potential. Mutation of nearby residues to give a net positive or negative charge was of further interest because it could, in principle, shift the cluster potential in both positive and negative directions, unlike the unidirectional shift associated with DNA binding.

In order to investigate these possibilities, the following EndoIII point mutants were prepared: E200K, Y205H, and K208E [18]. All of these residues are ~ 5 Å from the cluster, and these mutations span nearly the full range of possible single-charge alterations, going from a single negatively charged residue to a positively charged one (E200K), a neutral residue to a positive residue (Y205H), and a positive residue to a negative one (K208E). Positively charged mutants would be expected to be more repulsive to the [4Fe4S]³⁺ state, favoring reduction, while negatively charged mutants would be more attractive, stabilizing the oxidized form of the protein. While shifts might be expected, the precise extent cannot be readily predicted; a study on outer-sphere effects in HiPIP [4Fe4S] protein resulted in shifts as large as 150 mV, while surface mutations in certain ferredoxins led to no changes in potential [35, 36].

Surprisingly, all of the mutants exhibited DNA-free potentials on PGE thin films within error of WT (Figure 3.3, Table 3.1); this was apparent by CV, SQWV, and DPV. However, the standard deviation was relatively high, with the largest value (for WT) around 20 mV. Since conclusions are limited by the largest error among the species investigated, these data are consistent with two possibilities: either there is no change between WT and any of the mutants, or a small shift on the order of 10

mV is present. In either case, it is clear that the effect of changing a single charge, even one in very close proximity to the cluster, is much less dramatic than that of DNA binding.

To confirm the accuracy of potential measurements, thin films formed with 2 mM $[\text{Ru}(\text{NH}_3)_6]^{3+}$ with and without EndoIII were also examined (Figure A.10). The $[\text{Ru}(\text{NH}_3)_6]^{3+}$ midpoint potential was consistently ~ 10 mV vs NHE in the presence and absence of CNTs and Nafion, as well as in the presence and absence of EndoIII. Just as with EndoIII, CNTs did markedly sharpen the peaks and facilitate larger signals, independently confirming their effect on species in a thin film. Overall, these controls verified that the measured potentials were not affected by CNTs or other thin film components, indicating that the observed lack of variation between mutants was due to properties of the proteins themselves. Overall, direct electrochemistry of these EndoIII mutants confirms that DNA binding is a dominating effect relative to single charge reversals in the amino acid sequence [18].

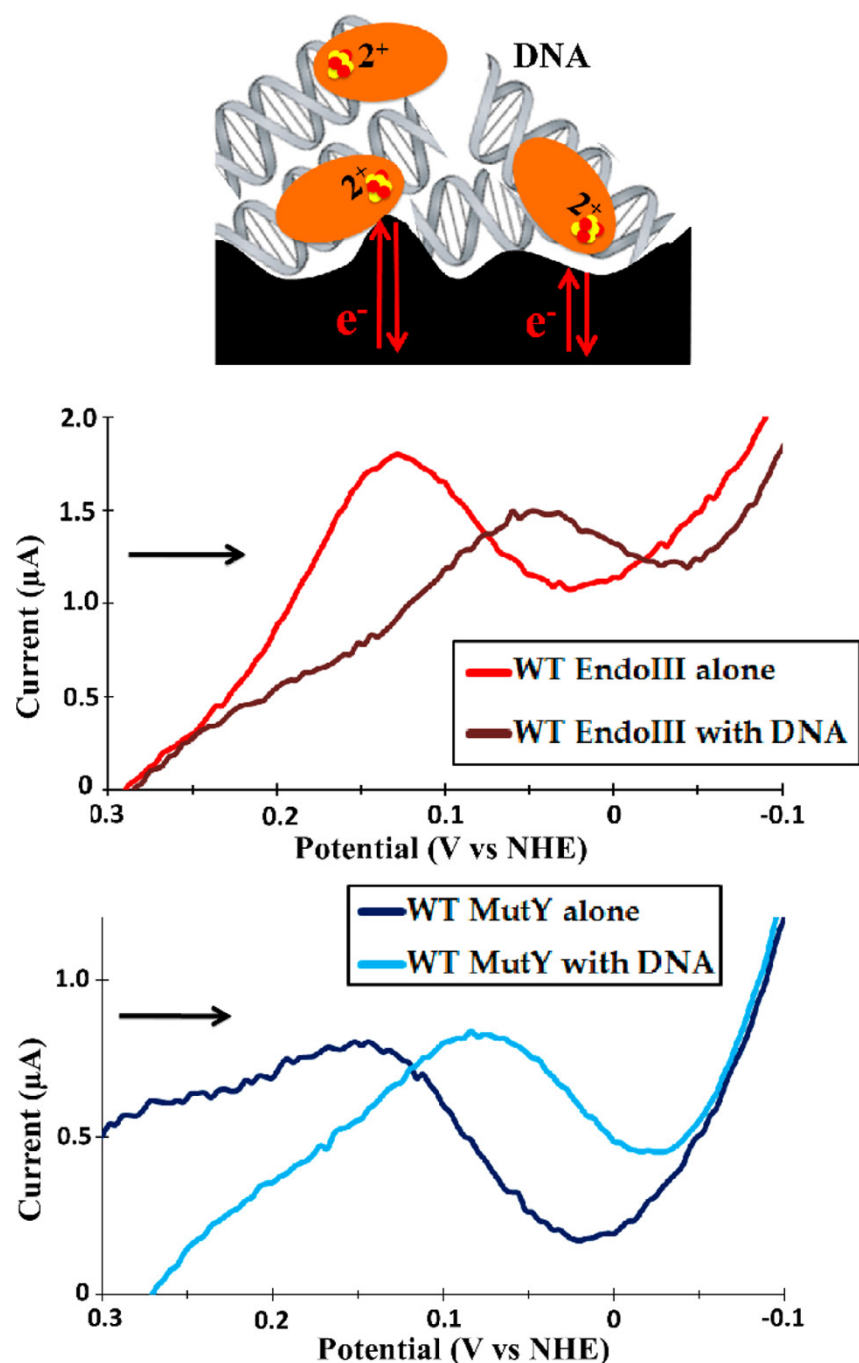


Figure 3.2: EndoIII and MutY thin film voltammetry on a PGE electrode in the presence of DNA. By SQWV, the presence of DNA resulted in a -65 mV shift in the potential of 75 μM EndoIII (center), with a similar result for 25 μM MutY (bottom). Signals were very small due to surface passivation, but they were still readily apparent by SQWV. Unfortunately, CNTs led to inconsistent and unstable signals, likely interfering with DNA binding, so they could not be used to enhance the signals. Thin films were formed from several layers of a premixed 1:1 protein/DNA solution, and were capped with Nafion. SQWV scans were taken at a frequency of 15 Hz with 0.025 V amplitude, and scans were from positive to negative potentials (indicated by the arrow).

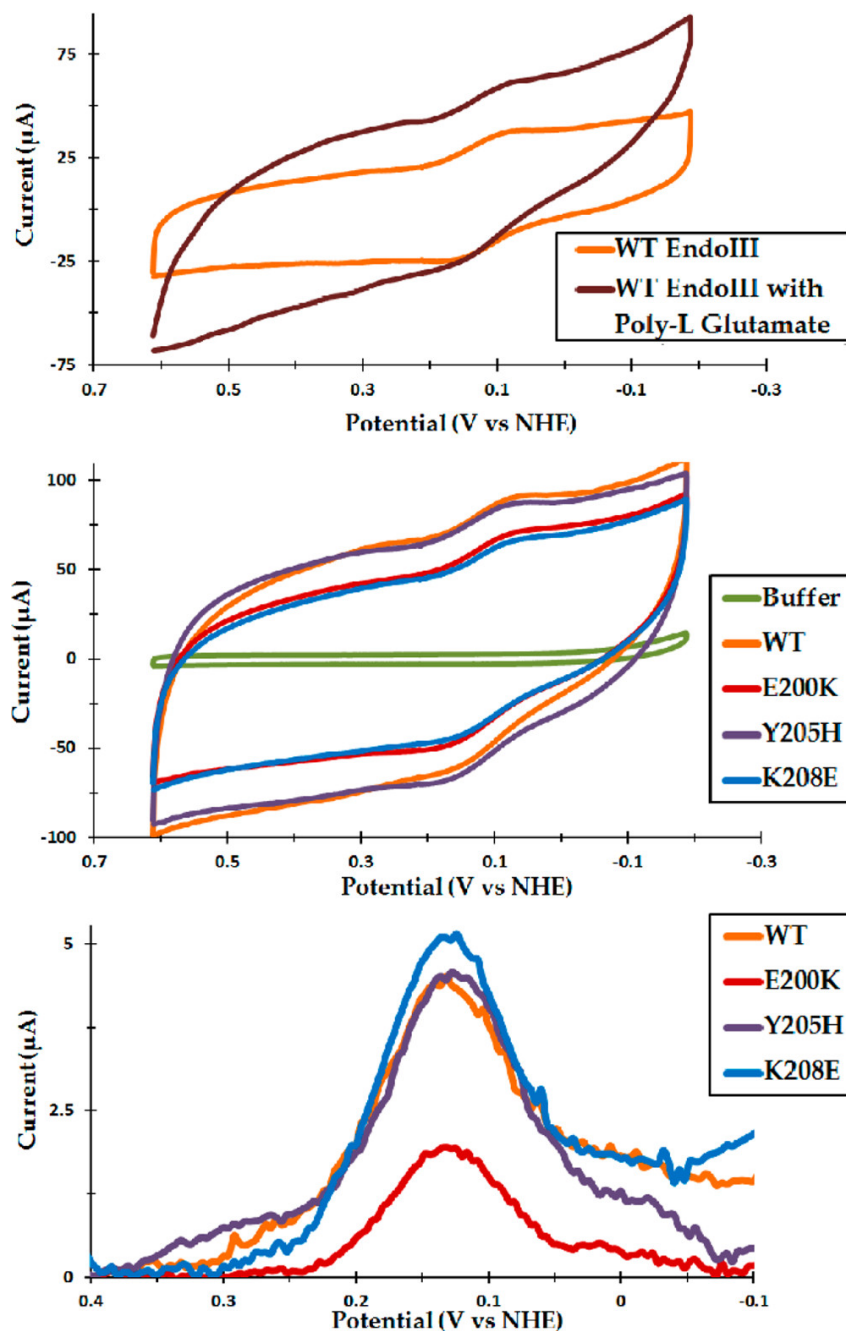


Figure 3.3: Thin film voltammetry of WT EndoIII with poly-l-glutamate and comparison of WT with the mutants E200K, Y205H, and K208E. Unlike DNA, poly-L-glutamate caused no significant potential shift even at 6 mM glutamate (top). 75 μ M WT and mutant EndoIII in protein/CNT/Nafion thin films had nearly identical potentials, with CV peaks centered around 125 mV versus NHE (center); the similarity is even more apparent by DPV (bottom). Small shifts within the measurement error (10–15 mV) are still possible but pale in comparison to the effect of DNA. All CVs shown were taken at 100 mV/s, while DPVs were taken at an amplitude of 0.05 V with a 0.5 s pulse period. Poly-L-glutamate was preincubated with 75 μ M EndoIII both with and without CNTs; due to the larger signals, the CVs shown are from films including CNTs.

3.4 Discussion

In this study, we have used thin film voltammetry on a PGE electrode to measure the potentials of EndoIII and MutY in the presence and absence of DNA, and, in the case of EndoIII, in the presence of poly-l-glutamate and with point mutations altering the charged environment near the cluster. Table 3.1 summarizes all of the results. Notably, the potential shift observed upon DNA binding was smaller than previously reported [8], with the SQWV potentials of DNA-free EndoIII going from 250 ± 30 mV on HOPG to 130 ± 8 mV on PGE. This difference was certainly in large part the result of less than 100% DNA binding on PGE, but the distinct electrode environments on PGE and HOPG may also have played a role [8, 19, 20]. Indeed, the presence of negatively charged surface oxides on PGE, but not HOPG, would be expected to lower the potential of adsorbed proteins to some extent [29]. Even with a lower DNA-free potential, DNA-bound potentials still dropped by 65 mV on PGE, which supports the assertion that DNA binding has a prominent, although not necessarily additive, effect which cannot be duplicated by nonsubstrate polyanionic molecules such as poly-L-glutamate.

The absence of a significant potential shift in the presence of poly-l-glutamate does at first appear to be in conflict with the results of the Todorovic group, wherein the redox activation of EndoIII was reported on a mercaptoundecanoic acid monolayer assembled on a gold electrode in the absence of DNA [16]. However, this effect was attributed to tight binding to the carboxylic acid film; in contrast, the solvated poly-L-glutamate used here would present a very different environment than a thin film of small molecules, and it is unlikely that EndoIII was readily able to bind this nonsubstrate polymer. While it is reasonable that multiple negative charges could shift the potential, they can only do so if EndoIII is able to bind with some specificity.

The results obtained here for DNA demonstrate that large potential shifts are observable on PGE even under conditions where full DNA binding is unlikely. In contrast to the conditions required to study DNA binding, the DNA-free EndoIII mutants were studied under conditions that generated very large and readily quantifiable signals; thus, the lack of any apparent change in the potential among these mutants indicates that individual charge alterations near the cluster do not have a significant effect. However, the error in these experiments was relatively high, leaving two interpretations open. First, there may genuinely be no shift. In this case, the conclusion would be that a single charge alteration is insufficient by itself to dis-

rupt the local environment, even for residues ~ 5 Å from the cluster. Alternatively, because the measurement error was around 20 mV for WT, shifts on the order of 10 mV may have been present but undetectable. Such small shifts would still pale in comparison to those associated with DNA binding, which are larger as independently measured on a PGE electrode (-60 mV for the EndoIII 2+/3+ couple) and on a HOPG electrode (-200 mV) [8]. Assuming that the charge mutants of EndoIII do have altered potentials and that the shift is at the upper limit of our error (~ 10 mV), the effect of DNA binding is at minimum 6 times greater than the effect of a single charge alteration. In either case, it should be noted that, despite the small signals and adverse conditions resulting from DNA in the film, a substantial shift in potential upon DNA binding was still detectable on PGE, while no obvious shift in potential relative to WT was observed for any of the mutants, even though their potentials were determined from very large DNA-free signals under ideal circumstances.

A similar result obtained with the same mutants on DNA-modified gold electrodes supports the observed lack of potential shifts. In those experiments, the similarity in potential was attributed to the presence of DNA being a dominant effect, with only an increase in current correlated with protein folding stability occurring for K208E and Y205H [18]. The smaller accessible window and poor to nonexistent DNA-free signal on gold electrodes prevented the experiments described here from being carried out, but taken along with our results, it appears that the mutants have similar potentials to WT both on and off of DNA.

In summary, these results reveal that, under the same experimental conditions, DNA binding is the dominant factor in tuning the redox potential of the [4Fe4S] cluster. This is supported by the similarity of the DNA-bound midpoint potentials of various repair enzymes [6], which all fall within a range of 60-85 mV vs NHE. In the context of DNA repair, we have previously proposed a model in which these proteins use single-electron transfers to signal to each other across the genome in the search for damage [15]. In order for this model to work, the electron transfers must be reversible, necessitating that the proteins involved have approximately equal DNA-bound midpoint potentials. If this were not the case, proteins of lower reduction potential would remain bound at the expense of those of higher potential, and the search process would only be able to proceed by diffusion processes that are too slow to fully account for the time scale of DNA repair [15]. This model depends on the large effect of DNA binding to bring potentials into a relevant regime, and our results verify that differences in the protein environment are unlikely to shift

the potential sufficiently to affect the reversibility of interprotein signaling on DNA. Overall, the similar DNA-bound potentials among diverse proteins not only facilitate the DNA damage search but could also make long-range communication between diverse pathways possible.

References

- (1) Kim, Y.-J.; Wilson, D. M. *Curr Mol Pharmacol* **2012**, *5*, 3–13.
- (2) Cunningham, R. P.; Asahara, H.; Bank, J. F.; Scholes, C. P.; Salerno, J. C.; Surerus, K.; Munck, E.; McCracken, J.; Peisach, J.; Emptage, M. H. *Biochemistry* **1989**, *28*, 4450–4455.
- (3) Porello, S. L.; Cannon, M. J.; David, S. S. *Biochemistry* **1998**, *37*, 6465–6475.
- (4) David, S. S.; O’Shea, V. L.; Kundu, S. Base-excision repair of oxidative DNA damage., *Nature* <https://www.nature.com/articles/nature05978> (accessed 07/06/2018).
- (5) Woods, R. D.; O’Shea, V. L.; Chu, A.; Cao, S.; Richards, J. L.; Horvath, M. P.; David, S. S. *Nucleic Acids Res* **2016**, *44*, 801–810.
- (6) Boal, A. K.; Yavin, E.; Lukianova, O. A.; O’Shea, V. L.; David, S. S.; Barton, J. K. *Biochemistry* **2005**, *44*, 8397–8407.
- (7) Arnold, A. R.; Grodick, M. A.; Barton, J. K. *Cell Chemical Biology* **2016**, *23*, 183–197.
- (8) Gorodetsky, A. A.; Boal, A. K.; Barton, J. K. *J. Am. Chem. Soc.* **2006**, *128*, 12082–12083.
- (9) Thayer, M. M.; Ahern, H.; Xing, D.; Cunningham, R. P.; Tainer, J. A. *EMBO J* **1995**, *14*, 4108–4120.
- (10) Fromme, J. C.; Verdine, G. L. *The EMBO Journal* **2003**, *22*, 3461–3471.
- (11) Guan, Y.; Manuel, R. C.; Arvai, A. S.; Parikh, S. S.; Mol, C. D.; Miller, J. H.; Lloyd, R. S.; Tainer, J. A. *Nature Structural & Molecular Biology* **1998**, *5*, 1058–1064.
- (12) Fromme, J. C.; Banerjee, A.; Huang, S. J.; Verdine, G. L. *Nature* **2004**, *427*, 652–656.
- (13) Stephens, P. J.; Jollie, D. R.; Warshel, A. *Chem. Rev.* **1996**, *96*, 2491–2514.
- (14) Ren, B.; Duan, X.; Ding, H. *J. Biol. Chem.* **2009**, *284*, 4829–4835.
- (15) Boal, A. K.; Genereux, J. C.; Sontz, P. A.; Gralnick, J. A.; Newman, D. K.; Barton, J. K. *Proc. Natl. Acad. Sci. U.S.A.* **2009**, *106*, 15237–15242.
- (16) Moe, E.; Sezer, M.; Hildebrandt, P.; Todorovic, S. *Chem. Commun.* **2015**, *51*, 3255–3257.
- (17) Dey, A.; Jenney, F. E.; Adams, M. W. W.; Babini, E.; Takahashi, Y.; Fukuyama, K.; Hodgson, K. O.; Hedman, B.; Solomon, E. I. *Science* **2007**, *318*, 1464–1468.
- (18) Pheeny, C. G.; Arnold, A. R.; Grodick, M. A.; Barton, J. K. *J. Am. Chem. Soc.* **2013**, *135*, 11869–11878.

- (19) Banks, C. E.; Compton, R. G. *Analyst* **2006**, *131*, 15–21.
- (20) Armstrong, F. A.; Bond, A. M.; Hill, H. A. O.; Oliver, B. N.; Psalti, I. S. M. *J. Am. Chem. Soc.* **1989**, *111*, 9185–9189.
- (21) Yin, Y.; Lü, Y.; Wu, P.; Cai, C. *Sensors* **2005**, *5*, 220–234.
- (22) Léger, C.; Elliott, S. J.; Hoke, K. R.; Jeuken, L. J. C.; Jones, A. K.; Armstrong, F. A. *Biochemistry* **2003**, *42*, 8653–8662.
- (23) Blanford, C. F.; Armstrong, F. A. *J Solid State Electrochem* **2006**, *10*, 826–832.
- (24) Chmiel, N. H.; Golinelli, M.-P.; Francis, A. W.; David, S. S. *Nucleic Acids Res* **2001**, *29*, 553–564.
- (25) Boon, E. M.; Livingston, A. L.; Chmiel, N. H.; David, S. S.; Barton, J. K. *Proc Natl Acad Sci U S A* **2003**, *100*, 12543–12547.
- (26) Kissinger, P.; Heineman, W. R., *Laboratory Techniques in Electroanalytical Chemistry, Second Edition, Revised and Expanded*, Google-Books-ID: AwuTx14Ro2UC; CRC Press: 1996; 1014 pp.
- (27) Wang, Y.; Limon-Petersen, J. G.; Compton, R. G. *Journal of Electroanalytical Chemistry* **2011**, *652*, 13–17.
- (28) Greeley, R. S.; Smith, W. T.; Stoughton, R. W.; Lietzke, M. H. *J. Phys. Chem.* **1960**, *64*, 652–657.
- (29) McCreery, R. L. *Chem. Rev.* **2008**, *108*, 2646–2687.
- (30) Blurton, K. F. *Electrochimica Acta* **1973**, *18*, 869–875.
- (31) Gooding, J. J. *Electrochimica Acta* **2005**, *50*, 3049–3060.
- (32) Breton, J. L.; Duff, J. L. C.; Butt, J. N.; Armstrong, F. A.; George, S. J.; Pétillot, Y.; Forest, E.; Schäfer, G.; Thomson, A. J. *European Journal of Biochemistry*, *233*, 937–946.
- (33) Laviron, E. *Journal of Electroanalytical Chemistry and Interfacial Electrochemistry* **1979**, *101*, 19–28.
- (34) Lee, S.; Verdine, G. L. *PNAS* **2009**, *106*, 18497–18502.
- (35) Low, D. W.; Hill, M. G. *J. Am. Chem. Soc.* **2000**, *122*, 11039–11040.
- (36) Shen, B.; Jollie, D. R.; Stout, C. D.; Diller, T. C.; Armstrong, F. A.; Gorst, C. M.; La Mar, G. N.; Stephens, P. J.; Burgess, B. K. *J. Biol. Chem.* **1994**, *269*, 8564–8575.

*Chapter 4***INVESTIGATION OF REPAIR PROTEIN EXPRESSION LEVELS
AND DNA-MEDIATED SIGNALING IN GENOME-WIDE
LESION DETECTION**

4.1 Introduction

Previous work using DNA-modified electrochemistry on repair proteins has suggested a system where the 4Fe4S redox couple for these proteins can be accessed interchangeably between each other due to sharing a common redox potential of $\sim 80\text{mV}$ vs. NHE [1–4]. Different cluster-containing repair proteins of different function and domains of life have been shown using atomic force microscopy (AFM) to localize to DNA mismatches using the DNA-binding affinity redox switch [5, 6]. This idea is the basis for the DNA-mediated redox signaling for lesion detection in the genome. In this system, the expression levels of each iron-sulfur DNA repair protein should sum up to create an optimal global genome scanning mechanism. If all 4Fe4S cluster containing DNA repair enzymes contributed equally to the efficiency of DNA repair by helping each other localize to the appropriate lesion, knocking out a specific cluster-containing repair protein should decrease the efficiency of other cluster-containing repair proteins to localize to lesions (Figure 4.1). This model was demonstrated in a cellular assay when DinG, a ATP-dependent 4Fe4S helicase involved in R-loop maturation, was inefficient in its ability to resolve deleterious R-loops after Endonuclease III (EndoIII), a 4Fe4S base excision repair enzyme, was knocked out of the system [7]. Mechanistic details of this unique interaction between the 4Fe4S clusters of DNA repair proteins remain uncharacterized. Here we study the relationship between the expression level of these 4Fe4S DNA repair proteins and its effect on DNA-mediated redox signaling for the detection of DNA lesions.

Investigation of the effect of DNA repair protein expression levels on repair efficiency *in vivo* hinges on the optimization of two experimental aspects: an assay that queries DNA-mediated redox signaling and a technique to tune protein expression precisely. Multiple approaches can be used to tune protein expression by at the transcription and translation levels. The most well-known method for tuning expression is utilizing different plasmid promoter-repressor systems. Propionate, arabinose, and lactose operons are examples of systems used to regulate transcription of the desired gene [8–10]. All of these regulation systems hinge on a repressor containing a binding site for their mentioned metabolite that deactivates repression, thus causing a turn-on effect for transcription. Another approach for tuning is using the CRISPR interference (CRISPRi) system where a guide RNA is designed to target the gene of interest to act as a transcriptional roadblock against that gene [11]. Additionally, plasmids or genomes can be edited to contain a stronger or weaker ribosome binding site (RBS) which affects the rate of translation initiation of the

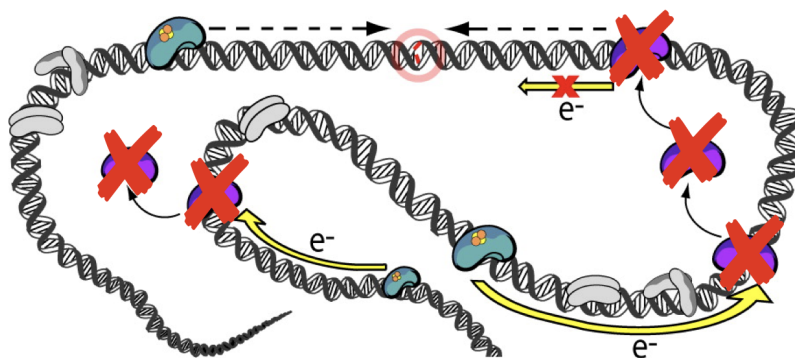


Figure 4.1: Illustration of the consequence of protein copy number on the scanning model. Given a lesion highlighted in the red circle that is a substrate for only the teal-colored protein, the efficiency of the teal 4Fe4S repair protein should decrease as the purple-colored 4Fe4S proteins are taken out of the system, as there are now fewer proteins overall participating in redox-signaling and scanning the genome.

gene of interest, allowing for additional depth in tuning copy numbers of proteins [12]. Finally, genome integration of these promoter-repressor constructs provides an additional level of specificity by ensuring only one single copy of the gene of interest is inside each cell [13].

Two cell-based assays were used to report on the efficiency DNA-mediated redox signaling and downstream repair efficiency. The InvA growth assay looks at the efficiency of DinG helicase activity to resolve deleterious R-loops and was used to demonstrate DNA-mediated redox signaling between EndoIII and DinG previously [7]. The UV-sensitivity assay involves irradiation of *E. coli* with UV to assess the efficiency of nucleotide excision repair (NER) after knockout of 4Fe4S protein signaling partners. In this work we uncover the effect of various 4Fe4S proteins on the efficiency of R-loop maturation and attempt to connect 4Fe4S DNA repair protein copy number with global DNA repair efficiency.

4.2 Materials and Methods

P1 Phage transduction

P1 phage transduction was used in order to generate InvA Δ nth and InvA Δ muty for the InvA growth assay. The donor strain of either Δ nth or Δ muty was grown overnight with antibiotic selection. This overnight was then diluted 1:100 into 2mL of fresh LB with 20mM MgCl₂, 5mM CaCl₂, and 0.1% glucose. After ~2 hours of growth at 37C, 40 μ L of P1 phage was added to the mixture and the mixture

was allowed to grow until all cells had been lysed by the phage (3 hours). 50 μ L of chloroform was then added to the lysate. Following brief vortex, the lysate was spun down in small 1.5 mL centrifuge tubes at 14000 rpm for 2 minutes. The supernatant was preserved and a few more drops of chloroform was added to the mixture for sterilization. The recipient strain InvA was grown overnight in the appropriate antibiotics. The cells were then pelleted at 6000rpm for 2min followed by resuspension in 300 μ L LB with 10mM MgSO₄ and 5mM CaCl₂. 100 μ L of p1 lysate was added into 100 μ L of recipient cells and incubated for 30 minutes at 37C. 200 μ L of 1M Na-Citrate at pH 5.5 and 1mL of pure LB was added and the culture was shaken for 1 hour to allow for antibiotic resistance expression. Cells are then spun down at 6000rpm for 5 minutes, decanted, and resuspended with 100 μ L of LB with 100mM Na-Citrate. This cell aliquot was then spread on an LB-plate with the correct antibiotics. InvA Δ muty strain creation was performed with Dr. Michael Grodick. Colony PCR was performed on InvA to verify *rrnA* operon inversion and gene knockout using primers listed in Table B.2.

Next generation sequencing of InvA Δ muty

Putative InvA Δ muty was processed with a blood and tissue DNA extraction kit (Qiagen). The extracted genome of InvA Δ muty was subject to Illumina sequencing with a read length of 100bp for 8 million reads to ensure adequate coverage of the entire genome. The acquired fastq files were aligned using bowtie-2 software against the reference genome of K-12 E. coli NC_008253 and converted, merged, sorted, and indexed into the appropriate genome file using samtools. Sequence alignments were visualized using the Integrative Genomics Viewer (IGV).

InvA growth assay

Overnight cultures of the E. coli InvA Δ nth containing various rescue plasmids were prepared by inoculating single colonies in 3 mL of LB media containing 50 μ g/mL ampicillin. After overnight growth of ~20 hours, 50 μ L of the culture was placed into a 10mL multichannel pipette tray with 10mL of LB-amp along with inducer at varying concentrations if applicable. Strains were then put into columns in the microplate depending on rescue plasmid genotype. The microplates were then subject to shaking at 37C for 12 hours taking an OD600 or 630 reading every 10 minutes. Plate reader data was saved to a .csv and data analysis was performed using scripts written in *python 3.6.5* using *matplotlib*, *seaborn*, and *bokeh* for data visualization [14–16].

Creation of pBAD, pPro, pLac plasmids for EndoIII expression

In order to tune protein expression, propionate, lactose, and arabinose based inducible systems were used and are designated as pPro, pLac, and pBAD respectively. Plasmids were assembled via Gibson assembly using vectors acquired from Addgene. pLac plasmid backbone is from pBbS5a-RFP (Plasmid# 35283 Addgene), pPro plasmid backbone is from pPro30 (Plasmid# 17809 Addgene), and pBAD plasmid backbone is pBbS8a-RFP (Plasmid# 35274 Addgene) [8, 17]. RFP insert was taken from pBbS5a-RFP or pBbS8a-RFP (both are identical) and EndoIII inserts extracted from either the *E.coli* genome using colony PCR or from the lab EndoIII overexpression plasmid. RFP was used either as a control or, in some cases, fused to the N or C-terminus of nth for future experiments to quantify EndoIII expression. Primers used are listed in Table B.3.

UV sensitivity colony counting assay

Overnight cultures of the *E. coli* Δ nth or Δ muty containing various pBAD rescue plasmids were prepared by inoculating single colonies in 5 mL of LB media containing 100 μ g/mL ampicillin and 50 μ g/mL kanamycin. 200 μ M or 50 μ M arabinose was added during this step for some assays. After overnight shaking at 37C, the cultures were diluted 1:500 into 10 mL of fresh LB media also containing antibiotics. Cultures were then treated with either 50 μ M of arabinose if not induced during the overnight step. Cultures were then incubated at 37C for 3 hours. An OD₆₀₀ measurement was taken and cell concentrations were adjusted to match optical density using phosphate buffered saline (PBS) to an OD₆₀₀ of 0.4 and then diluted 20200-fold and placed into a transparent petri dish. These dishes were placed inside the UVP-crosslinker and subject to one treatment of UV radiation at 30J/m². 10 μ L of the solution of cells was then taken from the petri dishes and placed into patterns on a plate as droplets. The plate was then tilted to allow for the cell droplets to spread and grow on a bigger surface area and thus allowing for easier counting. Plates were then incubated at 37C overnight. Resultant plates are imaged using a BioRad gel imager on the Coomassie blue setting. Colonies are counted up with the assistance of OpenCFU software (Figure 4.2) [18]. Regions of interests can be manually drawn out and the software will count automatically.

Genome integration of pBAD-nth

Integration of WT, D138, and Y82A EndoIII gene *nth* was accomplished using the clonetegration technique [13]. The *nth* gene insert under an arabinose promoter

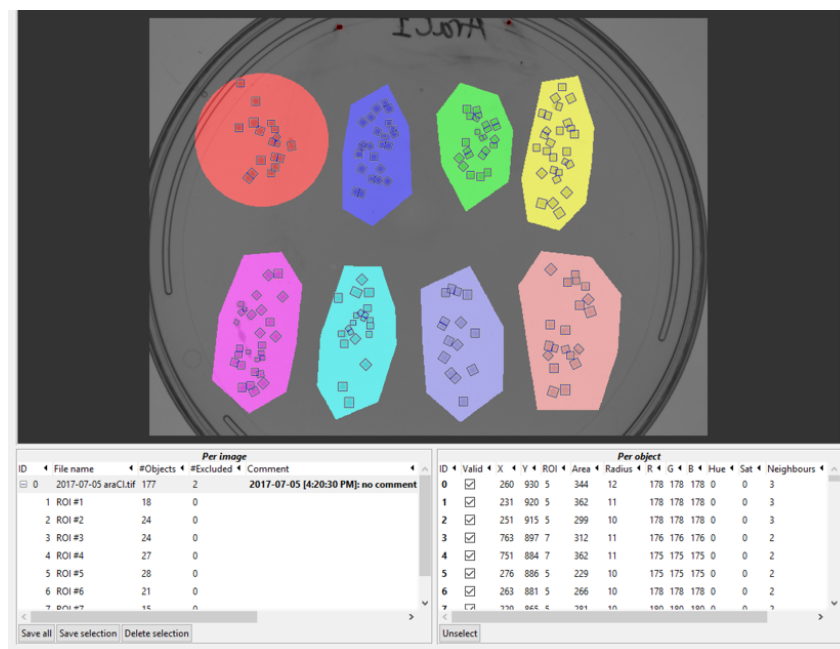


Figure 4.2: OpenCFU interface for drawing regions of interest and counting colonies.

including araC operators was cloned into the cloning module using Gibson assembly. The parent insert contains a toxic ccdB gene to prevent parent plasmid transformed strains from proliferating. Additionally, pOSIP contains a R6K γ origin of replication which can only replicate in strains that are pir⁺. This means that during integration of other strains, the integration plasmid will not replicate and thus only one copy is allowed to integrate. Integration occurs via the lambda integrase which takes the attP site on pOSIP and finds a matching attB site inside the genome of *E. coli*. Thus, integration only occurs at a specific place inside the strain. Additionally, the flanking terminators integrated into the genome ensure that transcription of the gene insert is exclusive to itself and is unaffected and will not affect endogenous transcription. Primers used for creation of clonetegration plasmids are listed in Table B.1. Colony PCR performed to confirm genome integration.

Plate-reader UV-sensitivity assay

Overnight starter cultures of Δ araC(pRFP) and Δ nth transformed or genome integrated with WT, D138A, or Y82A EndoIII were cultured similarly to the above protocol. After OD₆₀₀ adjustment of all strains to the same OD, a 16-fold dilution into PBS was performed on each strain into a transparent petri-dish for 254nm UV-irradiation at 90J/m². After treatment, the cell solution was diluted 16-fold into

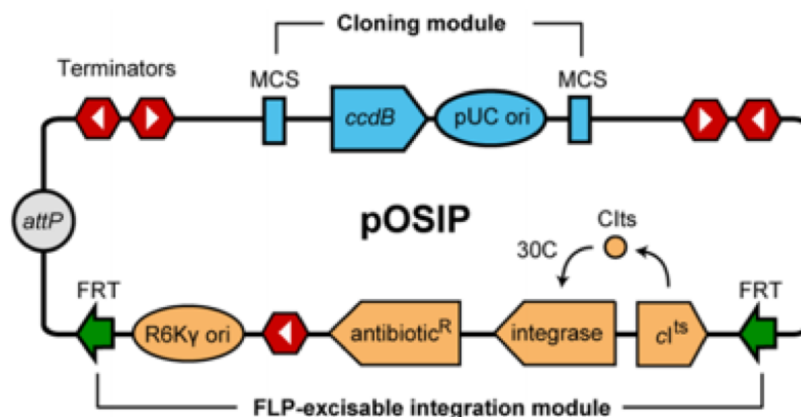


Figure 4.3: Clonetegration genome integration module developed by Endy et al. Adapted with permission from St-Pierre, F. et al. ACS Synth. Biol. 2013, 2, 537. Copyright 2013 American Chemical Society.

7mL LB with 100 μ g ampicillin. 200 μ L of each genotype was placed into a unique column in a 96-well microplate and placed into a plate-reader (BioTek) for OD₆₀₀ readings every 10 minutes over 670 minutes in total. Plate reader data was saved to a .csv and data analysis was performed using scripts written in *python 3.6.5* using *matplotlib*, *seaborn*, and *bokeh* for data visualization.

4.3 Results

InvA growth phenotype differs depending on gene knockout identity

Previous results of the InvA growth assay demonstrated signaling between EndoIII and DinG [7]. To summarize, the InvA strain contains an inversion of the highly transcribed *rrnA* operon. This inversion creates frequent collisions between transcription and replication machinery and results in the formation of R-loops which must be resolved by DinG helicase [19]. Knocking out BER glycosylase EndoIII in the InvA strain (InvA Δ nth) causes a severe growth defect suggesting EndoIII signaling to DinG to locate deleterious r-loops efficiently. Additionally, this growth defect is only rescued with the addition of EndoIII constructs capable of conducting DNA CT, as any point mutations negatively affecting EndoIII DNA-CT does not rescue growth in these InvA Δ nth cells (Figure 4.4). Given these results, the InvA growth assay could provide a means to measure DNA-mediated redox signaling between DinG and any 4Fe4S protein. We tested the effect of knocking out MutY, a 4Fe4S containing DNA glycosylase, on the growth of the InvA strain by creating the InvA Δ muty strain and comparing growth with the InvA strain (Figure

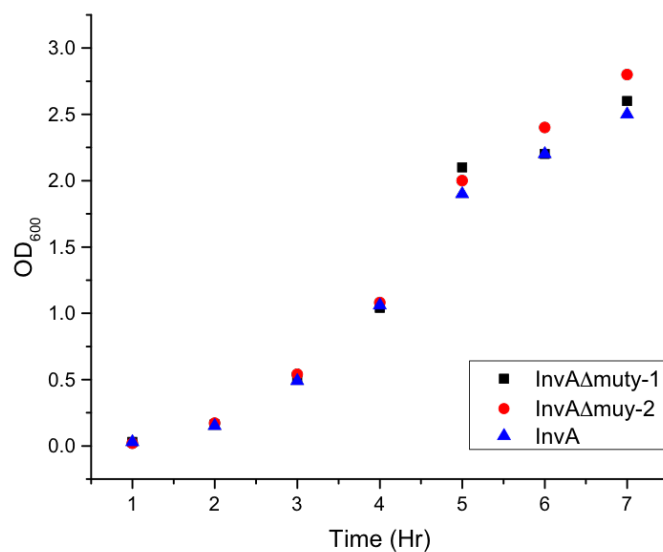


Figure 4.4: Growth of InvAΔmuty compared with InvA measured through optical density over 7 hours.

4.4). We observed no differences in growth between InvAΔmuty and InvA. Thus, MutY glycosylase does not assist DinG in any manner for locating R-loops or the assistance is so minimal that it is undetectable by this growth assay. This result implies that there is an uncharacterized difference between EndoIII and MutY that causes EndoIII to be the preferred DNA-mediated redox signaling partner for DinG. This difference may be found in the relative expression levels of these proteins.

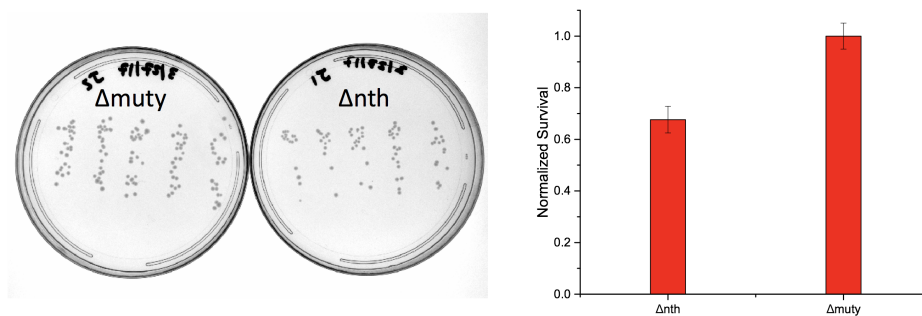


Figure 4.5: UV sensitivity colony count assay of Δnth and Δmuty strains after treatment with $30J/m^2$ UV. Pictures of colonies for each knockout strain (left) and a histogram (right).

To further confirm this difference in cellular preference of redox-signaling

partner between EndoIII and MutY, we utilized another DNA repair growth assay to see if the preference for EndoIII still remained (Figure 4.5). By knocking out either EndoIII or MutY from MG1655 *E.coli* and treating them with UV, we can assess the ability for these two DNA glycosylases to signal to NER through UvrC Endonuclease. The results show that the Δ nth strain was more sensitive to UV irradiation than the Δ muty strain, reflected by the difference in surviving fraction after treatment. This result maintains the trend that EndoIII is a preferred redox signaling partner and suggests that potential expression level differences between EndoIII and MutY can explain this trend.

Plasmid-based rescue of UV-sensitivity through EndoIII expression

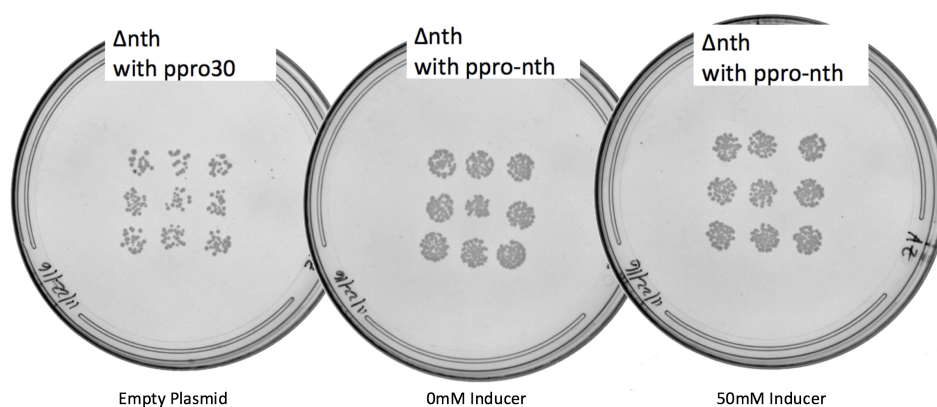


Figure 4.6: LB-plates containing droplets of Δ nth with pPro30-nth or empty rescue plasmid after treatment with $30J/m^2$ UV with varying propionate inducer concentrations.

In order to investigate the effect of protein copy number for the rescue of the UV-sensitivity growth phenotype, a tunable plasmid-based system was devised and tested. Our initial attempts utilized the propionate inducible pathway which is regulated by the promoter P_{prpB} and a $prpR$ positive regulator [8, 20]. When performing the UV-sensitivity assay with Δ nth and either an empty plasmid or one expressing EndoIII, we observed rescue of the growth defect but no inducible response when adding 50mM of propionate inducer (Figure 4.6). Thus we confirmed UV-sensitivity of Δ nth can be rescued with expression of EndoIII but cannot be induced using this system.

To achieve a tunable rescue system, we next attempted to utilize a lac-operon transcriptional regulation machinery. This system is widely used for controlling expression of proteins of interest in protein purification applications. This plasmid

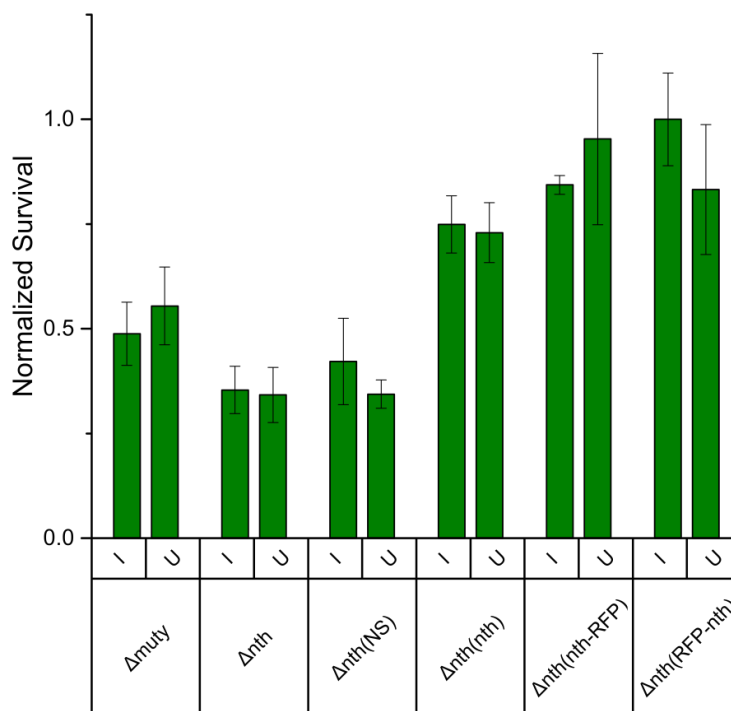


Figure 4.7: Normalized survival from UV-sensitivity droplet assay using pLac. Strains of Δ nth with various rescue plasmids were treated with $30J/m^2$ UV and plated as droplets. Colonies were quantified and the fraction survival was calculated and normalized to best surviving conditions. (I) and (U) stand for induced and uninduced, respectively, with induction meaning a final concentration of $50 \mu M$ of IPTG. (NS) means "nonsense" and contains a pLac plasmid expressing a nonsense peptide. Data presented are of three biological replicates.

is regulated through a lac promoter with a *lacO* binding site onto which the lac repressor, *LacI*, binds to regulate transcription. This setup was necessary in order to attain the desired tunability of our plasmid rescue system. However, basal expression of EndoIII was enough to rescue UV-sensitivity of Δ nth cells (Figure 4.7). All knockout cells and cells expressing nonsense peptides were more sensitive to UV-irradiation than their EndoIII expressing counterparts regardless of the presence of an RFP-fusion to EndoIII. Full rescue of the UV-sensitivity was achieved before addition of inducer and addition of inducer had no significant effect on rescue.

The final system we decided to utilize for creating a tunable EndoIII plasmid was the arabinose operon transcriptional regulatory machinery. This system is known for its lack of basal protein expression and is considered the gold-standard for preventing leaky expression in synthetic biology applications. These plasmids are regulated through an arabinose P_{BAD} promoter with regulatory protein AraC

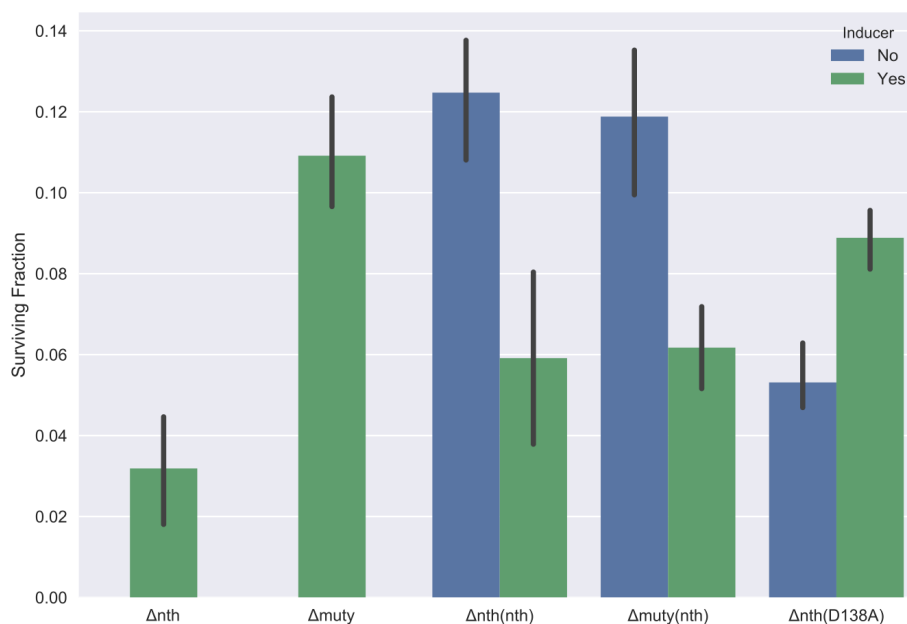


Figure 4.8: Normalized survival from UV-sensitivity droplet assay using pBAD. Strains of Δnth with various rescue plasmids were treated with $30 J/m^2$ UV and plated as droplets. Colonies were quantified and the fraction survival was calculated and normalized to best surviving conditions. Arabinose inducer concentration was $50 \mu M$ when added. Data presented are of three biological replicates.

which, depending on arabinose presence, can act as a repressor or activator of the system. When applying this system to tune EndoIII expression for the UV-sensitivity assay, we find that rescue of the growth phenotype occurs without the addition of inducer (Figure 4.8). Addition of arabinose inducer decreases cell survival after UV treatment at a $50 \mu M$ arabinose and no colonies grew at $200 \mu M$ (Figure 4.9).

Genome integration with inducible expression of EndoIII introduces cellular burden

From our plasmid-based UV-sensitivity experiments, we concluded that basal expression from any plasmid system was enough to rescue the growth defect. Depending on origin of replication, plasmids can be maintained at varying copy numbers inside *E. coli* which increases the basal expression of the rescue protein due to the multiple plasmid-DNA copies of EndoIII in each cell. We performed genome integration of pBAD-nth to bypass the issue of multiple copy numbers for the plasmid approach. After $90 J/m^2$ UV-treatment of Δnth with genome-integrated WT, D138A, and Y82A EndoIII, we observe a decrease in growth rate and carrying

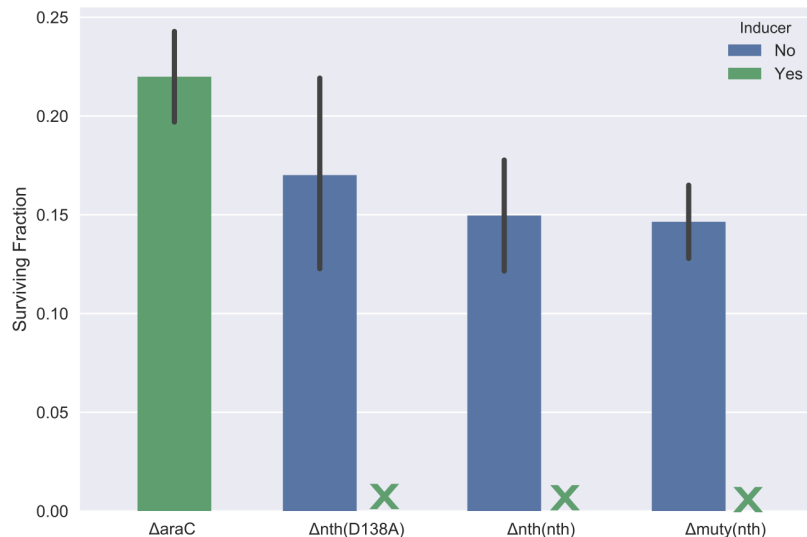


Figure 4.9: Normalized survival from UV-sensitivity droplet assay using pBAD. Strains of Δnth with various rescue plasmids were treated with $30J/m^2$ UV and plated as droplets. Colonies were quantified and the fraction survival was calculated and normalized to best surviving conditions. Arabinose inducer concentration was $200 \mu M$ when added. Data presented are of three biological replicates.

capacity with increasing arabinose inducer concentration. The decrease in growth rate and carrying capacity occurs regardless of EndoIII point-mutation and suggests that the growth-defect observed is likely due to an increase in cellular burden.

InvA Δnth experiences escape mutations from programmed growth defect

We wanted to apply the various tunable protein expression setups we have developed to the InvA growth assay to confirm whether the rescue trends we observed in the UV-sensitivity assay hold for the InvA growth assay. Using lab strains from previous work, we were able to replicate results of the InvA growth assay with our constitutively-expressing *nth* rescue plasmid (Figure 4.11). After introducing our tunable pBAD plasmid system to InvA, we observe a less dramatic growth defect for Y82A and an decrease in carrying capacity for WT EndoIII compared to previous results (Figure 4.12). Additionally, these InvA Δnth strains seem to suffer from escape mutations where the growth defect is bypassed over time, as demonstrated by the similar growth curves between Y82A and WT (Figure 4.13). This resulted in multiple fruitless attempts to recreate the InvA Δnth strain, as the strain would attain

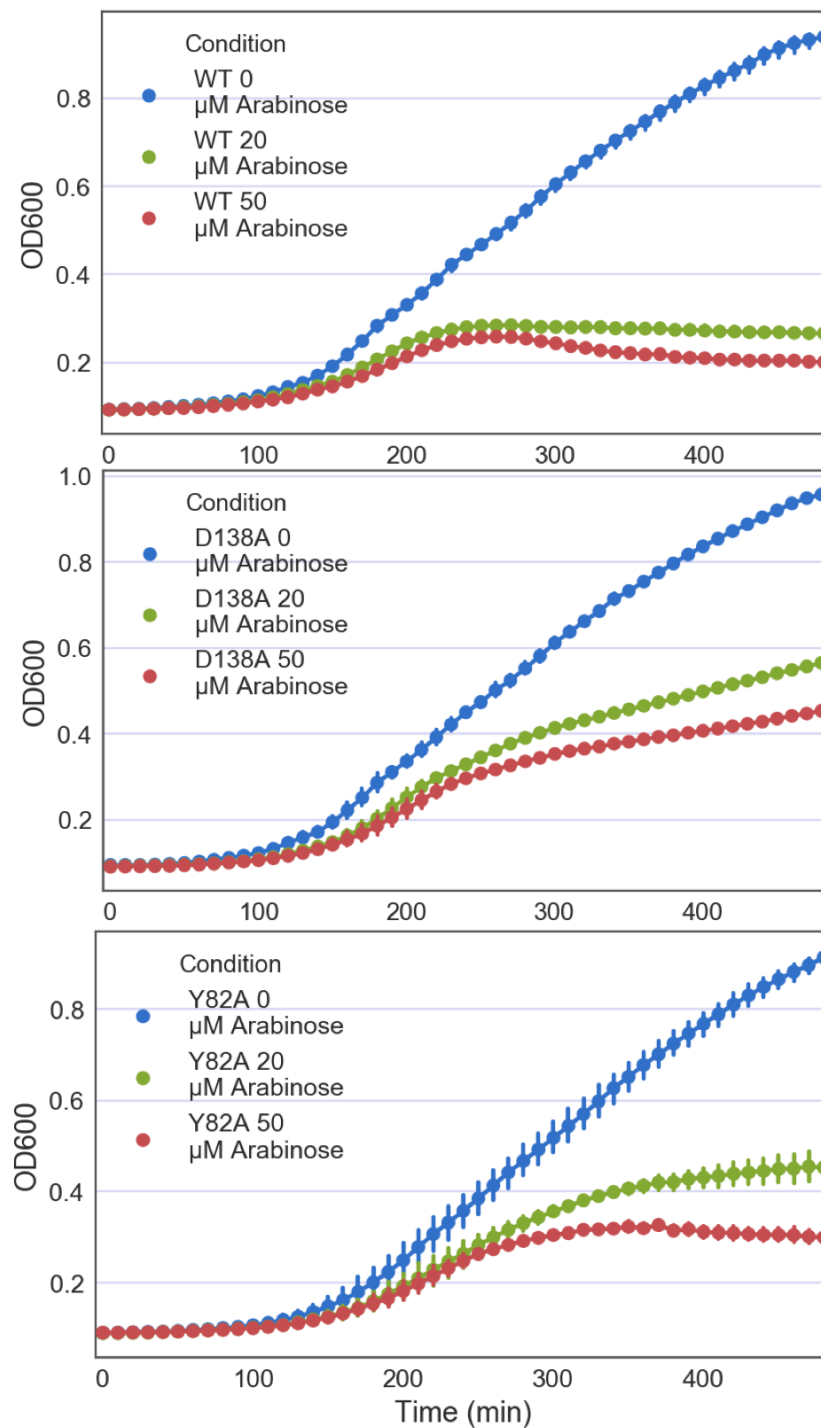


Figure 4.10: Growth curves of Δnth with genome-integrated WT, D138A, and Y82A EndoIII with varying amounts of arabinose inducer added. 95% confidence intervals are calculated using the bootstrap method for 16 technical replicates.

these escape mutations immediately after P1 phage transduction and thus display no growth defect before rescue.

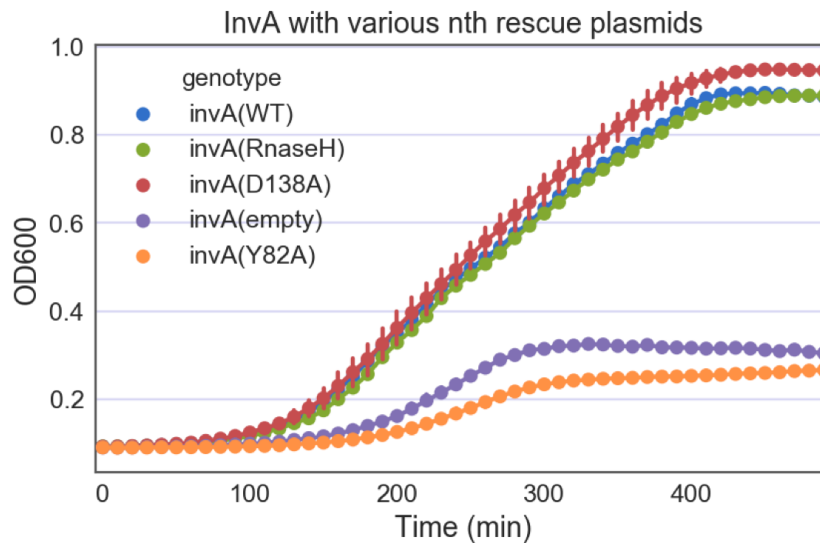


Figure 4.11: Growth curves of $InvA\Delta nth$ with various EndoIII rescue plasmids replicated using strains from Grodick et al [7]. 95% confidence intervals are calculated using the bootstrap method for 16 technical replicates.

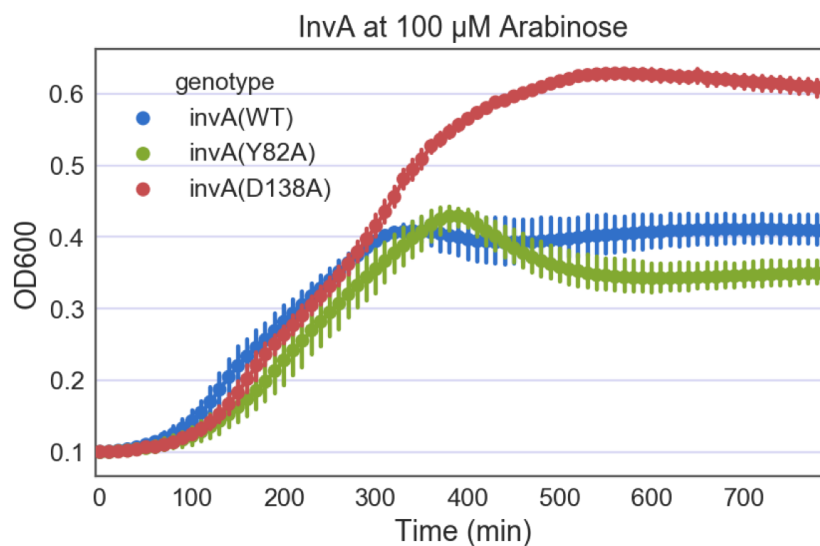


Figure 4.12: Growth curves of $InvA\Delta nth$ with pBAD EndoIII rescue plasmids at various arabinose inducer concentrations. 95% confidence intervals are calculated using the bootstrap method for 16 technical replicates.

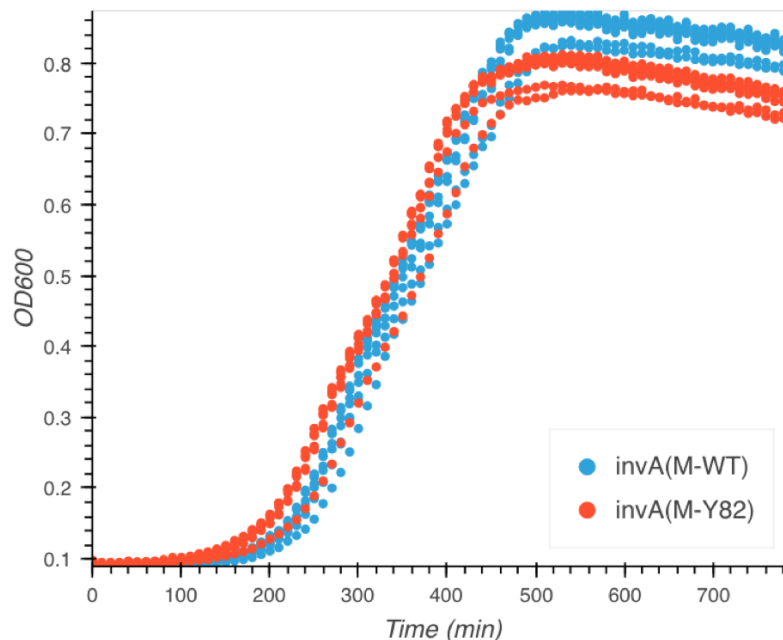


Figure 4.13: Growth curves of *InvA* Δ *nth* strains with rescue plasmids from Grodick et al after 2 overnight growth cycles with antibiotic selection. Technical replicates are plotted individually.

Preservation of endogenous DNA and mRNA contexts allows for WT *EndoIII* rescue of UV sensitivity

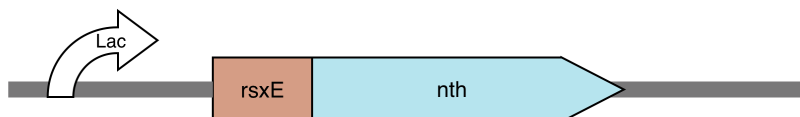


Figure 4.14: Design of rescue plasmids used in previous works [5, 7]. A 5' extension 283 base pairs upstream of *EndoIII* (*rsxE*) is added into the plasmid.

Even though we observed a lack of rescue of growth defects when using WT *EndoIII* as seen in Figure 4.12, previous works have shown a plasmid design where WT *EndoIII* could rescue growth defects [5, 7]. This plasmid setup, displayed in Figure 4.14, utilizes a 5' extension 283 base pairs upstream of *EndoIII* (*rsxE*). This addition allows for the WT *EndoIII* plasmid to rescue the UV sensitivity growth defect (Figure 4.15). From the UV-sensitivity assay growth curves in Figure 4.15, we see that the lag-time of Δ *nth* is decreased by ~1 hour, suggesting an increase in cellular fitness after UV irradiation when WT *EndoIII* is present [21].

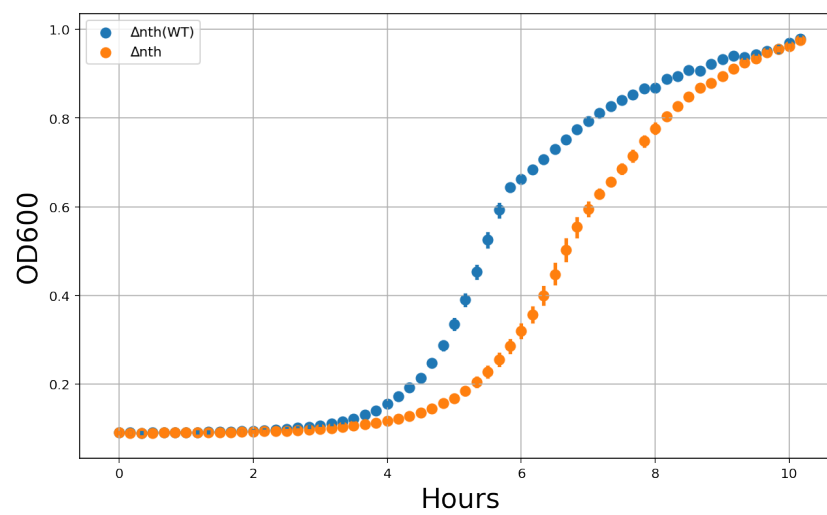


Figure 4.15: Growth of the Δnth strain with and without the WT EndoIII rescue plasmid.

4.4 Discussion

We have uncovered details about the effect of the protein expression levels on the efficiency of DNA-mediated redox signaling for DNA lesion detection. EndoIII is the preferred redox-signaling partner over MutY for multiple repair pathways. We demonstrated this preference in both UV-sensitivity and InvA growth assays when comparing the magnitude of the growth defect in Δ nth and Δ muty strains (Figures 4.4, 4.5). From our UV-sensitivity results, very low expression levels of EndoIII were enough to fully rescue growth phenotypes as all tunable expression setups rescued before addition of inducer (Figures 4.7, 4.9). Overexpression of WT EndoIII exacerbated strain growth after UV-treatment whereas overexpression of D138A, a catalytically deficient EndoII point-mutant, did not. Thus, an excess of enzymatically active EndoIII harms the cell during the dire need for proper DNA repair, likely due to non-specific enzyme activity. These results suggest that the DNA lesion scanning system, composed of 4Fe4S DNA repair proteins, is a finely tuned system that is sensitive to perturbation. Overexpression of one of the components, EndoIII, could have made scarce important cellular resources. Given that these 4Fe4S proteins requires the expression and fidelity iron-sulfur assembly pathway, a multi-protein network for the assembly and loading of FeS clusters, the metabolic tax of EndoIII overexpression was likely overwhelming for the cell [22]. Even with genome integration, addition of inducer always decreased cellular growth, further confirming the aforementioned metabolic tax (Figure 4.10).

We did successfully characterize one plasmid feature that led to rescue of growth defects with WT EndoIII. From Figure 4.14 and 4.15, we see that addition of a 5' extension 283 base pairs upstream of EndoIII (*rsxE*) allows for WT EndoIII to rescue the UV sensitivity growth defect. The protein product of *rsxE*, a trans-membrane subunit of an oxidoreductase complex [23], is likely unimportant to the observed rescue as this 5' extension does not contain any in-frame or deleterious out-of-frame start codons. Instead, with the addition of this *rsxE* extension, the DNA and mRNA plasmid contexts are affected in such a way that they replicate endogenous conditions. An endogenous DNA context preserves any relevant promoters that may exist upstream of the EndoIII gene which allows for more accurate transcription. Perhaps more vitally, an endogenous mRNA context preserves the RBS for a biological magnitude of translation of EndoIII. RBS content has the ability to tune protein expression over 5 orders of magnitude [12] and thus is extremely important for maintaining expression levels of EndoIII that avoid over-allocation of cellular resources and excess non-specific enzyme activity, which both have proven

to be detrimental to cellular fitness.

While these protein expression levels should indeed affect the efficiency of DNA-mediated redox signaling, they should not be the only contributing factor. When comparing 4Fe4S proteins MutY and EndoIII, we observed using UV-sensitivity and InvA growth that EndoIII is the preferred DNA-mediated redox signaling partner for UvrC and DinG respectively. However, when comparing expression levels between these two proteins attained from ribosome profiling and single-molecule counting, their numbers are similar [24, 25]. If EndoIII and MutY copy numbers are similar, there should exist biochemical or electrochemical differences between EndoIII and MutY that accounts for the preference for EndoIII as a redox-signaling partner for multiple repair pathways. Nonspecific DNA-binding affinity differences between MutY and EndoIII could explain a preference for EndoIII in DNA-mediated redox signaling. $[\text{Fe}_4\text{S}_4]^{2+}$ EndoIII has a measured non-specific DNA binding affinity of $\sim 6 \mu\text{M}$ whereas $[\text{Fe}_4\text{S}_4]^{2+}$ MutY has a non-specific DNA-binding affinity of $\sim 0.3 \mu\text{M}$ [26, 27]. This difference may cause MutY to bind too tightly in its reduced form to be an ideal redox signal mediator through DNA when compared to EndoIII. When uncovered, these *in vitro* biochemical differences between EndoIII and MutY may provide additional insight into the protein network of DNA-mediated redox signaling.

In order to investigate the effect of expression levels of DNA repair proteins on the fidelity of DNA-mediated redox signaling, we needed to develop a tunable protein-expression system that would not interfere with the growth rate of *E.coli*. The acquisition of this goal is an ongoing research effort. In 2015, Ceroni et al characterized and quantified the burden introduced by heterologous gene expression [28]. From their results, addition of inducer causes a decrease in growth rate similar to the decreases observed in our UV-sensitivity assays after addition of inducer (Figure A.11). Therefore, cellular burden must be consistent between all strains and maintain consistency through the timeline of the assay. One approach to achieve this consistency is to make multiple plasmids that are "fixed-points" spanning a range of protein expression levels. The goal of this set of plasmids is to span all the desired protein levels to assess but have the same cellular burden as measured using a GFP capacity-monitor technique detailed in Ceroni et al. To achieve similar overall cellular burden, plasmids expressing less EndoIII rescue protein will also express a dummy protein to counteract the increased burden encountered with plasmids expressing more EndoIII.

Another approach to circumvent the issue of cellular burden is to utilize an assay that bypasses using cellular growth to report on DNA repair fidelity. An assay where DNA repair events lead to a turn on fluorescent signal could be used to bypass the negative effects of cellular burden as repair events can be normalized to average fluorescence per cell. Though the fluorescent intensities may still be affected by cellular burden, the magnitude of expression of the reporter may be small enough that it does not feel the effects of resource re-allocation as strongly as something more resource-intensive such as growth. Finally, single-particle tracking of these repair proteins can be performed using super-resolution microscopy. This technique was used to measure diffusion coefficients of various DNA-processing enzymes and characterize the cellular localization and dynamics of NER proteins UvrA and UvrB [29, 30]. Using this approach, we may be able to record DNA-mediated redox signaling frame-by-frame in a movie that captures 4Fe4S DNA repair proteins localizing to DNA lesions.

Finally, development of an assay that does not depend on cellular growth avoids the development of escape mutations in the assessed strain. This was evident in the InvA growth assay, where the growth defect is not stable through multiple growth generations (Figure 4.13). The InvA Δ nth strain quickly finds a way to bypass its growth defect thus making it difficult to be created or made competent for plasmid transformation. Overall, we have demonstrated that DNA-mediated redox signaling is a well-connected network that is extremely sensitive to perturbation. Future work to investigate this complex network requires careful experimental design.

References

- (1) Boal, A. K.; Yavin, E.; Lukianova, O. A.; O'Shea, V. L.; David, S. S.; Barton, J. K. *Biochemistry* **2005**, *44*, 8397–8407.
- (2) Gorodetsky, A. A.; Barton, J. K. *Langmuir* **2006**, *22*, 7917–7922.
- (3) Bartels, P. L.; Zhou, A.; Arnold, A. R.; Nuñez, N. N.; Crespilho, F. N.; David, S. S.; Barton, J. K. *Langmuir* **2017**, *33*, 2523–2530.
- (4) Mui, T. P.; Fuss, J. O.; Ishida, J. P.; Tainer, J. A.; Barton, J. K. *J. Am. Chem. Soc.* **2011**, *133*, 16378–16381.
- (5) Boal, A. K.; Genereux, J. C.; Sontz, P. A.; Gralnick, J. A.; Newman, D. K.; Barton, J. K. *Proc. Natl. Acad. Sci. U.S.A.* **2009**, *106*, 15237–15242.
- (6) Sontz, P. A.; Mui, T. P.; Fuss, J. O.; Tainer, J. A.; Barton, J. K. *Proc. Natl. Acad. Sci. U.S.A.* **2012**, *109*, 1856–1861.
- (7) Grodick, M. A.; Segal, H. M.; Zwang, T. J.; Barton, J. K. *J. Am. Chem. Soc.* **2014**, *136*, 6470–6478.
- (8) Lee, S. K.; Keasling, J. D. *Appl Environ Microbiol* **2005**, *71*, 6856–6862.
- (9) Hansen, L. H.; Knudsen, S.; Sørensen, S. J. *Curr. Microbiol.* **1998**, *36*, 341–347.
- (10) Khlebnikov, A.; Datsenko, K. A.; Skaug, T.; Wanner, B. L.; Keasling, J. D. *Microbiology (Reading, Engl.)* **2001**, *147*, 3241–3247.
- (11) Larson, M. H.; Gilbert, L. A.; Wang, X.; Lim, W. A.; Weissman, J. S.; Qi, L. S. *Nat. Protocols* **2013**, *8*, 2180–2196.
- (12) Salis, H. M. *Meth. Enzymol.* **2011**, *498*, 19–42.
- (13) St-Pierre, F.; Cui, L.; Priest, D. G.; Endy, D.; Dodd, I. B.; Shearwin, K. E. *ACS Synth. Biol.* **2013**, *2*, 537–541.
- (14) McKinney, W. In *Proceedings of the 9th Python in Science Conference*, ed. by Walt, S. v. d.; Millman, J., 2010, pp 51–56.
- (15) Hunter, J. D. *Computing in Science Engineering* **2007**, *9*, 90–95.
- (16) Jones, E.; Oliphant, T.; Peterson, P. **2001**.
- (17) Lee, T. S.; Krupa, R. A.; Zhang, F.; Hajimorad, M.; Holtz, W. J.; Prasad, N.; Lee, S. K.; Keasling, J. D. *J Biol Eng* **2011**, *5*, 12.
- (18) Geissmann, Q. *PLOS ONE* **2013**, *8*, e54072.
- (19) Boubakri, H.; de Septenville, A. L.; Viguera, E.; Michel, B. *EMBO J* **2010**, *29*, 145–157.
- (20) Lee, S. K.; Newman, J. D.; Keasling, J. D. *J Bacteriol* **2005**, *187*, 2793–2800.

- (21) Rolfe, M. D.; Rice, C. J.; Lucchini, S.; Pin, C.; Thompson, A.; Cameron, A. D. S.; Alston, M.; Stringer, M. F.; Betts, R. P.; Baranyi, J.; Peck, M. W.; Hinton, J. C. D. *J Bacteriol* **2012**, *194*, 686–701.
- (22) Blanc, B.; Gerez, C.; Ollagnier de Choudens, S. *Biochim. Biophys. Acta* **2015**, *1853*, 1436–1447.
- (23) Koo, M.-S.; Lee, J.-H.; Rah, S.-Y.; Yeo, W.-S.; Lee, J.-W.; Lee, K.-L.; Koh, Y.-S.; Kang, S.-O.; Roe, J.-H. *EMBO J.* **2003**, *22*, 2614–2622.
- (24) Li, G.-W.; Burkhardt, D.; Gross, C.; Weissman, J. S. *Cell* **2014**, *157*, 624–635.
- (25) Taniguchi, Y.; Choi, P. J.; Li, G.-W.; Chen, H.; Babu, M.; Hearn, J.; Emili, A.; Xie, X. S. *Science* **2010**, *329*, 533–538.
- (26) Tse, E. C. M.; Zwang, T. J.; Barton, J. K. *J. Am. Chem. Soc.* **2017**, *139*, 12784–12792.
- (27) Lu, A.-L.; Tsai-Wu, J.-J.; Cillo, J. *J. Biol. Chem.* **1995**, *270*, 23582–23588.
- (28) Ceroni, F.; Algar, R.; Stan, G.-B.; Ellis, T. *Nat. Methods* **2015**, *12*, 415–418.
- (29) Uphoff, S.; Reyes-Lamothe, R.; Leon, F. G. d.; Sherratt, D. J.; Kapanidis, A. N. *PNAS* **2013**, *110*, 8063–8068.
- (30) Stracy, M.; Jaciuk, M.; Uphoff, S.; Kapanidis, A. N.; Nowotny, M.; Sherratt, D. J.; Zawadzki, P. *Nature Communications* **2016**, *7*, 12568.

*Chapter 5***REPAIR PATHWAY CROSSTALK BETWEEN BASE EXCISION
REPAIR AND NUCLEOTIDE EXCISION REPAIR IN *E. COLI***

5.1 Introduction

The 4Fe4S cluster is a metal cofactor utilized in biology for a variety of different functions in catalysis and electron transport [1]. Recently, a novel functional role for the cluster has been identified for proteins in DNA-repair and replication as a redox switch for DNA-binding [2, 3]. Human DNA primase utilizes this redox switch to coordinate primer handoff in replication[4]. For DNA-polymerase δ , enzymatic activity is tuned by the redox switch, allowing for a fast and reversible regulation of replication in response to oxidative stress[5]. In all cases, the redox of the 4Fe4S cluster is achieved through DNA-mediated charge transport (CT), the ability for DNA to carry charge through its π -stack[6]. Due to the reliance of this phenomena on the π -stacking of the nitrogenous bases, DNA CT is sensitive to DNA lesions and mismatches and can proceed over long molecular distances if the the DNA is well stacked[7]. In bacteria we have established a model for DNA-mediated redox signaling in which DNA CT occurs between 4Fe4S DNA-repair proteins, scanning the genome, and localizing repair proteins to a DNA lesion (Figure 5.1)[8].

Specific features of this model were experimentally validated: the 2+ and 3+ oxidation state of BER protein Endonuclease III (EndoIII) showed different binding affinities to DNA with a 500-fold lower K_d when EndoIII is in the 3+ oxidation state versus 2+[9]. The redox properties of the 4Fe4S cluster of EndoIII on and off DNA reveals that the 2+/3+ redox-couple is more easily accessed on DNA, suggesting redox of the 4Fe4S cluster occurs when EndoIII is bound to DNA[10]. Many *E.coli* 4Fe4S DNA-processing enzymes have been shown to have a 2+/3+ redox couple on DNA of 80mv vs. NHE, suggesting the ability of these proteins to signal with each other[3]. Different cluster-containing repair proteins of different function and domains of life have been shown using atomic force microscopy (AFM) to localize to DNA mismatches using the DNA-binding affinity redox switch[8, 9, 11]. Additionally, the evolutionary conservation a metabolically expensive 4Fe-4S cofactor in these repair proteins suggests additional function beyond being a structural motif. Following this model, previous work has demonstrated that redox signaling between 4Fe4S-cluster proteins DinG helicase and Endonuclease III (EndoIII) facilitates efficient resolution of R-loops[11].

Given multiple DNA-repair proteins have been shown to contain a 4Fe4S-cluster, inter-protein DNA-mediated redox signaling should exist between other repair pathways with a functional benefit of increased lesion detection efficiency. This signaling is essential as *E.coli* are a fast-dividing organism in which genome

fidelity must be maintained through each division within the time-limit of cellular division[12]. Insults to the genome result in diverse DNA lesions that require separate and specialized DNA-repair pathways to address in order to prevent these deleterious mutations[13]. Two examples of these specialized repair pathways are base excision repair (BER) and nucleotide excision repair (NER). BER proteins target single-base lesions resulting from oxidative damage to the DNA bases. NER proteins target bulky DNA lesions and multi-base lesions such as those formed after UV-irradiation. These separate repair pathways allow for a division of labor in identification, excision, and re-synthesis of each type of DNA lesion[14]. DNA-mediated redox signaling between 4Fe4S DNA-processing enzymes in separate repair pathways increases the efficiency of these proteins to locate DNA lesions.

EndoIII is a DNA glycosylase that has both glycosylase and AP lyase activity. It can process cytosine base lesions as a glycosylase and can cleave the phosphodiester backbone of DNA near an abasic site[15]. The 4Fe4S cluster of EndoIII has been implicated to signal to other repair pathways through its 4Fe4S[8, 11]. In order for CT signaling to occur between EndoIII and NER, a protein in NER must contain a 4Fe4S cluster. UvrC Endonuclease, involved in the dual-incisions of NER may contain this metal cofactor due to its unique conservation and arrangement of cysteine in the primary structure[16]. Additionally, electrochemical and spectroscopic characterization of purified MBP-UvrC confirms the presence of a DNA-CT active 4Fe4S cluster. Indeed, demonstration of signaling crosstalk between NER and BER further bolsters the nature of the 4Fe4S as a signaling cofactor in DNA-repair. Here, we have uncovered DNA-mediated redox-signaling from BER glycosylase Endonuclease III, to a NER endonuclease UvrC enhances the efficiency of UV lesion repair in *E.coli*.

5.2 Materials and Methods

Strains and plasmid construction

JW1625-1 and JW0063-1, a Δnth Keio collection knockout strain (gene product: EndoIII) and $\Delta araC$ knockout strain respectively, were acquired from the Coli Genetic Stock Center(CGSC, Yale)[17]. All rescue plasmids were derived from a PBBR1MCS-4 and contain a lac promoter for constitutive expression of protein. pWT and pY82A express WT and Y82A EndoIII respectively and were acquired from strains in previous work using a plasmid miniprep kit (Qiagen)[8]. pK120Q and pD138A express EndoIII K120Q and EndoIII D138A respectively and were generated using pWT as a template for site-directed mutagenesis using a Q5 mu-

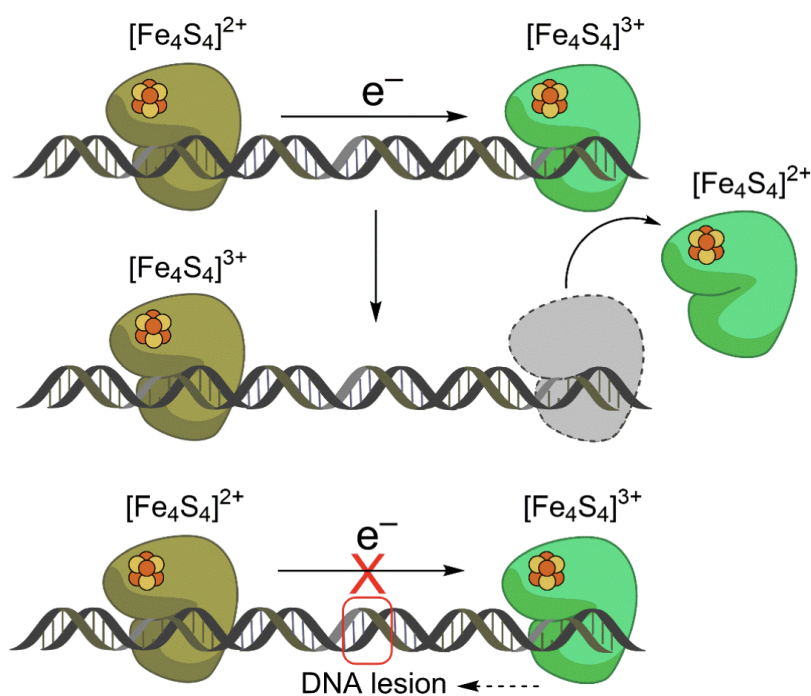


Figure 5.1: Schematic of DNA-mediated redox signaling. Two 4Fe4S containing DNA-repair proteins (green and olive) conduct redox between their clusters forcing one to bind with high affinity and the other to unbind with low affinity. This process can occur iteratively through DNA until a lesion is present where localization of bound repair proteins to the DNA-lesion follows.

tagensis kit (NEB). All plasmids expressing EndoIII have an additional 238 bp of upstream genome sequence to preserve endogenous mRNA context which is important to ensure low but equal amounts of cellular burden is placed on all strains[18]. pRFP expresses red fluorescent protein and was generated via Gibson assembly using a NEBuilder HiFi DNA assembly kit (NEB). Plasmid sequences and primers are listed in Table S1. Plasmids were maintained by transformation into NEB-5 α chemically-competent cells using heat-shock. Plasmids were transformed into Δ nth and Δ araC strains using electroporation (BioRad).

UV-sensitivity assay

Overnight starter cultures of Δ nth transformed with either pWT or pRFP were diluted 1:500 into 10mL of fresh LB media containing 100 μ g of ampicillin for 3 hours. An OD₆₀₀ measurement was taken and cell concentrations were adjusted to match optical density (OD) using phosphate buffered saline (PBS), diluted 20,000-

fold, placed into a transparent petri dish, and treated with 254nm UV at $30J/m^2$ UV inside a ultraviolet crosslinker (UVP). Each strain is subsequently plated as 10 μ L droplets and tilted to increase colony growth surface-area and facilitate colony-counting. Plates were imaged on a ChemiDoc gel imaging system (BioRad) and colonies were quantified from images using OpenCFU[19]. Survival was quantified as a fraction resulting from the number of colonies observed divided by the number of cells plated inferred via OD measurements at 600nm. The data reported is from three biological replicates.

Plate-reader UV-sensitivity assay

Overnight starter cultures of Δ araC(pRFP) and Δ nth transformed with pWT, pK120Q, pD138A, or pRFP cultured similarly to the above protocol. After OD₆₀₀ adjustment of all strains to the same OD, a 16-fold dilution into PBS was performed on each strain into a transparent petri-dish for 254nm UV-irradiation at $90J/m^2$. After treatment, the cell solution was diluted 16-fold into 7mL LB with 100 μ g ampicillin. 200 μ L of each genotype was placed into a unique column in a 96-well microplate and placed into a plate-reader (BioTek) for OD₆₀₀ readings every 10 minutes over 670 minutes in total. Three biological replicates were performed for every genotype and treatment condition.

Quantification of bacterial growth

Plate reader data was saved to a .csv and data analysis was performed using scripts written in *python 3.6.5* using *matplotlib*, *seaborn*, and *bokeh* for data visualization and *scipy*, *pandas*, and *numpy* for data cleaning and fitting[20–22]. Growth of strains from each well was fitted to a sigmoidal modified-gompertz equation[23]:

$$A = C \exp \left\{ - \exp \left[\frac{\mu_m}{C} (\lambda - t) + 1 \right] \right\} + A_0 \quad (5.1)$$

A is the OD₆₀₀ at time t , C is the carrying-capacity or asymptote of the growth curve, μ_m is the maximum specific growth rate, λ is the lag time, and A_0 is the initial OD₆₀₀ of a given well. Bacterial growth in each well was fitted to this equation using a nonlinear least squares method and histograms were generated after binning by genotype. a Δ lag-time parameter was calculated by subtracting the lag-time of each individual well by the lag-time of the minimum of the individual experimental dataset thus emphasizing differences in lag-times between strains in each independent experiment. 95% confidence interval was calculated via bootstrapping for all

parameters.

Protein Purification and quantification

WT EndoIII and point mutants Y82A and K120Q were overexpressed and purified out of BL21star-(DE3)pLysS cells. These proteins contained a His₆ ubiquitin tag and was purified as described previously and placed into a final storage buffer (20mM Tris, pH 8, 500mM NaCl, 5% glycerol) and buffer exchanged into an electrochemistry buffer (20mM sodium phosphate, pH 7.5, 150mM NaCl, 1mM ethylenediamine tetraacetate (EDTA)) for electrochemical, spectroscopic and gel-shift assays[24]. Protein stocks were stored at a concentration of $\sim 100\mu\text{M}$ and was quantified by the absorbance of the 4Fe4S cluster at 410nm using an extinction coefficient $\epsilon_{410\text{nm}} = 17000\text{M}^{-1}\text{cm}^{-1}$ on a UV-Vis spectrophotometer (Cary, Agilent).

DNA-Modified Electrochemistry

Preparation of thiol-modified dsDNA, fabrication and assembly of Au electrodes were performed as described previously[7, 25]. The DNA sequence used for EndoIII electrochemistry was used in previous experiments and is listed below[9]:

HS-C6-5'-GT GAG CTA ACG TGT CAG TAC-3'

3'-CA CTC GAT TGC ACA GTC ATG-5'

Au electrodes were incubated with 100uL thiol-modified dsDNA for 18 hours and then backfilled with 100 μL mercaptohexanol (1mM). This was followed by 5 100 μL repeated washes of the Au electrode surface with a glycerol buffer (20mM sodium phosphate, pH 7.5, 150mM NaCl, 1mM EDTA, 20% glycerol) and then by 5 100 μL repeated washes with electrochemistry buffer. 10 μM of WT, K120Q, or Y82A EndoIII was added to the surface for cyclic and square-wave voltammetry. The relationship of peak current to scan-rate of EndoIII was analyzed using a linear least squares method to produce regression lines for a linear or square-root of scan-rate dependence. The correct dependence is selected as the regression line with the highest coefficient of determination (R^2).

Electrophoretic Mobility Shift Assay

The nonspecific DNA-binding affinity was measured for K120Q and Y82A through a electrophoretic mobility shift assay (EMSA). dsDNA was purchased from Integrated DNA Technologies and purified by High Performance Liquid Chromatography (HPLC, Agilent). The DNA sequence used for EMSA was taken from previous

experiments and listed below[9]:

5'-ACT GAA CTC TGT ACC TGG CAC-3' [Strand A]

3'-TGA CTT GAG ACA TGG ACC GTG-5' [Strand B]

Strand A was radiolabeled with γ - ^{32}P -labeled ATP, 6000 Ci/mmol, 150 mCi/mL (Perkin-Elmer) using a T4 polynucleotide kinase (New England Biolabs) and purified using a Micro Bio-Spin 6 column (BioRad) followed by a Monarch PCR & DNA Cleanup Kit (NEB) to repeatedly wash the labeled DNA reaction with ethanol and kit DNA Cleanup binding buffer followed by a 25 μL elution with Monarch Elution Buffer. A 10 μM of annealed oligonucleotides was made by combining equimolar amounts of labeled strand A with strand B in the electrochemistry buffer and heating to 90°C for 10 minutes and cooled to room temperature over 3 hours. Annealing was verified by running a 10% polyacrylamide gel versus a single-stranded control lane at 4°C and imaged on a Typhoon FLA 9000 Imager (GE). 10 μM Labeled dsDNA was incubated with varying concentrations (0, 2.5, 5, 7.5, 15, 30, and 40 μM) of K120Q or Y82A EndoIII mutants (for 30 minutes at 4°C before gel electrophoresis with a 10 % polyacrylamide gel at 4°C. Exposure time on phosphor screens was calculated from the radioactivity of a 10 μL aliquot using a scintillation reading for a cumulative 2 million counts after exposure. Gels were imaged and analyzed in ImageQuant 5.2 by measuring free dsDNA band intensities to calculate fraction of DNA bound to EndoIII normalized by the highest free dsDNA band intensity when no EndoIII was added. DNA-binding affinities were fitted through a non-linear least squares method to a Hill equation with a $n = 1$ Hill coefficient.

UV-Vis Spectroscopy to monitor cluster degradation

Protein stocks of K120Q, Y82A, and WT EndoIII were diluted to ~10 μM in electrochemistry buffer and UV-vis spectra were recorded over a 28 hour timecourse. The loss of the 4Fe4S cluster absorbance was monitored over time and normalized by the maximum 4Fe4S absorbance for each point mutant to extract the fraction of 4Fe4S cluster remaining. A linear least-squares regression was calculated to extract a rate of degradation for each EndoIII point mutant.

Circular Dichroism

Protein stocks of K120Q, Y82A, and WT EndoIII were diluted to ~10 μM in electrochemistry buffer and circular dichroism (CD) spectroscopy was performed

(Aviv Model 430) in the electrochemistry buffer (see above). The CD signal was normalized by dividing each data point by the minimum of the dataset. A ratio of 222nm to 208nm was calculated for comparison of coiled-coil formations between point mutants.

5.3 Results

E. Coli is sensitized to UV after EndoIII knockout

Previous work demonstrating EndoIII signaling to DinG in R-loop repair suggested the potentially diverse redox signaling capabilities of EndoIII in other DNA-repair pathways[11]. From cysteine conservation and positioning, *E.coli* UvrC was considered to contain a 4Fe4S cluster and thus could be the conduit through which EndoIII can signal to the nucleotide excision repair pathway. Thus, the lack of signaling between EndoIII and NER should manifest as an increased sensitivity of *E.coli* to UV in the absence of EndoIII. Indeed, we observe this sensitivity as a decrease in colony forming units (CFU) in a droplet-based assay when treating a Δ nth *E. coli* strain with UV (Figure 5.2). This sensitivity is assuaged by complementation of the Δ nth strain with a plasmid expressing WT EndoIII.

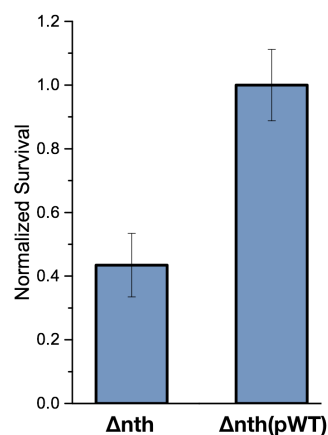


Figure 5.2: UV-sensitivity droplet assay. Strains of Δ nth expressing either WT-*nth* or RFP were treated with $30J/m^2$ UV and plated as droplets. Colonies were quantified and the fraction survival was calculated and normalized to WT conditions. Data presented are of three biological replicates.

In order to quantify the impact of UV to the growth of these strains, we tracked strain growth over 11 hours through OD measurements (Figure 5.3). Comparing the growth curves of Δ nth and Δ araC, the most evident change is in the lag-time or the time it takes for a strain to reach log phase. Here, cells expressing EndoIII reach log phase 1 hour sooner than cells with EndoIII knocked out, suggesting that UV

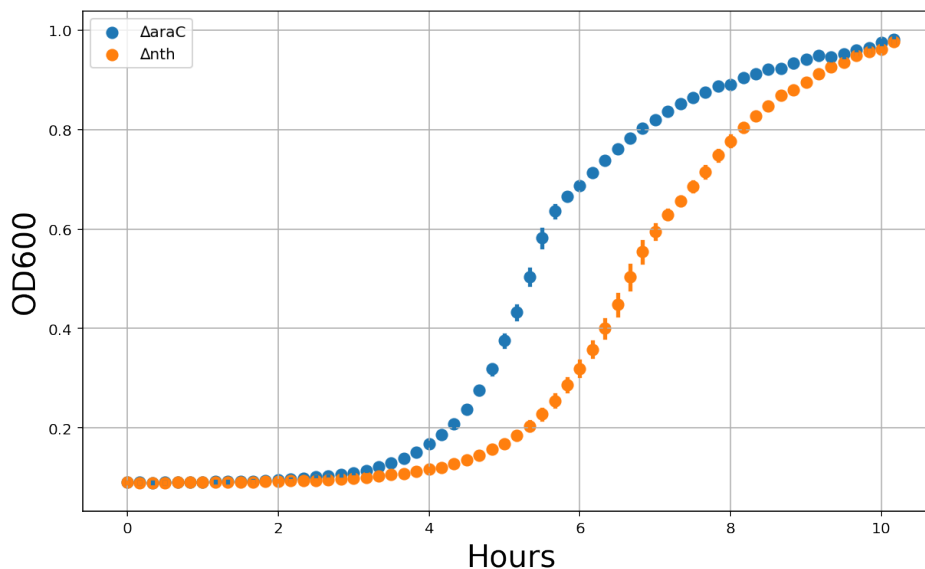


Figure 5.3: Average growth curve of Δ nth and Δ araC over 11 hours measured through OD600 readings. Error bars are the 95% confidence interval calculated using the bootstrap method.

lesions introduced after treatment are fully resolved as all strains reach log phase and have similar carrying capacities. Overall growth curves for all strains were comparable in growth rate and carrying capacity (Figure A.15). However, growth lag-times does change in the presence or absence of EndoIII, suggesting that EndoIII positively affects the efficiency of UV lesion repair.

Efficient UV-induced DNA lesion repair requires DNA CT active EndoIII

To investigate the mechanism through which EndoIII increases the repair of UV lesions, growth curves were monitored for a variety of strains expressing different point mutations of EndoIII to connect EndoIII protein biochemistry with observed growth phenotypes. Growth curves for each genotype were recorded and fitted individually. An averaged representation of the growth curves for each genotype is shown in Figure A.15. For each mutant, the initial ODs were similar, demonstrating that the amount of *E.coli* plated was consistent in all strains (Figure A.12). The mean Δ lag-times of Δ nth and Δ araC were quantified to be 0.15 and 0.97 hours respectively, indicating a near 1 hour lag between the two strains to reach log phase (Figure 5.4). This growth defect is lessened when WT EndoIII is introduced into the system and the Δ lag-time decreases to 0.26 hours. In the absence of UV, trends of lag-times between each strain mirror the UV-treated trends but are much

less pronounced, suggesting that the lag-time differences are mostly caused by the presence of UV-lesions(Figure A.13). The full extent of the Δ lag-time data was visualized via a beeswarm plot (Figure A.16).

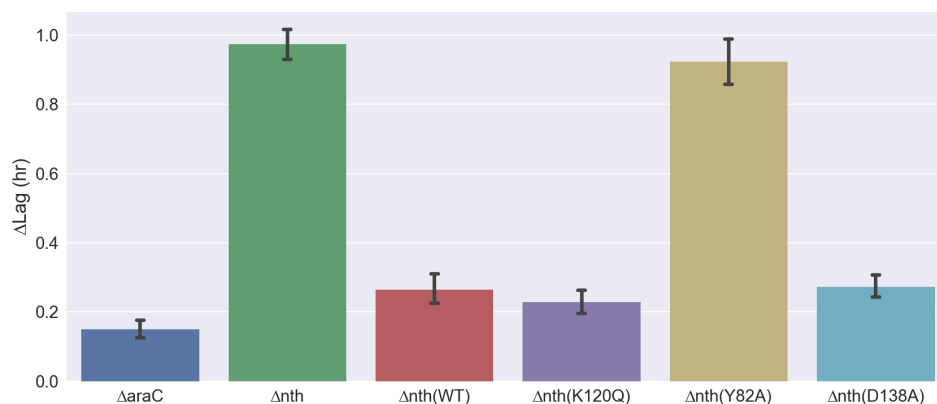


Figure 5.4: Δ lag-times of Δ araC and Δ nth strains with various rescue plasmids after treatment with $90J/m^2$ UV. Δ lag-times were calculated by subtracting the lag-time of each individual well by the lag-time of the minimum of the individual experimental dataset. Error bars are 95% confidence intervals calculated using the bootstrap methods. Data presented is from three biological replicates.

To check the effect of the enzymatic activity of EndoIII on lag-times, a K120Q EndoIII point mutant was used to rescue the growth defect. K120Q has been previously reported to have a 10^5 decrease in k_{cat} for apurinic sites, but after UV treatment, K120Q rescues have a similar Δ lag-time to WT at 0.23[15]. A similar trend is observed with D138A, another catalytically deficient mutant of EndoIII which has a Δ lag-time of 0.27. These observations demonstrate that the enzyme activity of EndoIII is not important in the repair of UV lesions. However, the Y82A point-mutant is poorly rescuing and has a Δ lag-time of 0.92. Y82A has been previously characterized to have catalytic function but poor DNA CT efficiency reflected from multiple DNA-modified electrochemistry and AFM experiments[8, 11, 26]. In this case, the poor growth rescue capabilities of Y82A mirrors its poor DNA CT efficiency and inability to facilitate DNA-repair proteins to redistribute to lesions.

Nonspecific DNA-binding affinity of K120Q and Y82A EndoIII

In order to delineate the contribution of DNA-binding affinities to the CT-signaling model, nonspecific DNA-binding affinities of K120Q and Y82A were measured using EMSA (Figure 5.5). The affinities of K120Q and Y82A to non-

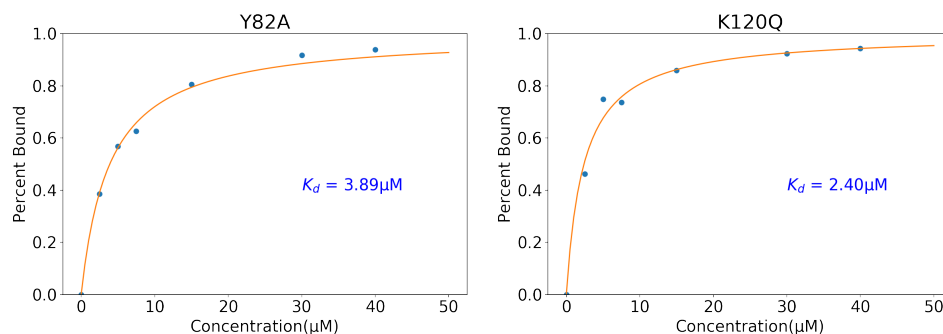


Figure 5.5: EMSA of K120 and Y82A for measurement of nonspecific DNA-binding affinity. K_d was calculated through non-linear least squares fitting of free dsDNA band intensities to a Hill equation with a Hill coefficient of 1.

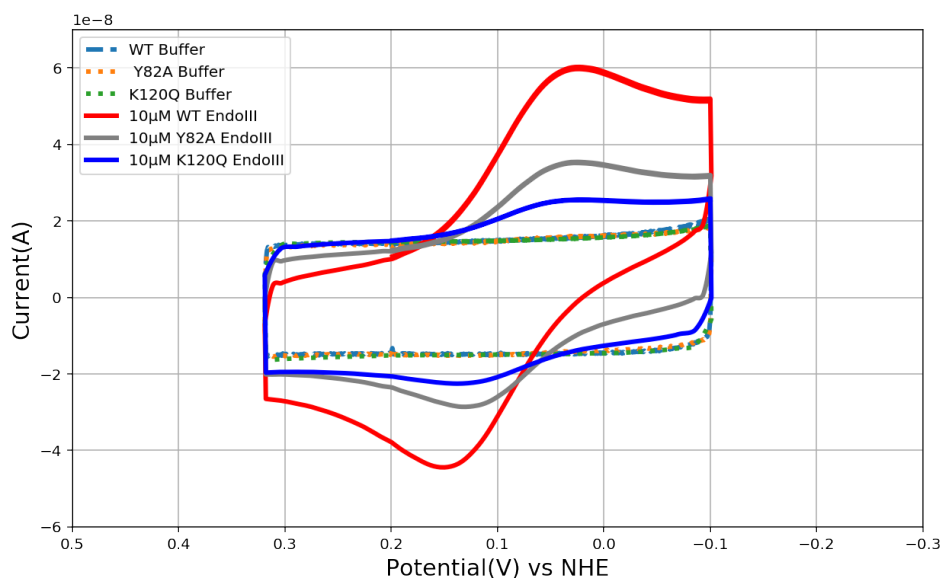


Figure 5.6: Cyclic voltammetry of WT, K120Q, and Y82A EndoIII. Buffer scan capacitance for each point-mutant indicate similar DNA-modified surfaces before the addition of protein. A reversible redox reaction is observed at 80mv vs. NHE.

specific DNA were $2.4\mu\text{M}$ and $3.9\mu\text{M}$ respectively. Comparing these affinities to the WT EndoIII nonspecific DNA-binding affinity of $6.6\mu\text{M}$ (measured previously using microscale thermophoresis (MST)) [9], we observe at most a 3-fold difference in affinity between WT and K120Q EndoIII, which dwarfs in comparison to the 500-fold change in binding affinity between the $[\text{Fe}_4\text{S}_4]^{2+}$ and $[\text{Fe}_4\text{S}_4]^{3+}$ state.

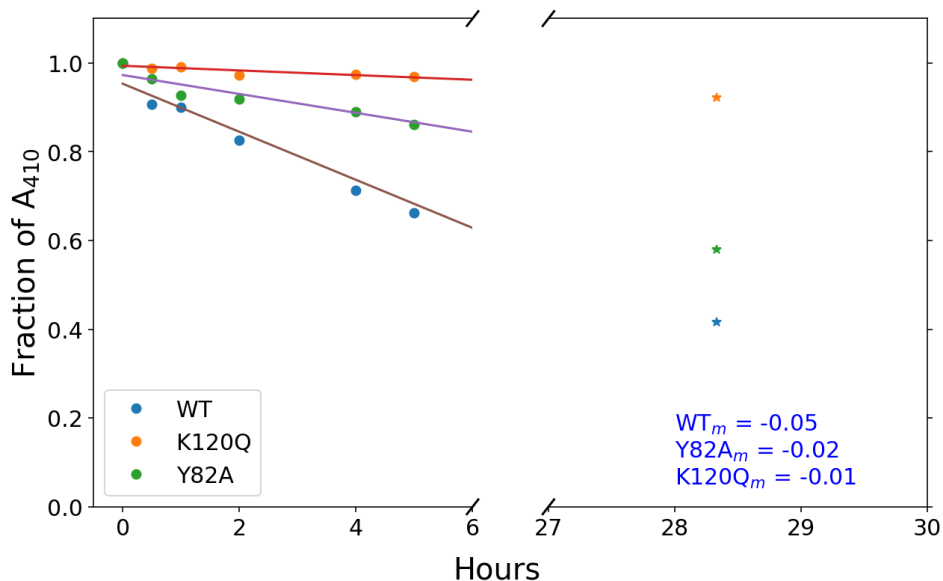


Figure 5.7: Quantification of Cluster degradation using UV-Vis. The absorbance intensity at 410nm was measured as a proxy for the concentration of the 4Fe4S cluster over 28 hours. Linear regression was performed using the least squares method for all data points up to 6 hours to model degradation over the timescale of a typical electrochemical experiment.

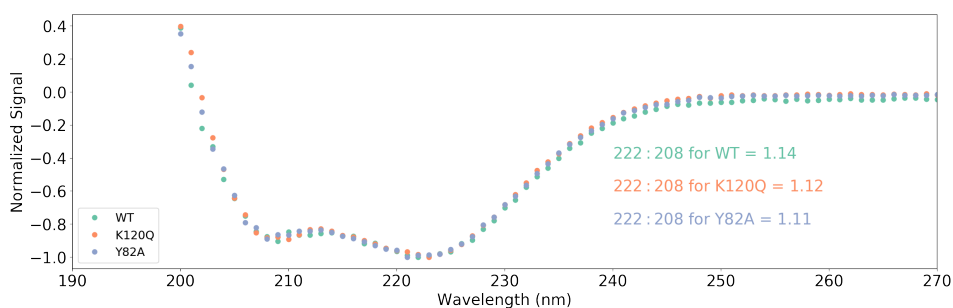


Figure 5.8: Circular Dichroism spectroscopy on WT, K120Q, and Y82A EndoIII. CD signals were normalized to the minimum signal of each dataset by division. A ratio of 222:208nm was calculated for each point mutant to report the presence coiled-coils.

Electrochemical and spectroscopic characterization of K120Q and Y82A EndoIII

We characterized the electrochemical properties of K120Q and Y82A EndoIII compared to WT using cyclic voltammetry. Cyclic voltammograms obtained after 2hr EndoIII incubation on a DNA-modified gold electrode revealed both Y82A and K120Q had smaller redox current peaks compared to WT (Figure 5.6). K120Q

EndoIII was measured to have the smallest current peak between the three. UV-Vis spectroscopy was performed to connect the observed current magnitudes of WT, K120Q, and Y82A EndoIII with cluster stability through the loss of absorbance at 410nm (Figure 5.7). Indeed, K120Q EndoIII displayed the slowest degradation of absorbance signal at 410nm whereas WT was the fastest to degrade. Besides differences in the rate of cluster degradation, no structural differences were observed using CD spectroscopy as K120Q, Y82A, and WT EndoIII displayed characteristic alpha helical CD spectra and similar 222:208nm ratios.

5.4 Discussion

EndoIII has now been shown to increase DNA lesion processing efficiency for both R-loop maturation and NER [11]. Growth phenotype differences are present between the InvA growth assay and the growth assay in this work due to the nature how of the DNA lesion is produced. In InvA growth, the R-loop lesion is genetically programmed through inversion of the *rrnA*, requiring repair to occur in every cell during every doubling [27]. Thus, the resulting growth is affected by the lesion both in growth rate and lag-times. Here, UV-lesions are initially introduced in a bolus of UV irradiation which requires time to repair. However, once the inhibitory UV-lesions are resolved, the cell can continue to grow. Thus, we observe the greatest impact on growth for our UV-treated strains to be in the lag-time. This increase in growth lag-time is rescued with the presence of WT, D130A, or K120Q EndoIII but not with Y82A EndoIII (Figure 5.4). The two catalytically deactivating mutations, K120Q and D138A, rescue the growth defect fully. This establishes that enzyme activity is not required for signaling between EndoIII and UvrC but electron transfer efficiency of residue Y82 in EndoIII may be essential for CT signaling.

DNA-binding affinities should play a role in the efficiency of the DNA-mediated redox signaling model for detecting DNA lesions [9]. If a protein does not bind well to nonspecific DNA, it is less participatory to scanning the DNA for lesions through the DNA CT model. Measurements of nonspecific DNA-binding affinities of K120Q and Y82A point mutants show that both proteins have similar binding affinities and are slightly tighter though in the same order of magnitude as the WT affinity (Figure 5.5). Thus, the observed growth defect rescue using K120Q and lack of rescue with Y82A are not due to differences in their capacity to bind to DNA non-specifically.

Electrochemical differences between these proteins may contribute to their

differences in rescue capacity. Cyclic voltammograms comparing WT and Y82A EndoIII shows a decrease in the redox peak current of Y82A relative to WT, reflecting the inability of Y82A to rescue the growth-defect observed (Figure 5.6). However, K120Q shows a peak current signal lower than that of Y82A. The current signal of all mutants exhibited a linear dependence on the scan rate, suggesting protein adsorption to the DNA-modified electrode surface (Figure A.17). CD spectroscopy indicates no global structural differences between WT, K120Q, and Y82A EndoIII as the curve shape and the 222:208nm ratios are the same for all mutants (Figure 5.8). The peak current differences between the point-mutants is explained by *in vitro* differences of the stability of the 4Fe4S cluster. Monitoring the cluster absorbance at 410nm over time, it is clear that the mutant with the largest electrochemical current signal is the least stable in solution over time (Figure 5.7). Such a trend was observed previously with electrostatic cluster point mutants of EndoIII where lower protein stability meant greater solvent access to the cluster forming a water pocket[28–30]. Structured water molecules have been demonstrated to increase the efficiency of biological electron transfer and the same trends are observed here as with the electrostatic cluster point-mutants of EndoIII[24]. AFM experiments on K120Q may uncover a superior mismatch discrimination vs Y82A to contrast with the electrochemical results seen here. Also, anaerobic conditions may be necessary to characterize electrochemical properties more to true to *in vivo* conditions and prevent the observed cluster degradation within the timescale of an electrochemical experiment.

We have uncovered that DNA-mediated redox signaling of EndoIII increases the repair efficiency of UV lesions and facilitates crosstalk between BER and NER. This signaling does not depend on the enzyme activity of the proteins involved but are more closely tied to their electrochemical features. More effort must be put towards the connection of these electrochemical features to *in vivo* observations. Investigation into other NER cluster-containing proteins, such the UvrC homolog Cho, may further elucidate this signaling network and its coordination for effective DNA lesion repair [31]. Additionally, understanding the downstream gene expression consequences given UV-irradiation may add additional insight into the depth of this signaling crosstalk between NER and EndoIII[32]. This work acts as a step towards understanding the effect of DNA-CT on multiple repair pathways and demonstrates the flexibility for the 4Fe4S cluster to act as a signaling motif for DNA-repair proteins to effectively scan the genome.

References

- (1) Rouault, T. A.; Tong, W.-H. *Nature Reviews Molecular Cell Biology* **2005**, *6*, 345–351.
- (2) Stehling, O.; Vashisht, A. A.; Mascarenhas, J.; Jonsson, Z. O.; Sharma, T.; Netz, D. J. A.; Pierik, A. J.; Wohlschlegel, J. A.; Lill, R. *Science* **2012**, *337*, 195–199.
- (3) Bartels, P. L.; O’Brien, E.; Barton, J. K. In *Iron-Sulfur Clusters in Chemistry and Biology*, 2ed; De Gruyter: 2017; Vol. 2, pp 405–424.
- (4) O’Brien, E.; Holt, M. E.; Thompson, M. K.; Salay, L. E.; Ehlinger, A. C.; Chazin, W. J.; Barton, J. K. *Science* **2017**, *355*, DOI: 10.1126/science.aag1789.
- (5) Bartels, P. L.; Stodola, J. L.; Burgers, P. M. J.; Barton, J. K. *J. Am. Chem. Soc.* **2017**, *139*, 18339–18348.
- (6) Slinker, J. D.; Muren, N. B.; Renfrew, S. E.; Barton, J. K. *Nat Chem* **2011**, *3*, 230–235.
- (7) Boal, A. K.; Yavin, E.; Lukianova, O. A.; O’Shea, V. L.; David, S. S.; Barton, J. K. *Biochemistry* **2005**, *44*, 8397–8407.
- (8) Boal, A. K.; Genereux, J. C.; Sontz, P. A.; Gralnick, J. A.; Newman, D. K.; Barton, J. K. *Proc. Natl. Acad. Sci. U.S.A.* **2009**, *106*, 15237–15242.
- (9) Tse, E. C. M.; Zwang, T. J.; Barton, J. K. *J. Am. Chem. Soc.* **2017**, *139*, 12784–12792.
- (10) Bartels, P. L.; Zhou, A.; Arnold, A. R.; Nuñez, N. N.; Crespilho, F. N.; David, S. S.; Barton, J. K. *Langmuir* **2017**, *33*, 2523–2530.
- (11) Grodick, M. A.; Segal, H. M.; Zwang, T. J.; Barton, J. K. *J. Am. Chem. Soc.* **2014**, *136*, 6470–6478.
- (12) Wielgoss, S.; Barrick, J. E.; Tenaillon, O.; Cruveiller, S.; Chane-Woon-Ming, B.; Médigue, C.; Lenski, R. E.; Schneider, D. *G3: Genes, Genomes, Genetics* **2011**, *1*, 183–186.
- (13) Kang, J.; Blaser, M. J. *Nature Reviews Microbiology* **2006**, *4*, 826–836.
- (14) Truglio, J. J.; Croteau, D. L.; Van Houten, B.; Kisker, C. *Chem. Rev.* **2006**, *106*, 233–252.
- (15) Thayer, M. M.; Ahern, H.; Xing, D.; Cunningham, R. P.; Tainer, J. A. *EMBO J* **1995**, *14*, 4108–4120.
- (16) Grodick, M. A.; Muren, N. B.; Barton, J. K. *Biochemistry* **2015**, *54*, 962–973.
- (17) Baba, T.; Ara, T.; Hasegawa, M.; Takai, Y.; Okumura, Y.; Baba, M.; Datsenko, K. A.; Tomita, M.; Wanner, B. L.; Mori, H. *Mol Syst Biol* **2006**, *2*, 2006.0008.

- (18) Ceroni, F.; Algar, R.; Stan, G.-B.; Ellis, T. *Nat. Methods* **2015**, *12*, 415–418.
- (19) Geissmann, Q. *PLOS ONE* **2013**, *8*, e54072.
- (20) McKinney, W. In *Proceedings of the 9th Python in Science Conference*, ed. by Walt, S. v. d.; Millman, J., 2010, pp 51–56.
- (21) Hunter, J. D. *Computing in Science Engineering* **2007**, *9*, 90–95.
- (22) Jones, E.; Oliphant, T.; Peterson, P. **2001**.
- (23) Zwietering, M. H.; Jongenburger, I.; Rombouts, F. M.; van 't Riet, K. *Appl Environ Microbiol* **1990**, *56*, 1875–1881.
- (24) Pheeny, C. G.; Arnold, A. R.; Grodick, M. A.; Barton, J. K. *J. Am. Chem. Soc.* **2013**, *135*, 11869–11878.
- (25) Slinker, J. D.; Muren, N. B.; Gorodetsky, A. A.; Barton, J. K. *J. Am. Chem. Soc.* **2010**, *132*, 2769–2774.
- (26) Romano, C. A.; Sontz, P. A.; Barton, J. K. *Biochemistry* **2011**, *50*, 6133–6145.
- (27) Boubakri, H.; de Septenville, A. L.; Viguera, E.; Michel, B. *EMBO J* **2010**, *29*, 145–157.
- (28) Tezcan, F. A.; Crane, B. R.; Winkler, J. R.; Gray, H. B. *Proc. Natl. Acad. Sci. U.S.A.* **2001**, *98*, 5002–5006.
- (29) Van Amsterdam, I. M. C.; Ubbink, M.; Einsle, O.; Messerschmidt, A.; Merli, A.; Cavazzini, D.; Rossi, G. L.; Canters, G. W. *Nat. Struct. Biol.* **2002**, *9*, 48–52.
- (30) Miyashita, O.; Okamura, M. Y.; Onuchic, J. N. *Proc. Natl. Acad. Sci. U.S.A.* **2005**, *102*, 3558–3563.
- (31) Moolenaar, G. F.; Rossum-Fikkert, S. v.; Kesteren, M. v.; Goosen, N. *PNAS* **2002**, *99*, 1467–1472.
- (32) Courcelle, J.; Khodursky, A.; Peter, B.; Brown, P. O.; Hanawalt, P. C. *Genetics* **2001**, *158*, 41–64.

Appendix A

ADDITIONAL FIGURES AND TABLES

A.1 Supplemental figures for Chapter 2

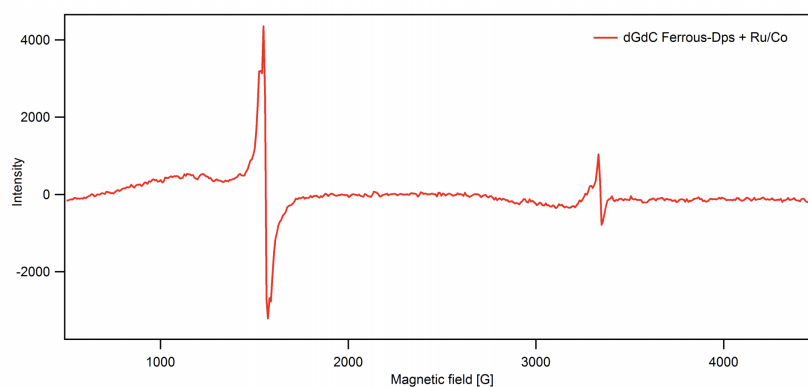


Figure A.1: Wide EPR spectra of irradiated sample containing WT ferrous iron-loaded Dps, poly(dGdC)₂ DNA, Ru(phen)(dppz)(bpy')²⁺, and [Co(NH₃)₅Cl]²⁺ with dark control subtracted. All conditions and instrument settings are identical to Figure 2.3 in Chapter 2.

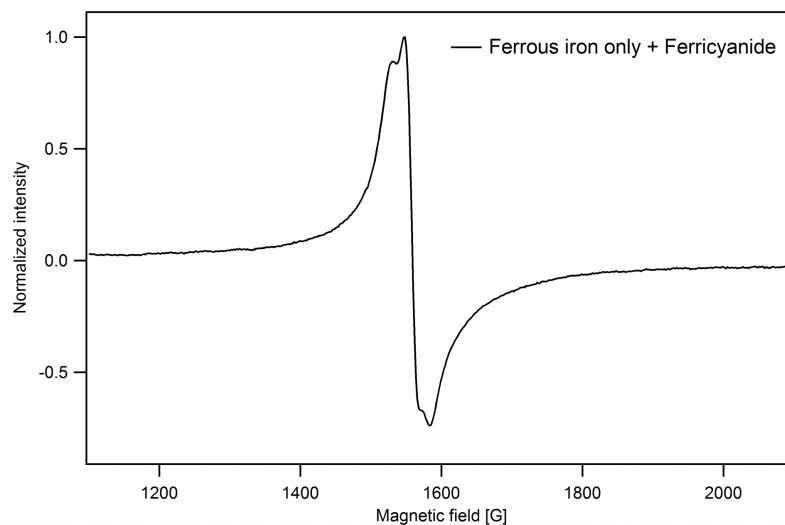


Figure A.2: Ferrous iron only (no protein) mixed with stoichiometric ferricyanide in 50 mM Tris, pH 7.0, 150 mM NaCl, 5% glycerol. Concentration of iron was 240 μ M, equivalent to that in 20 μ M solution of Dps with 12 Fe/Dps. Instrument settings identical are to Figure 2.3 in Chapter 2.

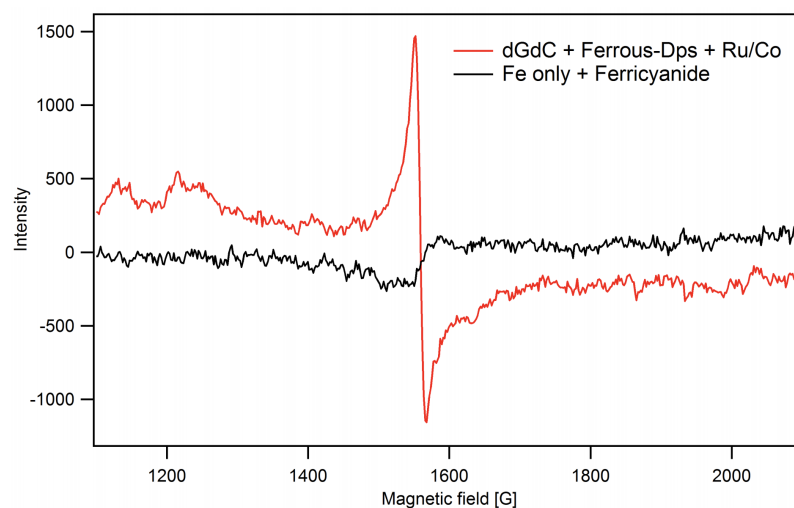


Figure A.3: WT Dps EPR spectra compared to Fe only control in MOPS buffer. Concentrations: Fe only: 240 μM ferrous iron with 240 μM ferricyanide (black trace). Irradiated Dps sample: 20 μM Dps ($\text{Fe}^{2+}/\text{Dps}$: 11.7 ± 0.1), 1 mM base-pairs poly(dGdC)₂ DNA, 20 μM $[\text{Ru}(\text{phen})(\text{dppz})(\text{bpy}')^{2+}]^{2+}$, 120 μM $[\text{Co}(\text{NH}_3)_5\text{Cl}]^{2+}$ (red trace). Buffer: 50 mM MOPS, pH 7.0, 150 mM NaCl, 5% glycerol. Dps spectrum has had DC subtracted. Instrument settings: modulation amplitude = 10 G at 100 kHz; frequency = 9.37 GHz; microwave power = 6.4 mW; temperature = 10 K.

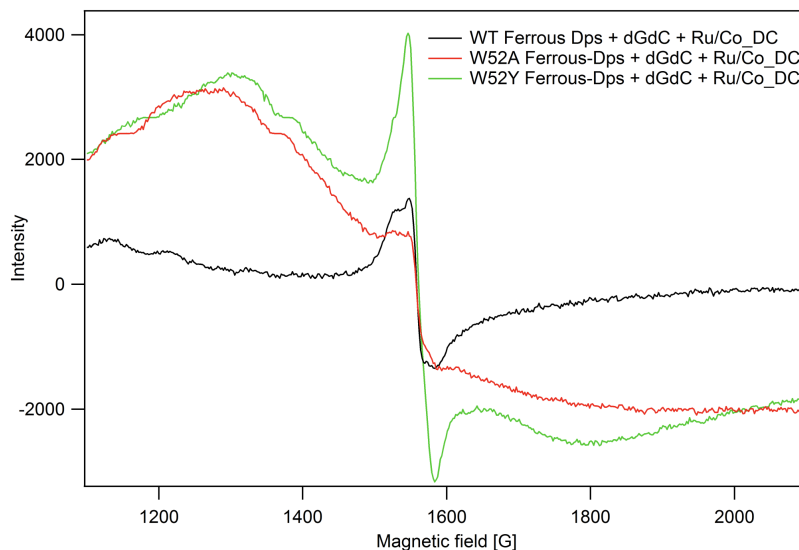


Figure A.4: Dark controls (before irradiation) of DNA-bound ferrous iron-loaded WT Dps and W52A/Y mutants. Spectra not adjusted for Fe loading of mutants. Concentrations: 20 μM Dps ($\text{Fe}^{2+}/\text{Dps}$: WT: 16.0 ± 0.5 , W52A: 10.1 ± 0.2 ; W52Y: 11.5 ± 0.2), 1 mM base-pairs poly(dGdC)₂ DNA, 20 μM $[\text{Ru}(\text{phen})(\text{dppz})(\text{bpy}')]^{2+}$, 120 μM $[\text{Co}(\text{NH}_3)_5\text{Cl}]^{2+}$. Buffer: 50 mM Tris, pH 7.0, 150 mM NaCl, 5% glycerol. Instrument settings: modulation amplitude = 5 G at 100 kHz; frequency = 9.37 GHz; microwave power = 6.4 mW; temperature = 10 K.

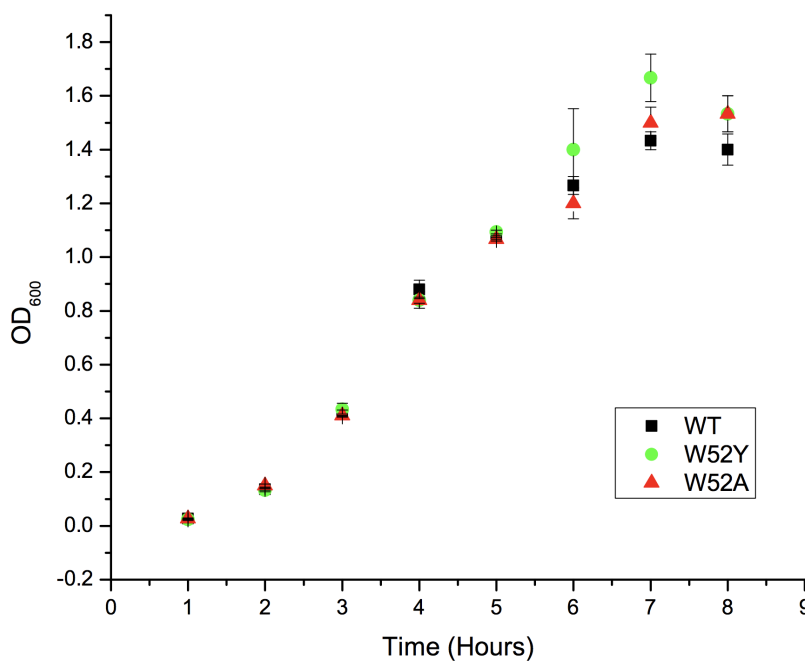


Figure A.5: Growth of *E. coli* ZK2471 strain (*dps::kan ΔrecA Δara*) containing WT, W52A, or W52Y pBAD18-*dps* plasmids induced with 0.2 w/v L-arabinose.

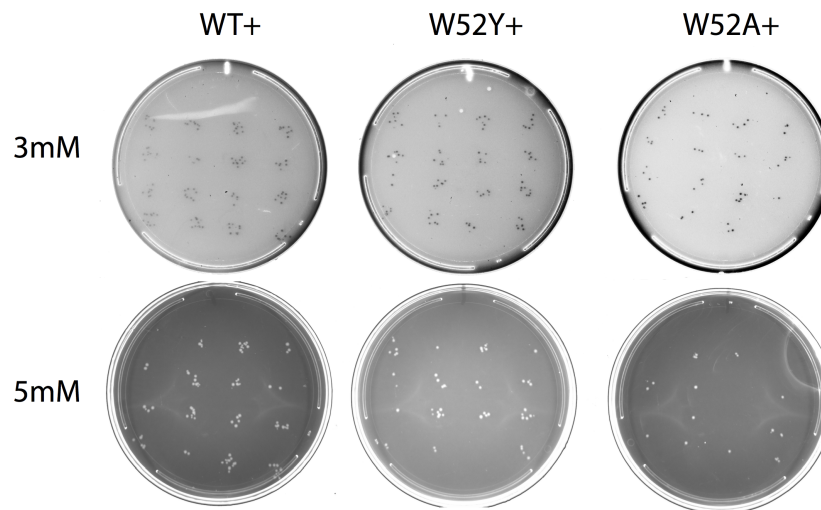


Figure A.6: Raw images of *E. coli* ZK2471 strain (*dps::kan ΔrecA Δara*) containing WT, W52A, or W52Y pBAD18-dps plasmids induced with 0.2 w/v L-arabinose, treated with 3mM and 5mM hydrogen peroxide, and diluted 10,000-fold.

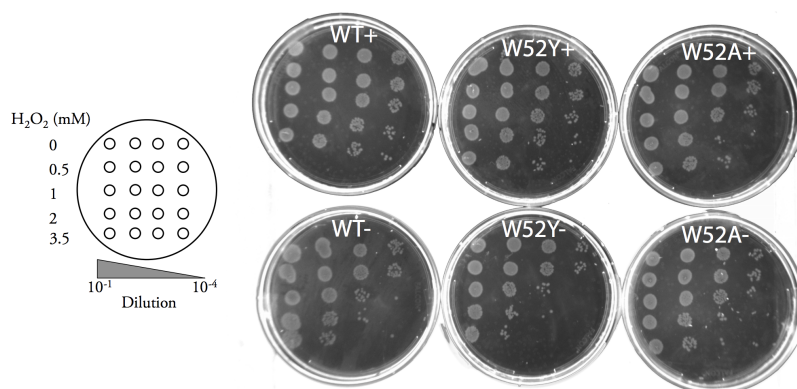


Figure A.7: *E. coli* ZK2471 strain (*dps::kan ΔrecA Δara*) containing WT, W52A, or W52Y pBAD18-dps plasmids induced (+) with 0.2 w/v L-arabinose or uninduced (-). Each 10 μ L droplet contains a unique dilution factor and concentration of hydrogen peroxide. This layout was conducted to extract optimal experimental conditions to ensure a quantifiable amount of colonies on plates. At 3.5 mM treatment of peroxide treatment (5th row colonies) there are clear differences in survival between induced and uninduced strains. We extrapolated that 3 mM H₂O₂ treatment of 10,000-fold diluted cells would create countable colonies for the survival assay.

A.2 Supplemental figures for Chapter 3

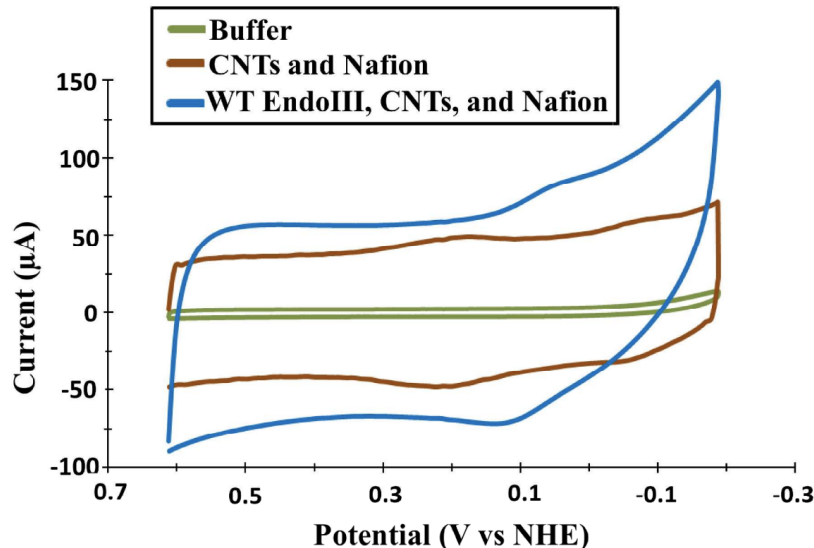


Figure A.8: CV scans of storage buffer, a CNT/Nafion thin film, and a WT EndoIII/CNT/Nafion thin film. CNTs increase the capacitance dramatically relative to buffer alone (20 mM sodium phosphate, pH 7.5, 150 mM NaCl, 0.5 mM EDTA; green plot), although they also enhanced the signal due to charged surface species (around 200 mV vs NHE) in addition to a signal near -80 mV vs NHE attributable to oxides on the CNTs themselves (brown plot). Notably, neither of these peaks exhibited any splitting, indicative of rapid processes taking place at the surface. Incorporation of 75 μM EndoIII into the thin film suppressed both of these signals, and resulted in the appearance of a reversible signal with noticeable peak splitting near 100 mV vs NHE. The much higher capacitance in these CVs relative to those in Figure 1 is due to the addition of 3-6 more layers of CNT/protein than later CVs, which made the comparison easier but also caused the EndoIII peaks to be less clearly defined. All CVs were taken at a scan rate of 100 mV/s.

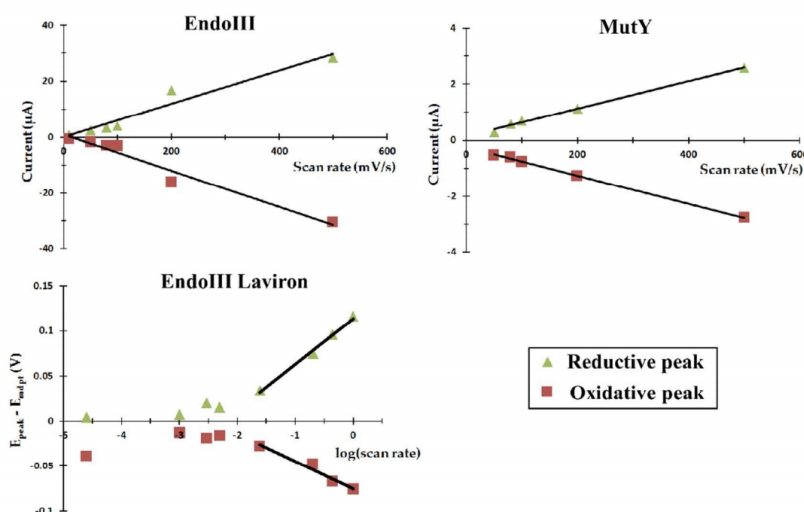


Figure A.9: Scan rate dependence of the current for EndoIII and MutY, and peak splitting for WT EndoIII. The linear dependence of current on scan rate confirms that the protein is adsorbed to the electrode surface (EndoIII, top right; MutY, top left). Because the proteins were adsorbed to the surface, Laviron's method for non-diffusive systems was applied to estimate electron transfer rates (k_{ET}) and coefficients (α) for EndoIII (bottom; the small size of the MutY signal precluded Laviron analysis).

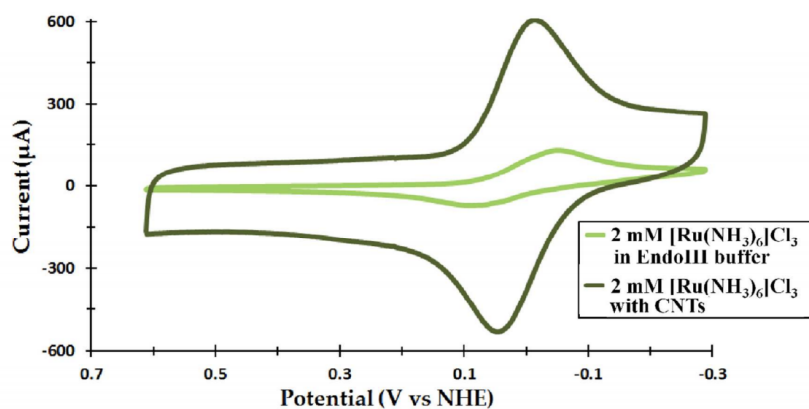


Figure A.10: Electrochemistry controls on the PGE electrode. To determine the electro-active area of the PGE electrode and to verify the accuracy of measured potentials, 2 mM $[\text{Ru}(\text{NH}_3)_6]^{3+}$ in EndoIII storage buffer was added in the presence (dark green) and absence of CNTs (light green). Notably, while the peak splitting decreased slightly in the presence of CNTs, the midpoint potential was unaltered.

A.3 Supplemental figures for Chapter 4

Technique	EndoIII	MutY
Ribosome Profiling (MOPS Complete)	542	501
Single Molecule Counting	6	7

Table A.1: Protein expression levels of EndoIII and MutY measured by ribosome profiling and single molecule counting [1, 2]

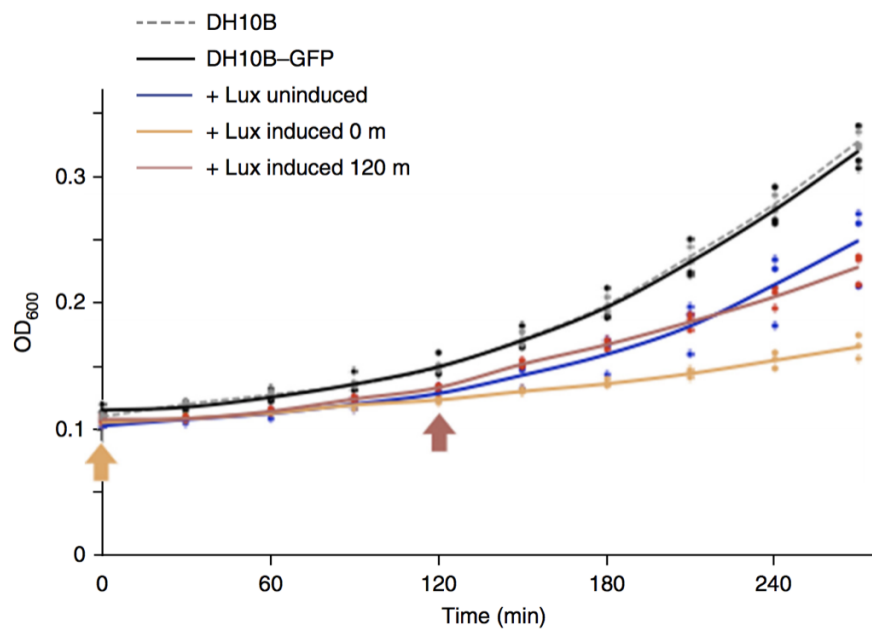


Figure A.11: Growth curves of E.coli after arabinose induction for expression of the Lux operon adapted from Ceroni et al [3].

A.4 Supplemental figures for Chapter 5

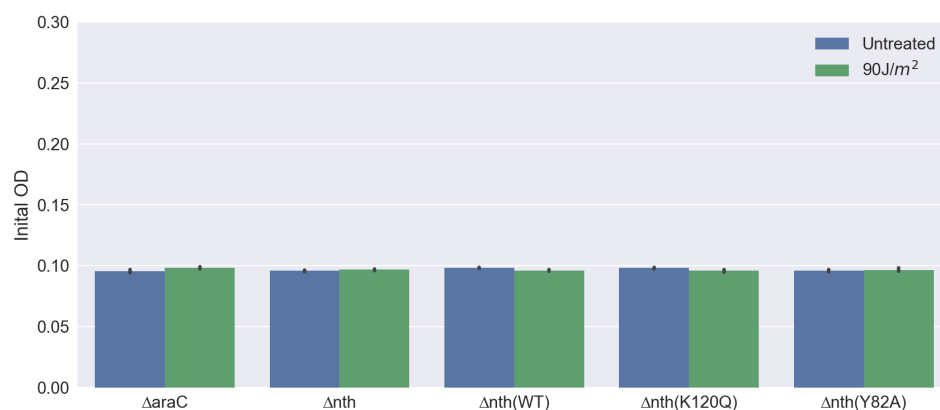


Figure A.12: The starting OD₆₀₀ of Δ araC and Δ nth strains with various rescue plasmids either treated with 90J/m² UV or left untreated. This initial-OD was extracted from the y-intercept of the curve fits for each well. Error bars are 95% confidence intervals calculated using the bootstrap methods. Data presented is from three biological replicates.

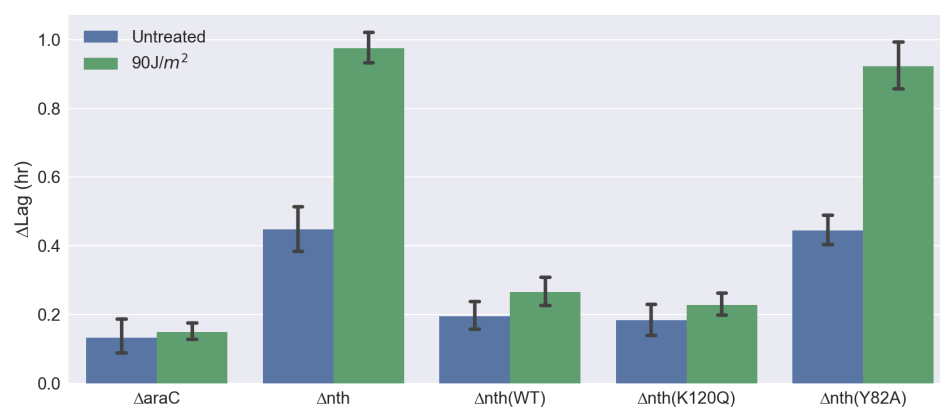


Figure A.13: The Δ lag-times of Δ araC and Δ nth strains with various rescue plasmids either treated with 90J/m² UV or left untreated. Error bars are 95% confidence intervals calculated using the bootstrap methods. Data presented is from three biological replicates.

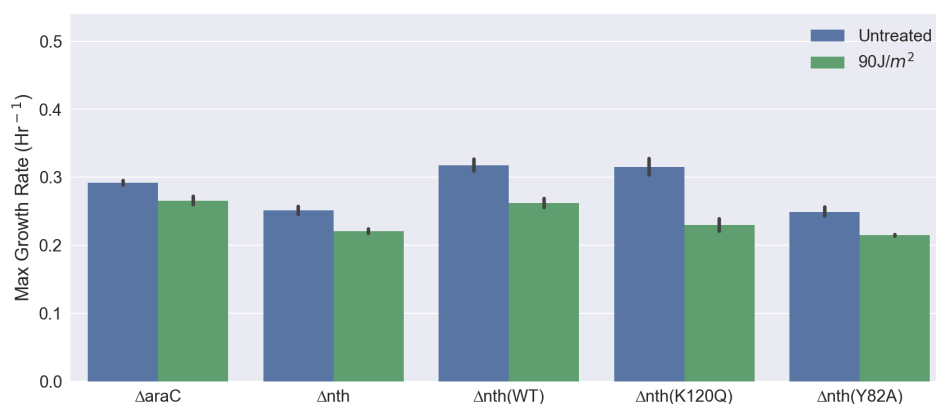


Figure A.14: The maximum specific growth of Δ araC and Δ anth strains with various rescue plasmids either treated with $90J/m^2$ UV or left untreated. Error bars are 95% confidence intervals calculated using the bootstrap methods. Data presented is from three biological replicates.

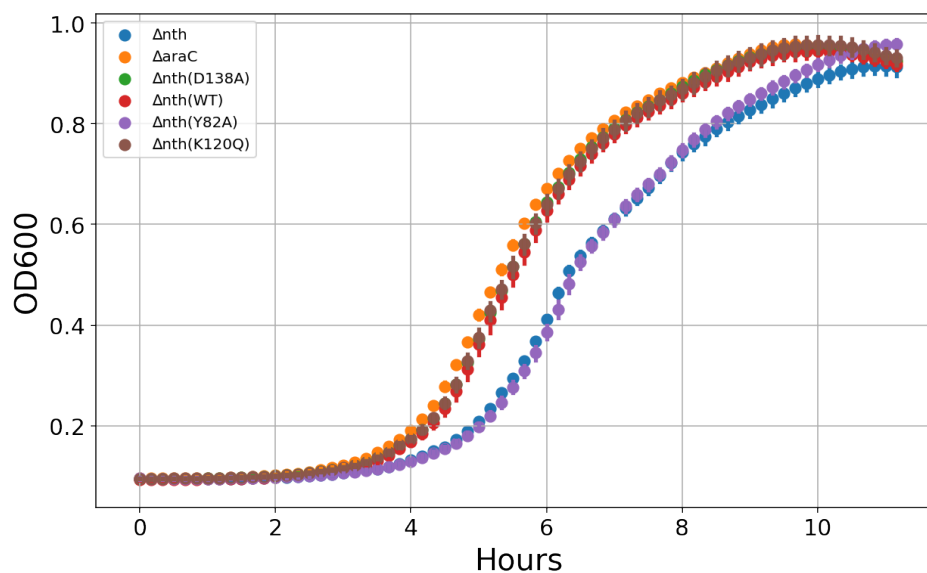


Figure A.15: 96-well plate OD600 growth curves of each genotype of E.coli after treatment of $90J/m^2$ UV. Curves from the 16 technical replicates of each genotype are represented as an average with a 95% confidence interval acquired through the bootstrap method.

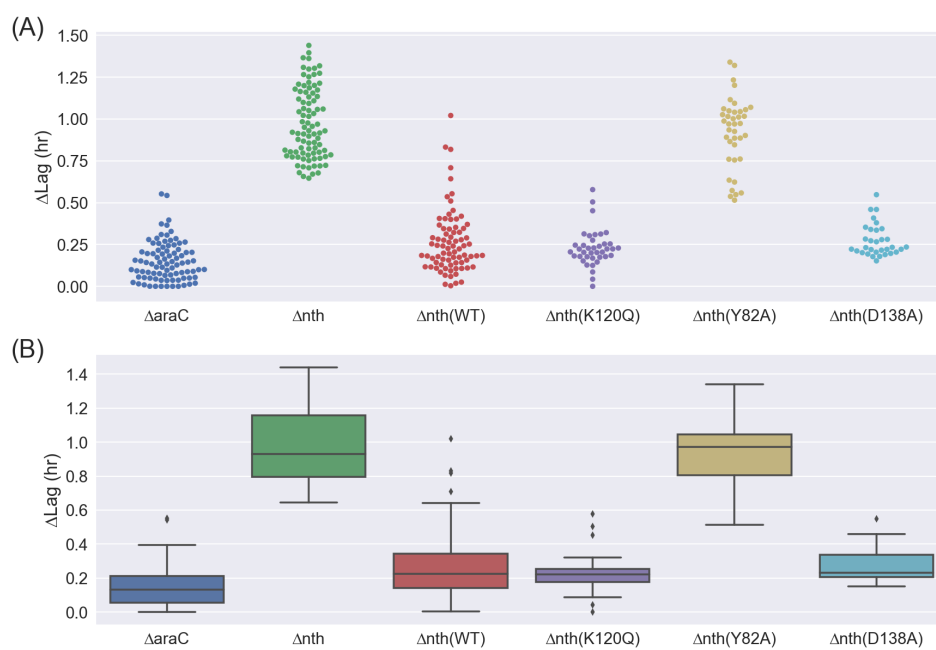


Figure A.16: (A) Δlag -time data of E.coli treated with $90J/m^2$ UV visualized as a beeswarm plot. Every observation over three biological replicates are plotted. (B) Boxplot of Δlag -time data showing the minimum and maximum extent of the data, outliers, median, and data quartiles (1st and 3rd).

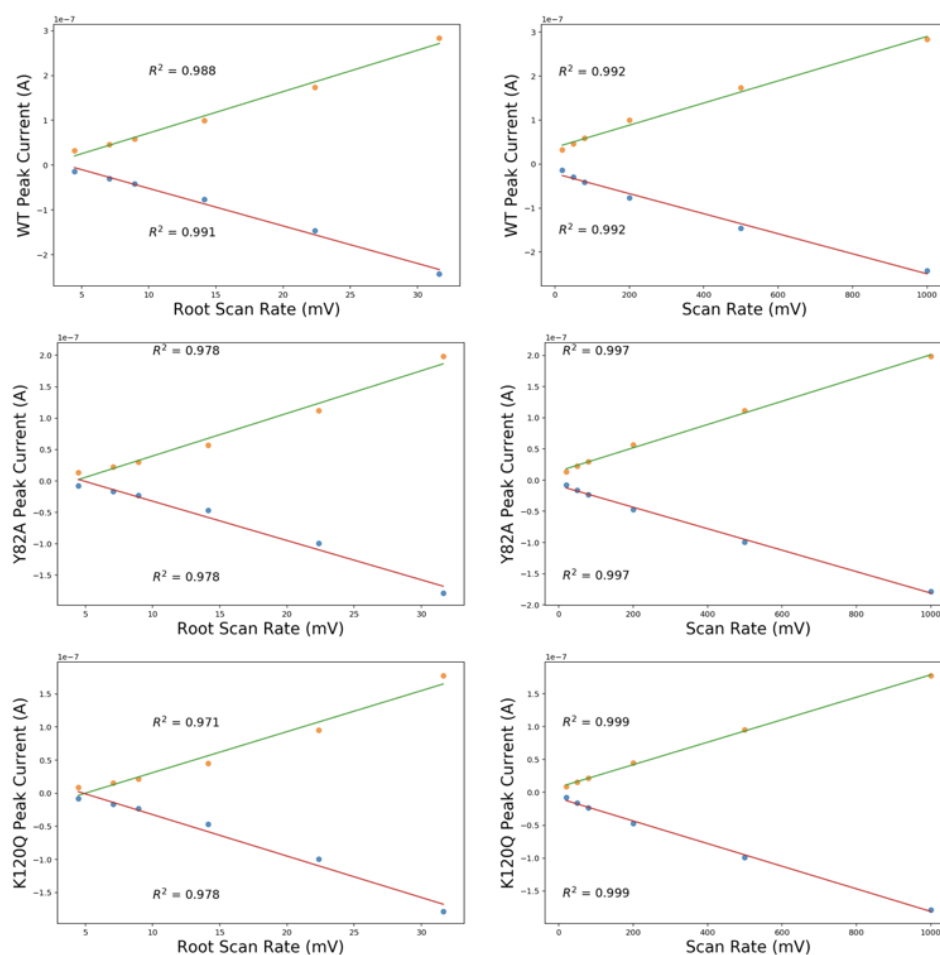


Figure A.17: Scan-rate dependence of WT, K120Q, and Y82A EndoIII. The relationship of peak current to scan-rate of EndoIII was analyzed using a linear least squares method to produce regression lines for a linear or square-root of scan-rate dependence. The correct dependence is selected as the regression line with the highest coefficient of determination (R^2).

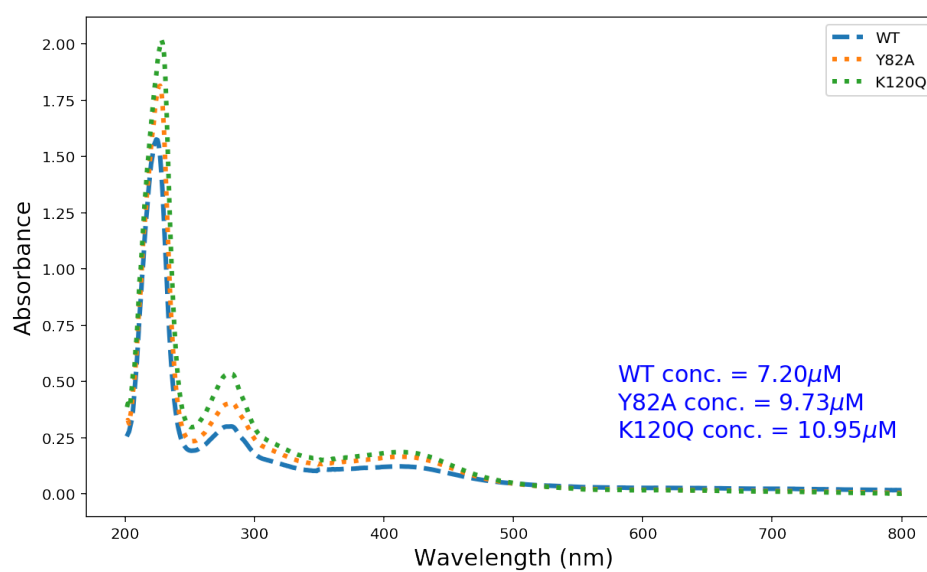


Figure A.18: UV-vis spectra of EndoIII point mutants at $t = 0$ hours. Starting concentrations are calculated by the absorbance of the 4Fe4S cluster at 410nm using an extinction coefficient $\epsilon_{410nm} = 17000M^{-1}cm^{-1}$. Cluster degradation analysis was completed by normalizing to these concentrations.

Appendix B

PRIMERS

Plasmid designation	Sequence 5'–3'
hk022_nth_backbone fwd + rev: Gibson assembly primers for hk022-nth vector	GCAATATGGACAATTGGTT-TCGATCCCCAATTCCTGGCAG AAGAGAAAGTTGACATCT-GAGCATGCCTCGAGATGCATGG
hk022_nth_insert fwd + rev: Gibson assembly primers for hk022-nth insert	CTGCCAGGAATTGGGGATCG-AAACCAATTGTCCATATTGCA CCATGCATCTCGAGGCATGCTCA-GATGTCAACTTTCTCTTTG
P1: Clonetegration check primer for colony PCR check primer	GGAATCAATGCCTGAGTG
P2: Clonetegration check primer for colony PCR check primer	ACTTAACGGCTGACATGG
P3: Clonetegration check primer for colony PCR check primer	ACGAGTATCGAGATGGCA
P4: Clonetegration check primer for colony PCR check primer	GGCATCAACAGCACATTC

Table B.1: Table of primers for Clonetegration [4].

Designation	Sequence 5'–3'
nth-genome-check fwd + rev: Colony PCR primers to amplify <i>nth</i> in the <i>E.coli</i> genome	GAGATCCGCATTCCCATTTA GGCTTAACGGCGATATGTTC
InvA-check fwd + rev: Colony PCR primers to confirm <i>rrnA</i> operon inversion in InvA	CCAGTCATTTGGCGAAAG GGCGTAATAGCGAAGAGG

Table B.2: Table of primers for colony PCR of InvA strain.

Plasmid designation	Sequence 5'-3'
pPro30_insert fwd + rev: Gibson assembly primers for pPro30-nth	GATTGGGCTTGCTAACAGCAAAGC GTTTTGATATAGGTTTTCACC
pPro30_backbone fwd + rev: inverse PCR to extract pPro30-nth backbone	TCTAGAGTCGACCTGCAG GCTAGCTTGTATCAACTTGTTAT
pLac-nth_backbone fwd + rev: Gibson assembly primers for pLac-nth backbone	AAGAGAAAGTTGACATCTG- AGGATCCAAACTCGAGTAAGG AGGCGTTTTGCTTTATTCATAT- GTATATCTCCTTCTTAAAAGATCTTT
pLac-nth_insert fwd + rev: Gibson assembly primers for pLac-nth insert	TTTTAAGAAGGAGATATA- CATATGAATAAAGCAAAACGCCT CCTTACTCGAGTTTGGATCCT- CAGATGTCAACTTTCTCTTTG
pLac-nth-RFP_backbone fwd + rev: Gibson assembly primers for pLac-nth-RFP backbone	AGAAAGTTGACATCGGCAGCG- CGAGTAGCGAAGACGTTAT AGGCGTTTTGCTTTATTCATA- TGTATATCTCCTTCTTAAAAGATCTTT
pLac-nth-RFP_insert fwd + rev: Gibson assembly primers for pLac-nth-RFP insert	TTTTAAGAAGGAGATATACAT- ATGAATAAAGCAAAACGCCT TCTTCGCTACTCGCGCTGCCGATG- TCAACTTCTCTTTGTATT
pLac-RFP-nth_backbone fwd + rev: Gibson assembly primers for pLac-RFP-nth backbone	ACAAAGAGAAAGTTGACATCGGAT- CCAAACTCGAGTAAGGATCTC CGTTTTGCTTTATTGCTG- CCAGCACCGGTGGAGTGACGAC
pLac-RFP-nth_insert fwd + rev: Gibson assembly primers for pLac-RFP-nth insert	ACTCCACCGGTGCTGGCAGCA- ATAAAGCAAAACGCCTGGA CCTTACTCGAGTTTGGATCCG- ATGTCAACTTCTCTTTGTATT
pBAD-nth_backbone fwd + rev: Gibson assembly primers for pBAD-nth backbone	AAGAGAAAGTTGACATCT- GAGGATCCAAACTCGAGTAAGG AGGCGTTTTGCTTTATTCATATGT- ATATCTCCTTCTTAAAAGATCTTT
pBAD-nth_insert fwd + rev: Gibson assembly primers for pBAD-nth insert	TTTTAAGAAGGAGATATACAT- ATGAATAAAGCAAAACGCCT CCTTACTCGAGTTTGGATCCT- CAGATGTCAACTTTCTCTTTG

Table B.3: Table of primers for pPro, pLac, and pBAD tunable EndoIII plasmids.

Plasmid designation	Sequence 5'–3'
Y82A_SDM fwd + rev: Site directed mutagenesis primers for Y82A EndoIII	GATTGGGCTTGCTAACAGCAAAGC GTTTTGATATAGGTTTTCACC
D138A_SDM fwd + rev: Site directed mutagenesis primers for D138A EndoIII	TATTGCTGTCGCCACGCACATTTTCC GTCGGCCAGCCGAATGCA
K120Q_SDM fwd + rev: Site directed mutagenesis primers for K120Q EndoIII	CGTAGGTCGTCAAACAGCCAACGTCG CCGGGCAGGGCTTCAAGC
pLac-RFP_backbone fwd + rev: Gibson assembly primers for pLac vector	GTCACTCCACCGGTGCTTAAA- GAAAAGGGGTAACACCGAT ACGTCTTCGCTACTCGCCA- TCAGACATTCCCTGTTTCACC
pLac_RFP_insert fwd + rev: Gibson assembly primers for RFP insert	GGTGAAACAGGGAATG- TCTGATGGCGAGTAGCGAAGACGT ATCGGTGTTACCCCTT- TTCTTTAAGCACCGGTGGAGTGAC

Table B.4: Table of primers for site directed mutagenesis of EndoIII and RFP control plasmid.

REFERENCES FOR FIGURES AND TABLES

- (1) Li, G.-W.; Burkhardt, D.; Gross, C.; Weissman, J. S. *Cell* **2014**, *157*, 624–635.
- (2) Taniguchi, Y.; Choi, P. J.; Li, G.-W.; Chen, H.; Babu, M.; Hearn, J.; Emili, A.; Xie, X. S. *Science* **2010**, *329*, 533–538.
- (3) Ceroni, F.; Algar, R.; Stan, G.-B.; Ellis, T. *Nat. Methods* **2015**, *12*, 415–418.
- (4) St-Pierre, F.; Cui, L.; Priest, D. G.; Endy, D.; Dodd, I. B.; Shearwin, K. E. *ACS Synth. Biol.* **2013**, *2*, 537–541.